5-2017

Control Oriented Nonlinear Model Reduction for Distributed Parameter Systems

Samir Sahyoun
University of Tennessee, Knoxville, ssahyoun@vols.utk.edu

To the Graduate Council:

I am submitting herewith a dissertation written by Samir Sahyoun entitled "Control Oriented Nonlinear Model Reduction for Distributed Parameter Systems." I have examined the final electronic copy of this dissertation for form and content and recommend that it be accepted in partial fulfillment of the requirements for the degree of Doctor of Philosophy, with a major in Electrical Engineering.

Seddik Djouadi, Major Professor

We have read this dissertation and recommend its acceptance:

Kevin Tomsovic, Suzanne Lenhart, Husheng Li

Accepted for the Council:

Dixie L. Thompson

Vice Provost and Dean of the Graduate School

(Original signatures are on file with official student records.)

Control Oriented Nonlinear Model Reduction for Distributed Parameter Systems

A Dissertation Presented for the

Doctor of Philosophy

Degree

The University of Tennessee, Knoxville

Samir Sahyoun

May 2017

I dedicate this work to those who make my life meaningful; my father and the soul of my mother, my wife, brothers sisters, and friends.

Acknowledgements

I would like to thank my advisor Dr Seddik Djouadi, I would have never made it without his continuous help, solid support and valuable guidance. Not only he is smart and his beautiful mind is always full of ideas as an academic advisor, he is also such a great person that I always considered as a brother.

I would like to thank my committee members Dr Kevin Tomsovic, Dr Suzanne Lenhart and Dr Husheng Li for their support and their valuable suggestions.

I would like to thank my friends in Knoxville; Wassim Bara, Mohammed Olama and Essam Elshreafi, and my colleagues; Jin Dong, Chao Ma, Anis Drira, Ehsan Raoufat, Chris Winstead and Yitchen Zhang.

Abstract

The development of model reduction techniques for physical systems modeled by partial differential equations (PDEs) has been a very active research area. Large number of states is needed to accurately capture the dynamics of such systems which makes them unsuitable for control design. The order of the system must be reduced prior to control design. In this dissertation, new methods that generalize the popular proper orthogonal decomposition (POD) to nonlinear PDEs are investigated. In particular, cluster based POD algorithms are developed and applied to the one and two dimensional Burgers equations that govern a nonlinear convective flow. Each cluster contains relatively close in distance dynamic behavior within itself, and considerably far with respect to other clusters. Three different clustering schemes in time, space and space-time are proposed. A complete and detailed approach for the Orthogonal Locality Preserving Projections (OLPP) modes computation for the incompressible Navier-Stokes PDE that governs the dynamics of the NACA 0015 airfoil fluid flow is presented. Close snapshots in the full order model are forced to stay close in the reduced order model by defining an optimization problem that preserves local distances. Optimal boundary control laws are derived based on the proposed nonlinear reduced order models, and applied to various distributed parameter systems including: Nonlinear convection, temperature control in energy efficient buildings systems governed by the heat equation, power and voltage control in large electromechanical oscillations in the power grid governed by the wave equation, and flow separation control for fluid flows governed by the Navier-Stokes equations.

Table of Contents

List of Tables

List of Figures

Chapter 1

Introduction

Model order reduction became an active research area in the last few decades as it is computationally difficult to design control laws for systems described by partial differential equations. Large number of states is needed to accurately capture the dynamics of such systems which makes them unsuitable for control design [50]. Conventionally the order of the system must be reduced before control law design can be done.

Many different model reduction approaches exist, but only few of them are optimal in some sense. The popular balanced truncation based on singular value decompositions is one of them. It is a main tool used in both "reduce-then-design" and "design-then-reduce" approaches. The theory of balanced model reduction was initiated by B.C. Moore for controllable, observable and exponentially stable linear systems in state space form [47].

In balanced truncation, the system is first transformed to a basis where the "difficult to reach" states are simultaneously "difficult to observe. This is done by simultaneously diagonalizing the reachability and the observability Gramians, which are solutions to the reachability and the observability Lyapunov equations. The reduced model is obtained by truncating these states. While this method preserves stability, it suffers two important limitations; it is not optimal in any sense and it efficiently applies to linear systems only. Some work has been done by [69] to extend balancing to nonlinear systems but the limitation there is that the method requires solving the complicated nonlinear Hamilton Jacobi equations.

Proper Orthogonal Decomposition (POD), introduced in the context of fluid dynamics by [42] and detailed by [26] is a model reduction technique that is efficient when used to reduce models that approximate nonlinear infinite dimensional systems to lower order finite dimensional systems, especially those who describe the dynamics of fluid flows. POD is a popular model reduction technique used to alleviate the computational expense required for very high dimensional systems [26]. The tools of POD have been used for some time as a model order reduction technique to achieve faster simulations of complex high dimensional systems. POD models of only a few dozen states have been shown to accurately capture the system dynamics of the full order system model of thousands of states [15]. Model reduction using POD is often conducted to extract a relevant set of basis vectors.

In POD the snapshot method is usually used to create an ensemble of solutions with particular open loop control input data. [71] suggested the method of snapshots as a way of determining the optimal basis vectors without explicitly calculating the kernel necessary for POD.

The problem with POD is that it fails to capture the nonlinear degrees of freedom in nonlinear systems, since it assumes that data belongs to a linear space and therefore relies on the Euclidean distance as the metric to minimize. However, snapshots generated by nonlinear partial differential equations (PDEs) belong to manifolds for which the geodesics do not correspond in general to the Euclidean distance. A geodesic is a curve that is locally the shortest path between points. The global nonlinear manifold geodesic is difficult to be quantified in general but we show in this dissertation that it can be approximated efficiently by local linear Euclidean distances.

In [1] the solution snapshots were partitioned into sub-regions that characterize the nonlinear features of the solutions of interest. This partitioning was performed by computing snapshots of the solution, clustering them according to their relative distances using the k-means algorithm, computing in each cluster a reduced-order basis using POD method, identifying each snapshot cluster with a sub-region of the solution space, and assigning to this sub-region the reduced-order basis computed in that cluster.

Nonlinear control theory covers a wider class of systems that do not obey the superposition principle. It applies to more real-world systems which are often governed

by nonlinear partial differential equations. The mathematical techniques which have been developed to handle them are more rigorous and much less general, often applied only to a narrow class of systems. Even if the plant is linear, a nonlinear controller can often have attractive features such as simpler implementation, faster speed, more accuracy, or reduced control energy, which justify the more difficult design procedure [29].

The reduction-control conventional path is to reduce the model, linearize, design the control based on the reduced model, and then apply the controller to the full order model. However, for systems with dominant nonlinearities linearization fails. The same path is followed throughout this dissertation but with no linearization, instead, the nonlinear optimal controller is designed based on the POD reduced order system with a particular quadratic nonlinearity in the state and the control.

Contributions

New methods that make POD more accurate are investigated. In chapter 2, POD is applied locally to clusters instead of applying it to the global system. Each cluster contains relatively close in distance behavior within itself, and considerably far with respect to other clusters. Three different clustering schemes in time, space and space-time are introduced. For time clustering, time snapshots of the solution are grouped into clusters where the solution exhibits significantly different features and a local basis is pre-computed and assigned to each cluster. Space clustering is done in a similarly for the space vectors of the solution instead of snapshots, and finally space-time clustering is applied through a hybrid clustering scheme that combines space and time behavior together. Our methods are applied to reduce a nonlinear convective PDE system governed by the Burgers' equation for fluid flows over 1D and 2D domains.

In the same chapter, the proper orthogonal decomposition without the usual integral or inner product constraints is extended to general Hilbert spaces, such as Sobolev spaces, using functional analytic methods. It is shown that a particular tensor product space is dense in the Hilbert space where the partial differential equation (PDE) solution lives. This allows approximating the PDE solution by tensors to any desired accuracy. Optimal approximation by these tensors is shown to result in the POD using operator theoretic

arguments. This is achieved by solving a nonlinear optimization problem where the PDE solution is approximated by operators of a prescribed finite rank in the corresponding trace class 2 norm. POD modes can then be computed by solving an infinite dimensional eigenvalue problem using Hilbert-Schmidt theory. Contributions of this chapter have been published in [57], [16], [64], [65], [55], [59], [60], [58], and [11].

Nonlinear systems of quadratic type nonlinearity with the presence of a linear term are the reduced order finite dimensional version of the fluid flow systems described by the Navier Stokes equations. The one dimensional version of the Navier Stokes PDE reduces to the one dimensional Burgers' equation. In chapter 3, an analytical solution is presented for the one dimensional quadratic system with homogeneous type Dirichlet Conditions. The resulting finite dimensional nonlinear system for both PDEs has the same structure, hence the result in this note applies also to the Navier Stokes system. The same chapter includes deriving the POD model reduction, Galerkin projection, and finally the nonlinear optimal control design for the 1D Burgers equation PDE. Explicit expressions for the adjoint and state equations are derived in order to avoid numerical instabilities. The nonlinear control design is shown to be significantly better than the linearized one when the nonlinearities in the system are dominant. Contribution in this chapter has been published in [61].

In chapter 4, complete and detailed approach for the Orthogonal Locality Preserving Projections (OLPP) modes computation for the incompressible Navier Stokes PDE that governs the dynamics of the NACA 0015 airfoil fluid flow problem is presented. Close snapshots in the full order model are forced to stay close in the reduced order model by defining an optimization problem that preserves local distances. The POD reduced model is computed for the same problem. The PID closed loop flow separation control problem is shown in which fluid suction on part of the airfoil boundary is used to control flow separation on the boundary layer. Contribution in this chapter has been published in [62].

The heat equation is used as an application of a linear PDE system. The building sector in the United States consumes a large part of the energy used and is responsible for nearly 40% of greenhouse gas emissions. It is therefore economically and environmentally important to reduce the building energy consumption to realize massive energy savings. In chapter 5, a method to control room temperature in buildings is proposed. The approach is based

on a distributed parameter model represented by a three dimensional (3D) heat equation in a room with heater/cooler located at ceiling. The latter is resolved using finite element methods, and results in a model for room temperature with thousands of states. The latter is not amenable to control design. A reduced order model of only few states is then derived using POD. A Linear Quadratic Regulator (LQR) is computed based on the reduced model, and applied to the full order model to control room temperature. Contribution in this chapter has been published in [66].

Sudden disturbances in large electrical power networks cause electromechanical oscillations that have been modeled as spatially continuum systems that follow the dynamics of a second order nonlinear wave equation with constant voltage assumptions. In chapter 6, the optimal control problem is solved for both the constant voltage continuum system and the generalized time-space voltage varying PDE. First the mechanical power is used as the control input and then the varying voltage magnitude is used as the control input. Contribution in this chapter has been published in [63].

For an islanded microgrid modeled by a Kuramoto oscillators nonlinear model, the distributed optimal controller is designed in chapter 7 using the maximum principle optimization theory. Synchrony is quantified in terms of phases and droop coefficients at the inverters in the microgrid and then it is maximized. The solution existence of the distributed optimal control problem is proved and the solution is found. Performance is evaluated in a simulation case. Contribution in this chapter has been published in [56].

Chapter 2

Time, Space and Space-Time Hybrid Clustering POD

POD fails to capture the nonlinear degrees of freedom in nonlinear systems, since it assumes that data belongs to a linear space and therefore relies on the Euclidean distance as the metric to minimize. However, snapshots generated by nonlinear partial differential equations (PDEs) belong to manifolds for which the geodesics do not correspond in general to the Euclidean distance. A geodesic is a curve that is locally the shortest path between points. The global nonlinear manifold geodesic is difficult to be quantified in general but we show in this chapter that it can be approximated efficiently by local linear Euclidean distances.

In this chapter, new methods that make POD more accurate will be investigated. POD will be applied locally to clusters instead of applying it to the global system. Each cluster contains relatively close in distance behavior within itself, and considerably far with respect to other clusters. Three different clustering schemes in time, space and space-time will be introduced. For time clustering, time snapshots of the solution are grouped into clusters where the solution exhibits significantly different features and a local basis is pre-computed and assigned to each cluster. Space clustering is done in a similarly for the space vectors of the solution instead of snapshots, and finally space-time clustering is applied through a hybrid clustering scheme that combines space and time behavior together. Our methods will be applied to reduce a nonlinear convective PDE system governed by the Burgers' equation

for fluid flows over 1D and 2D domains. The next section provides a brief introduction about global POD.

2.1 Proper Orthogonal Decomposition (POD)

Proper Orthogonal Decomposition (POD) provides an optimal set of basis functions such that a low dimensional subspace is obtained by the basis functions projection on the governing PDE. The fundamental idea behind POD is as follows: Given a function $w(x,t)$ in the standard Hilbert space $L^2(\Omega,T)$ where $x \in \Omega$ for some $\Omega \subset \mathbb{R}^p$ and T is a finite time interval. The n POD basis functions set $\{\phi_i\}_{i=1}^n$ is computed by minimizing the following cost function:

$$J(\phi) := \int_0^T \int_\Omega |w(x,t) - \sum_{i=1}^n \alpha_i(t)\phi_i(x)|^2 dxdt \tag{2.1}$$

where $w(x,t)$ is the solution of the governing PDE, which is usually difficult to analytically compute. Alternatively, Numerical simulations are easier to compute and the solution is defined at the mesh locations at different times (snapshots) $\{S_i\}_{i=1}^N$, then the optimization problem becomes discrete as follows:

$$J(\phi) := \sum_k \sum_m |S(x_m,t_k) - \sum_{i=1}^n \alpha_i(t)\phi_i(x)|^2 dxdt \tag{2.2}$$

For a given snapshots matrix S, the solution of the optimization problem (2.2) up to n pod basis functions is given by the n eigenvectors that correspond to the maximum n eigenvalues in the eigenvalue problem [26]:

$$SS^T\phi = \lambda\phi. \tag{2.3}$$

2.2 Generalization of the Proper Orthogonal Decomposition

POD is known to be optimal in the sense of energy minimization. That is, the reduced order model is based on minimizing the energy error with the full order system subject to an integral constraint [26]. The energy is quantified in terms of the L^2 norm in the space domain. In this section, this result is extended to Sobolev spaces by studying its optimality using functional analytic methods. First, it is shown that a particular tensor product space is dense in the Sobolev space where the partial differential equation (PDE) solution lives. This allows approximating the PDE solution by tensors to any desired accuracy. Optimal approximation *without the usual POD integral constraint* by these tensors is shown to result in the POD using operator theoretic arguments. This is achieved by solving a nonlinear optimization problem where the PDE solution is approximated by operators of a prescribed finite rank in the corresponding trace class 2 norm. POD modes can then be computed by solving an infinite dimensional eigenvalue problem using Hilbert-Schmidt theory. Some work has been performed in extending POD to more general Hilbert spaces, see for e.g., [34, 33, 25]. However, in these works the corresponding optimizations are all subject to integral or inner product constraints on the POD coefficients. This sets apart our work from the existing literature. Let $\Omega \in \mathbb{R}^n$ be a domain (open bounded set). In this paper, PDE solutions are regarded as mapping from Ω into $\mathbb{R}$. Let $L^2(\Omega)$ denote the Hilbert space of measurable and square integrable functions $f : \Omega \to \mathbb{R}$, i.e.,

$$\|f\|^2_{L^2(\Omega)} = \int_\Omega |f(\mathbf{x})|^2 d\mathbf{x} < \infty \tag{2.4}$$

Introduce the Sobolev space $H^1(\Omega)$ as the Hilbert space of continuously differentiable functions $f : \Omega \to \mathbb{R}$ under the norm

$$\|f\|^2_{H^1(\Omega)} = \int_\Omega (|f(\mathbf{x})|^2 + \|\nabla f(\mathbf{x})\|^2) d\mathbf{x} < \infty \tag{2.5}$$

where $\nabla f(\mathbf{x})$ denotes the gradient of $f(\mathbf{x})$, and $\|.\|$ stands for the Euclidean norm in $\mathbb{R}^n$. $H^1(\Omega)$ is endowed with the inner product for $f, g \in H^1(\Omega)$,

$$< f, g >_{H^1} = \int_\Omega (f(\mathbf{x})g(\mathbf{x}) + \nabla f(\mathbf{x}) \cdot \nabla g(\mathbf{x}))d\mathbf{x} \tag{2.6}$$

where "$\cdot$" denotes the Euclidean inner product.

We will point out how our results generalize to Sobolov spaces $H^m(\Omega)$, that is, the spaces of m continuously differentiable functions under the norm

$$\|f\|^2_{H^m} := \int_\Omega (|f(\mathbf{x})|^2 + \sum_{\alpha=1}^{m} \|\nabla^\alpha f(\mathbf{x})\|^2)d\mathbf{x} < \infty \tag{2.7}$$

where $\nabla^\alpha f(\mathbf{x})$ is the partial derivative of order α of $f(\mathbf{x})$ with respect to $\mathbf{x}$.

Now define the space $L_2([0,T]) \times H^1(\Omega)$ as the Hilbert space of function defined on $[0,T] \times \Omega$ with values in $\mathbb{R}$ under the norm $w(t,\mathbf{x}) \in L_2([0,T]) \times H^1(\Omega)$

$$\|w(t,\mathbf{x})\|_2 := \big(\int_0^T \int_\Omega (|w(t,\mathbf{x})|^2 + \|\nabla w(t,\mathbf{x})\|^2)dtd\Omega\big)^{\frac{1}{2}} \tag{2.8}$$

and the inner product

$$< w(t,\mathbf{x}), v(t,\mathbf{x}) >:= \int_{[0,T]} \int_\Omega (w(t,\mathbf{x})v(t,\mathbf{x}) + \nabla w(t,\mathbf{x})\nabla v(t,\mathbf{x}))d\Omega dt \tag{2.9}$$

For arbitrary n define the tensor product $L_2([0,T]) \otimes H^1(\Omega)$ as the space

$$L_2([0,T]) \otimes H^1(\Omega) = \{\mu = \sum_{i=1}^{n} a_i(t) \otimes b_i(\mathbf{x});$$

$$a_i(t) \in L_2([0,T]), b_i(\mathbf{x}) \in H^1(\Omega); n \ arbitrary\} \tag{2.10}$$

The inner product on $L_2([0,T]) \otimes H^1(\Omega)$ is defined so that if $u = \sum_{i=1}^n a_i(t) \otimes b_i(\mathbf{x})$, $v = \sum_{j=1}^m c_j(t) \otimes d_j(\mathbf{x})$ then

$$< u, v >= \sum_{i=1}^{n} \sum_{j=1}^{m} < a_i(t), c_j(t) >_{L^2} < b_i(\mathbf{x}), d_j(\mathbf{x}) >_{H^1} \tag{2.11}$$

where $< \cdot, \cdot >_{L^2}$ denotes the inner product of $L^2[0,T]$.
Note that $L_2([0,T]) \otimes H^1(\Omega)$ under the inner product (2.11) is an inner product space. The norm induced by this inner product is

$$\beta(u) = \beta(\sum a_i \otimes b_i) := \{\sum_{i=1}^{n} \sum_{j=1}^{m} < a_i(t), a_j(t) >_{L^2} < b_i(\mathbf{x}), b_j(\mathbf{x}) >_{H^1}\}^{\frac{1}{2}}$$

The completion of $L_2([0,T]) \otimes H^1(\Omega)$ with norm β is denoted by $L_2([0,T]) \otimes_\beta H^1(\Omega)$. We show in the next proposition that the completion is in fact equal to the Hilbert space $L_2([0,T]) \times H^1(\Omega)$.

Proposition 1.

$$L_2([0,T]) \otimes_\beta H^1(\Omega) = L_2([0,T]) \times H^1(\Omega)$$

Proof:

Let $u \in L_2([0,T]) \otimes H^1(\Omega), u = \sum_{i=1}^n a_i(t) \otimes b_i(\mathbf{x})$ where $a_i(t) \in L_2([0,T]), b_i(\mathbf{x}) \in H^1(\Omega)$ and associate to u the function

$$f(t, \mathbf{x}) := \sum_{i=1}^{n} a_i(t) b_i(\mathbf{x}) \tag{2.12}$$

Note that $f \in L_2([0,T]) \times H^1(\Omega)$. Define the map

$$\mathcal{L} : L_2([0,T]) \otimes H^1(\Omega) \to L_2([0,T]) \times H^1(\Omega)$$
$$u \to f = \mathcal{L}u$$

$\mathcal{L}$ is linear and norm preserving since

$$\begin{aligned} \|f\|_g^2 &= \int_{[0,T]} \int_\Omega (|f(t,\mathbf{x})|^2 + \|\nabla f(t,\mathbf{x})\|^2) d\Omega dt \\ &= \beta(u) \end{aligned} \tag{2.13}$$

Therefore, the completion of $L_2([0,T]) \otimes H^1(\Omega)$ in the β norm is equal to its closure in $L_2([0,T]) \times H^1(\Omega)$. Now, we need to show that the closure of $L_2([0,T]) \otimes H^1(\Omega)$,

$$L_2([0,T]) \otimes_\beta H^1(\Omega) = L_2([0,T]) \times H^1(\Omega) \tag{2.14}$$

To this end it suffices to show that the orthogonal complement of $L_2([0,T]) \otimes H^1(\Omega)$ is $\{0\}$ in $L_2([0,T]) \times H^1(\Omega)$.
Let $\mathbf{F} = (F_1, F_2) \in L_2([0,T]) \times H^1(\Omega)$ and $\forall u \otimes v \in L_2([0,T]) \otimes H^1(\Omega)$,

$$< \mathbf{F}, u \otimes v > = < F_1, u >_{L_2} < F_2, v >_{H^1} = 0$$

since u is arbitrary in $L_2([0,T])$ and v is arbitrary in $H^1(\Omega)$

$$\begin{aligned} < F_1, u > = 0 \Rightarrow F_1 = 0 \ a.e. \\ < F_2, v > = 0 \Rightarrow F_2 = 0 \end{aligned}$$

Therefore (2.14) holds and the proposition is proved. ■

The proposition shows that any PDE solution $w(t,\mathbf{x})$ in $L_2([0,T]) \times H^1(\Omega)$ can be approximated as closely as desired by functions of the form $\sum_{i=1}^n a_i(t)\varphi_i(\mathbf{x}), t \in [0,T], \mathbf{x} \in \Omega$ in the norm $\|.\|_2$, that is, as $n \to \infty$ we have

$$\|w(t,\mathbf{x}) - \sum_{i=1}^n a_i(t)\varphi_i(\mathbf{x})\|_2 \to 0 \tag{2.15}$$

For fixed n, define the shortest distance minimization in the norm $\|.\|_2$ from the function $w(t,\mathbf{x})$ to the set $\mathcal{S}$, by

$$\mu = \inf_{f \in \mathcal{S}} \|w(t,\mathbf{x}) - f(t,\mathbf{x})\|_2 \tag{2.16}$$

where

$$\mathcal{S} := \{\mathbf{F} = \sum_{i=1}^{n} a_i(t)\varphi_i(\mathbf{x}); a_i \in L_2([0,T]), \varphi_i \in H^1(\Omega)\} \tag{2.17}$$

It is important to note at this point that the minimization (2.16) is *not subject to any constraint* besides the minimizer belonging to $\mathcal{S}$ as is for instance the case in [34, 33, 25], i.e., we do not impose, a priori, any relationship between the POD coefficients $a_i(t)$ and φ_i, $i = 1, 2, \cdots$.

Following [14], let Γ be the integral operator with kernel $w(t,\mathbf{x})$:

$$\begin{aligned} &\Gamma : H^1(\Omega) \to L^2[0,T] \\ &\phi \to (\Gamma\phi)(t) = \int_\Omega (w(t,\mathbf{x})\phi(\mathbf{x}) + \nabla w(t,\mathbf{x}) \cdot \nabla\phi(\mathbf{x}))d\mathbf{x} \end{aligned} \tag{2.18}$$

It can be shown that such an operator is compact, that is, an operator that maps bounded sets into pre-compact sets. In fact, for $w(t,\mathbf{x}) \in L_2([0,T]) \times H^1(\Omega)$, Γ is a trace class 2 operator, that is, the sum of all the singular values squared is finite (see for, e.g., [68]). The class of trace class 2 operates from $H^1(\Omega)$ into $L_2([0,T])$ will henceforth be denoted by $\mathcal{C}_2$.

Let us define the adjoint of Γ, $\Gamma^\star$, as the operator acting from $L^2[0,T]$ into $H^1(\Omega)$ as for

$f(\mathbf{x}) \in H^1(\Omega), g(t) \in L^2[0,T]$,

$$
\begin{aligned}
&< \Gamma f, g >_{L^2} \\
&:= \int_0^T \int_\Omega [w(t,\mathbf{x}) f(\mathbf{x}) + \nabla w(t,\mathbf{x}) \cdot \nabla f(\mathbf{x})] d\mathbf{x} \cdot g(t) dt \\
&= \int_\Omega f(\mathbf{x}) \int_0^T [w(t,\mathbf{x}) g(t) + \nabla^T (t,\mathbf{x}) g(t)] dt \cdot \nabla f(\mathbf{x}) d\mathbf{x} \\
&=:< f, \Gamma^\star g >_{H^1}
\end{aligned} \tag{2.19}
$$

This shows that

$$
(\Gamma^\star g)(t) = \int_{[0,T]} w(t,\mathbf{x}) g(t) dt \tag{2.20}
$$

Using polar representation of compact operators [68]

$$
\Gamma = U(\Gamma^\star \Gamma)^{\frac{1}{2}}
$$

where U is a partial isometry and $(\Gamma^\star\Gamma)^{\frac{1}{2}}$ is the square root of T, which is also trace class 2 operator, and admits a spectral factorization of the form [68]

$$
(\Gamma^\star \Gamma)^{\frac{1}{2}} = \sum_i \lambda_i \nu_i \otimes \nu_i \tag{2.21}
$$

where $\lambda_i > 0$, $\lambda_i \searrow 0$ as $i \uparrow \infty$, are the eigenvalues of $(\Gamma^\star\Gamma)^{\frac{1}{2}}$, and ν_i form the corresponding orthonormal sequence of eigenvectors, i.e., $(\Gamma^\star\Gamma)^{\frac{1}{2}} \nu_i = \lambda_i \nu_i,\ i = 1, 2, \cdots$. Putting $U\nu_i =: \psi_i$, we can write

$$
\Gamma = \sum_i \lambda_i \ \nu_i \otimes \psi_i \tag{2.22}
$$

Both $\{\nu_i\}$ and $\{\psi_i\}$ are orthonormal sequences in $L^2[0,T]$ and $H^1(\Omega)$, respectively. The sum (2.22) has either a finite or countably infinite number of terms. The above representation is unique.

Noting that the polar decomposition of $\Gamma^\star = U^\star(\Gamma\Gamma^\star)^{\frac{1}{2}}$, a similar argument yields

$$(\Gamma\Gamma^\star)^{\frac{1}{2}} = \sum_i \lambda_i \psi_i \otimes \psi_i \tag{2.23}$$

$$\Gamma^\star = \sum_i \lambda_i \psi_i \otimes \nu_i \tag{2.24}$$

which shows that α_i from an orthonormal sequence of eigenvectors of $(\Gamma\Gamma^\star)^{\frac{1}{2}}$ corresponding to the eigenvalues λ_i. From (2.21) and (2.24) it follows that

$$\Gamma\psi_i = U(\Gamma^\star\Gamma)^{\frac{1}{2}}\psi_i = \lambda_i \nu_i \tag{2.25}$$

$$\Gamma^\star\nu_i = U^\star(\Gamma\Gamma^\star)^{\frac{1}{2}}\nu_i = \lambda_i \psi_i \tag{2.26}$$

We say that ψ_i and ν_i constitute a Schmidt pair [53]. In terms of integral operators expressions, identities (2.25) and (2.26) can be written, respectively, as

$$\nu_i(t) = \int_\Omega [w(t,\mathbf{x})\psi_i(\mathbf{x}) + \nabla w(t,\mathbf{x}) \cdot \nabla\psi_i(\mathbf{x})]d\mathbf{x} \tag{2.27}$$

$$\psi_i(\mathbf{x}) = \int_0^T w(t,\mathbf{x})\nu_i(t)dt \tag{2.28}$$

In terms of the eigenvalues λ_i's of Γ, its trace class 2 norm $\|\cdot\|_{\mathcal{C}_2}$ is given by [68]

$$\|\Gamma\|_{\mathcal{C}_2} = \Big(\sum_i \lambda_i^2\Big)^{\frac{1}{2}} \tag{2.29}$$

Note that since the operator Γ is trace class 2, the sum in (2.29) is finite. The Trace class 2 norm is also induced by the operator inner product defined by (2.32).

By interpreting each elements of the subspace $\mathcal{S}$ defined in (2.17) as a trace class 2 operator as we did for $w(t,\mathbf{x})$, we see that $\mathcal{S}$ is the subspace of trace class 2 operators of rank n, i.e.,

$$\begin{aligned}\mathcal{S} =& \{s = \textstyle\sum_{j=1}^n \vartheta_j\ f_j(t) \otimes \chi_j(\mathbf{x}) : \\ & f_j(t) \in L^2([0,T]), \chi_j(\mathbf{x}) \in H^1(\Omega),\ \vartheta_j \in \mathbb{R}\}\end{aligned} \tag{2.30}$$

In addition, the distance minimization (2.16) is then the minimal distance from Γ to trace class 2 operators of rank n. In other terms, we have

$$\mu = \min_{s \in \mathcal{S}} \|\Gamma - s\|_{\mathcal{C}_2} \tag{2.31}$$

The space of trace class 2 operators is in fact a Hilbert space with the inner product [68], denoted $(\cdot,\ \cdot)$, if A and B are two trace class 2 operators defined on $H^1(\Omega)$,

$$(A, B) := tr(B^\star A) \tag{2.32}$$

where tr denotes the trace, which in this case is given by the sum of the eigenvalues of the operator $B^\star A$ which is necessarily finite [68]. Note that the inner product (2.32) induces the trace class 2 norm $\|A\|_{\mathcal{C}_2} = \big(tr(A^\star A)\big)^{\frac{1}{2}}$.

Theorem 2.1.

$$\begin{aligned}
\mu &= \min_{\int \in \mathcal{S}} \|\Gamma - \int\|_{\mathcal{C}_2} \\
&= \min_{\substack{\alpha_i \in \mathbb{R}, \\ f_i \in H^1(\Omega), \\ g_i \in L_2([0,T]), \\ \|f_i\|_{H^1} = \|g_i\|_{L_2} = 1}} \|\Gamma - \sum_{i=1}^{n} \alpha_i f_i \otimes g_i\|_{\mathcal{C}_2} \\
&= \|\sum_{i=n+1}^{\infty} \lambda_i \nu_i \otimes \psi_i\|_{\mathcal{C}_2} \\
&= \Big(\sum_{i=n+1}^{\infty} \lambda_i^2\Big)^{\frac{1}{2}}
\end{aligned} \tag{2.33}$$

Proof: For simplicity we shall prove (2.33) only for $n = 1$. The general case can be proved by induction. Let then

$$\int = \alpha_1 f_1 \otimes g_1,\ \alpha_1 \in \mathbb{R},\ f_1 \in H^1(\Omega),\ g_1 \in L_2([0,T])$$

For $n = 1$ (2.33) becomes

$$\mu = \min_{\substack{\alpha_1 \in \mathbb{R} \\ f_1 \in H^1(\Omega), \\ g_1 \in L_2([0,T]), \\ \|f_1\|_{H^1} = \|g_1\|_{L_2} = 1}} \|\Gamma - \alpha_1 f_1 \otimes g_1\|_{\mathcal{C}_2} \tag{2.34}$$

Let $\{\varphi_i\}$ be an orthonormal basis of $H^1(\Omega)$ with $\varphi_1 = f_1$ then by definition of trace class 2 norm:

$$\begin{aligned} \|\Gamma - \alpha_1 \varphi_1 \otimes g_1\|_{\mathcal{C}_2}^2 &= \sum_{i=1}^{\infty} \|(\Gamma - \alpha_1 f_1 \otimes g_1)\varphi_i\|_{L_2}^2 \\ &= \sum_{i=1}^{\infty} \|\Gamma\varphi_i - \alpha_1 < \varphi_1, \varphi_i >_{H^1(\Omega)} g_1\|_{L_2}^2; \end{aligned}$$

note that $< \varphi_1, \varphi_i >_{H^1(\Omega)} = 0 \qquad \forall i \geq 2$

$$\begin{aligned} &= \sum_{i=2}^{\infty} \|\Gamma\varphi_i\|_{L_2}^2 + \|\Gamma\varphi_1 - \alpha_1 g_1\|_{L_2}^2 \\ &= \|\Gamma\|_{\mathcal{C}_2}^2 - \|\Gamma\varphi_1\|_{L^2}^2 + \|\Gamma\varphi_1 - \alpha_1 g_1\|_{L^2}^2 \end{aligned} \tag{2.35}$$

We need to minimize (2.35) with respect to $\varphi_1 \in H^1(\Omega), \|\varphi_1\| = 1, g_1 \in L^2([0,T]), \|g_1\|_{L^2} = 1$. To do so we need to maximize $\|\Gamma\varphi_1\|_{L^2}$ w.r.t. φ_1 and minimize $\|\Gamma\varphi_1 - \alpha_1 g_1\|_{L^2}$ w.r.t. φ_1 and g_1. We get then

$$\arg \max_{\substack{\varphi_1 \in H^1(\Omega), \\ \|\varphi_1\|_{H^1(\Omega)} = 1}} \|\Gamma\varphi_1\|_{L_2} = \psi_1(x)$$

$$\arg \min_{\substack{\alpha_1 \in \mathbb{R}, \\ \|g_1\|_{L^2} = 1}} \|\Gamma\varphi_1 - \alpha_1 g_1\|_{L_2} \to \alpha_1 = \lambda, g_1 = \nu_1$$

since $\Gamma\varphi_1 = \sum_{i=1}^{\infty} \lambda_i < \psi_i, \psi >_{H^1} \nu_i = \lambda_1 \nu_1$, and the Theorem is proved.

remark 1. *The above results generalize to the Sobolev spaces $H^m(\Omega)$ by using the following inner product*

$$< f, g >_{H^m} := \int_\Omega \Big(f(\mathbf{x})g(\mathbf{x}) + \sum_{\alpha=1}^{m} \big(\nabla^\alpha f(\mathbf{x}) \cdot \nabla^\alpha g(\mathbf{x}) \big) \Big) d\mathbf{x}$$

instead of the inner product in H^1 defined in (2.6).

2.3 The Burgers' Equation

The Burgers' equation is a nonlinear PDE with a quadratic type nonlinearity. The 1-D viscous Burgers' equation is given by [7]:

$$\frac{\partial w}{\partial t} = \frac{1}{R_e} \frac{\partial^2 w}{\partial x^2} - w \frac{\partial w}{\partial x} \tag{2.36}$$

where $x \in [a, b]$ is the space variable, $t \in [t_0, t_f]$ is the time variable, $1/R_e$ is the viscosity constant and the initial condition is:

$$w(x, t_0) = w_0(x) \tag{2.37}$$

with Dirichlet boundary conditions specified as:

$$\begin{pmatrix} w(a,t) \\ w(b,t) \end{pmatrix} = \begin{pmatrix} u_a(t) \\ u_b(t) \end{pmatrix} := u(t) \tag{2.38}$$

For $x \in [0, 100]$ and boundary conditions $\begin{pmatrix} w(0,t) \\ w(100,t) \end{pmatrix} = \begin{pmatrix} 2 \\ 1 \end{pmatrix}$, numerical solution at three different times is shown in Fig. 2.1.

The 2D Burgers' equation is given by [7]:

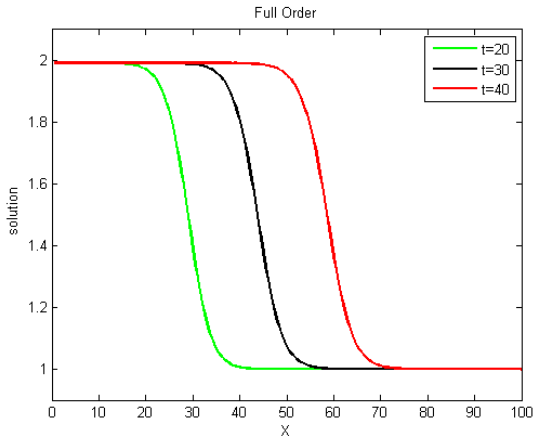

Figure 2.1: 1D Full order solution at three different times

$$\frac{\partial w}{\partial t} + w(\frac{\partial w}{\partial x} + \frac{\partial w}{\partial y}) = \frac{1}{R_e}(\frac{\partial^2 w}{\partial x^2} + \frac{\partial^2 w}{\partial y^2}) \tag{2.39}$$

where x and y are the spacial variables, t is the time variable and $1/R_e$ is the viscosity constant such that R_e is analogues to the Reynolds number that appears in the Navier Stokes equations. The spatial domain is shown in Figure 2.2 where the fluid enters from the left boundary in a specified constant velocity and pases around an obstacle as shown. The 2D Burgers' equation PDE shares the same nonlinearity as the Navier stokes PDE. It has the same quadratic nonlinearity and can be used to model incompressible fluid flows.

Figure 2.2: 2D Geometry

The 2D Burgers' equation full order system is solved numerically in Matlab using 2000 space mesh elements and $R_e = 300$, on the space domain shown in Fig. 2.3 which shows

the solution at $t = 30$ seconds. This domain models the velocity of a fluid with a constant Dirichlet parabolic velocity profile at the left boundary that is maximum in the middle and zero in the top and bottom. The fluid passes over an obstacle to show the velocity behavior that the 2D Burgers' equation models.

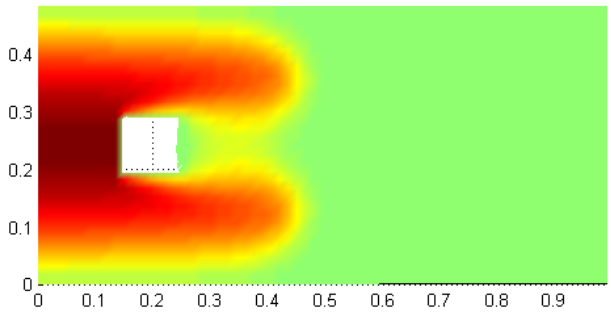

Figure 2.3: 2D Full order solution at t=30

2.4 Clustered POD

K- means algorithm groups together nearby locations according to their relative clustering distances. The clustering distance is defined as follows:

$$d(E_i, E_j) = \sqrt{(E_i - E_j)^T (E_i - E_j)} \tag{2.40}$$

where d is the Euclidean distance between two time snapshots E_i and E_j. These vectors contain the solution at times i and j respectively for all space location times.

Suppose we want to group N time snapshots $\{E_i\}_{i=1}^N$ into T clusters $\{\chi_j\}_{j=1}^T$, we first randomly choose T time snapshots as centroids $\{E_{c_j}\}_{j=1}^T$. Then the distance between each time snapshot and the centroid is calculated as:

$$d(E_i, E_{c_j}) = \sqrt{(E_i - E_j)^T (E_i - E_{c_j})} \tag{2.41}$$

Let c_i be the argument of the minimum distance between E_i and E_{c_j}:

$$c_i = \arg \min_{j=1,\cdots,T} d(E_i, E_{c_j}) \tag{2.42}$$

Then the new centroids would be:

$$E_{c_j} = \frac{\sum_{i=1}^{N} 1_{c_i=j} E_i}{\sum_{i=1}^{N} 1_{c_i=j}} \tag{2.43}$$

where $j = 1, \cdots T$ and $1_{c_i=j} = 1$ if $c_i = j$ and zero otherwise. Then the last step is to assign each time snapshot E_i to the cluster χ_{c_j}.

2.4.1 Time Snapshots Clustering (TSC) POD

The time snapshots are grouped into clusters where the solution exhibits significantly different features. A cluster is a group that contains states which are close in some defined distance. Time Clustering for the 1D equation is shown in Figure 2.4. Local bases are pre-computed and assigned to each cluster. The set of pre-computed time snapshots are partitioned into T clusters using K-means clustering algorithm discussed in the previous section.

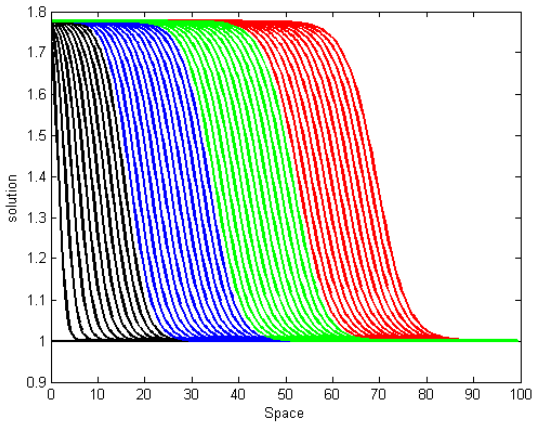

Figure 2.4: TSC 4 Clusters

Reduced order bases are now computed for each cluster as follows:

Let the number of time snapshots in cluster k be N^k, the $N^k \times N^k$ correlation matrix L^k is defined by [26]:

$$L^k_{i,j} = \left\langle E^k_i, E^k_j \right\rangle \tag{2.44}$$

is constructed, where $\langle , \rangle$ denotes the Euclidean inner product of time snapshots E^k. With R^k denotes the number of TSC POD modes to be constructed for cluster k, the first R^k eigenvalues of largest magnitude, $\{\lambda\}_{i=1}^{R^k}$, of L^k are found. They are sorted in descending order, and their corresponding eigenvectors $\{v^k\}_{i=1}^{R^k}$ are calculated. Each eigenvector is normalized so that

$$\left\|v_i^k\right\|^2 = \frac{1}{\lambda_i^k} \tag{2.45}$$

The orthonormal TSC POD basis set $\{\phi_i^k\}_{i=1}^{R^k}$ is constructed according to:

$$\phi_i^k = \sum_{j=1}^{N^k} v_{i,j}^k E_j^k \tag{2.46}$$

where $v_{i,j}^k$ is the j^{th} component of v_i^k . The 1-D Burgers' equation solution time snapshots were grouped into 4 clusters as shown in Figure 2.4 and the first four modes of each cluster are shown in Figure 2.5.

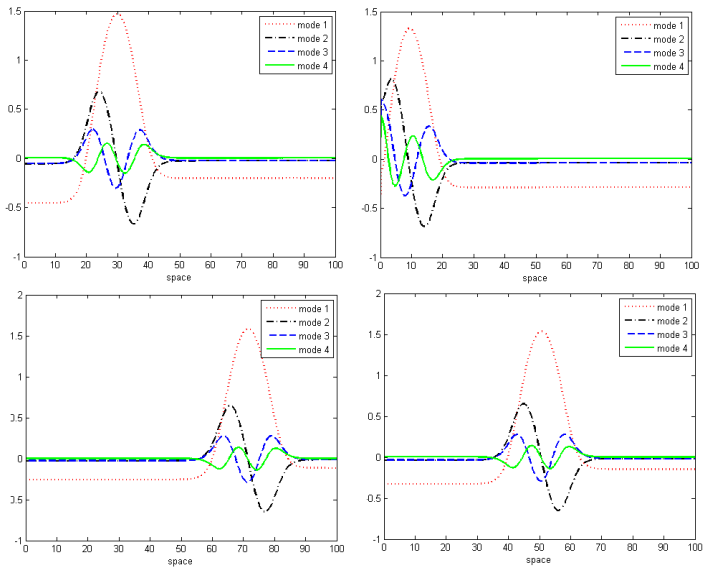

Figure 2.5: First 4 modes of TSC POD in 4 clusters

The 2-D Burgers' equation solution time snapshots were grouped into 8 clusters. The first four modes of cluster 1 are shown in Figure 2.6.

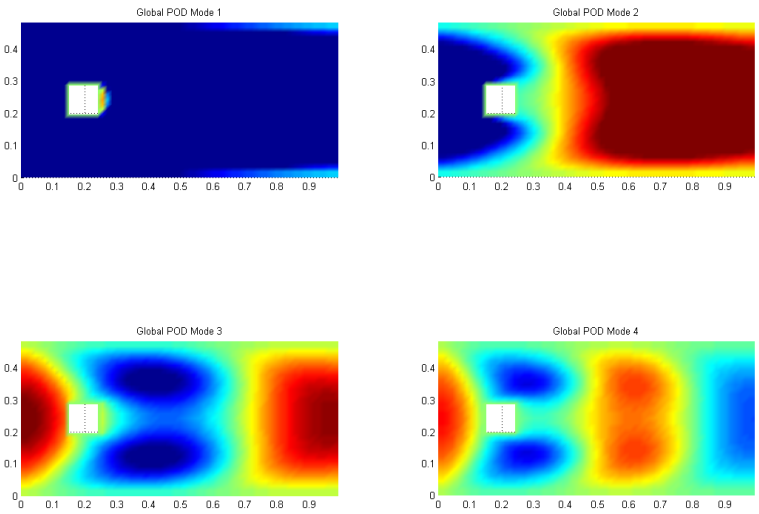

Figure 2.6: 2D First four modes of TSC POD in cluster 1

Then the constructed local reduced order bases are projected to their corresponding locations in the full solution as follows:

$$\{U_{TSC}\}_{k=1}^{T} \approx \{\sum_{i=1}^{R^k} \alpha_i^k \phi_i^k\}_{k=1}^{T} \tag{2.47}$$

2.4.2 Space Vector Clustering (SVC) POD

In TSC POD discussed in the last section, time snapshots are clustered. In this section, the solution space domain is clustered where the solution exhibits significantly different features. Local bases are pre-computed and assigned to each cluster. The set of pre-computed solution space domain is partitioned into T clusters using K-means clustering algorithm. Space vector clustering is shown in Figure 2.7.

Let the number of space vectors in cluster k be N^k, the $N^k \times N^k$ correlation matrix L^k is defined by:

$$L_{i,j}^k = \langle W_i^k, W_j^k \rangle \tag{2.48}$$

is constructed with R^k denotes the number of SVC POD modes to be constructed for cluster k, the first R^k eigenvalues of largest magnitude, $\{\lambda\}_{i=1}^{R^k}$, of L^k are found. They

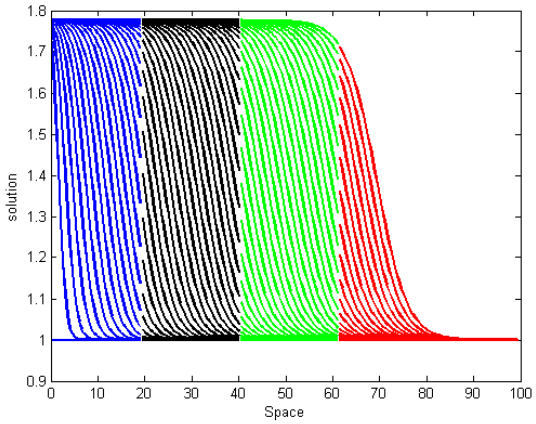

Figure 2.7: SVC 4 clusters

are sorted in descending order, and their corresponding eigenvectors $\{v^k\}_{i=1}^{R^k}$ are calculated. Each eigenvector is normalized so that

$$\left\|v_i^k\right\|^2 = \frac{1}{\lambda_i^k} \tag{2.49}$$

The orthonormal SVC POD basis set $\{\phi_i^k\}_{i=1}^{R^k}$ is constructed according to:

$$\phi_i^k = \sum_{j=1}^{N^k} v_{i,j}^k W_j^k \tag{2.50}$$

where $v_{i,j}^k$ is the j^{th} component of v_i^k . The 1-D Burgers' equation solution space vectors were grouped into 4 clusters and the first four modes of each cluster are shown in Figure 2.8

The 2-D Burgers' equation solution space vectors were grouped into 8 clusters. The first four modes of cluster 1 are shown in Figure 2.9.

The SVC modes in Figure 2.9 are different from the modes of the global POD because they are based only on one cluster that includes relatively close states. These states are clearly the ones on the far left of the domain that share a relatively higher fluid velocities most of the time. We should notice from the modes of this cluster that locations which are close to the top and bottom of the left side do not appear to belong to this cluster. This is due to the fact that they have lower velocities most of the time so they are grouped in some other clusters other than the one shown in Figure 2.9.

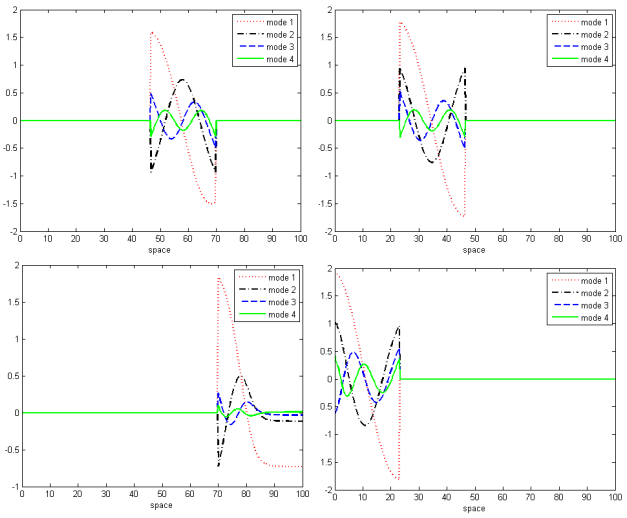

Figure 2.8: First 4 modes of SVC POD in 4 clusters

Now we have computed the clusters with their local reduced order bases, the last step is the projection to the full solution. The constructed local reduced order bases are projected to their corresponding locations in the full solution as follows:

$$\{U_{SVC}\}_{k=1}^{T} \approx \{\sum_{i=1}^{R^k} \alpha_i^k \phi_i^k\}_{k=1}^{T} \tag{2.51}$$

2.4.3 Space-Time Hybrid (STH) POD

In this section, the whole solution space and time domains is clustered using K-means algorithm. Note that clusters now contain space-time points instead of time snapshots or space vectors in the previous sections. However, these points are then reshaped to form either time or space vectors in each cluster. STH clustering is shown in Figure 2.10. Note that this is not uniform for all clusters, meaning that some clusters could contain time snapshot vectors while others contain space vectors, we will call them STH vectors. The optimum choice will be investigated in future work. Reduced order bases are computed for each cluster as follows: Let the number of STH vectors in cluster k be N^k, the $N^k \times N^k$ correlation matrix L^k is defined by:

$$L_{i,j}^k = \left\langle H_i^k, H_j^k \right\rangle \tag{2.52}$$

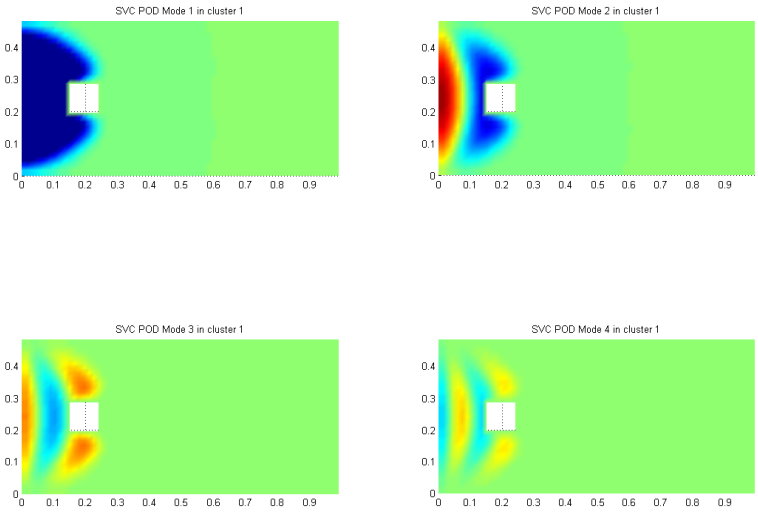

Figure 2.9: 2D First four modes of SVC POD in cluster 1

is constructed with R^k denotes the number of STH POD modes to be constructed for cluster k, the first R^k eigenvalues of largest magnitude, $\{\lambda\}_{i=1}^{R^k}$, of L^k are found. They are sorted in descending order, and their corresponding eigenvectors $\{v^k\}_{i=1}^{R^k}$ are calculated. Each eigenvector is normalized so that

$$\left\|v_i^k\right\|^2 = \frac{1}{\lambda_i^k} \tag{2.53}$$

The orthonormal STH POD basis set $\{\phi_i^k\}_{i=1}^{R^k}$ is constructed according to:

$$\phi_i^k = \sum\nolimits_{j=1}^{N^k} v_{i,j}^k H_j^k \tag{2.54}$$

where $v_{i,j}^k$ is the j^{th} component of v_i^k .

It is important to record the original ordering of snapshots because we need this in the projection process. The constructed local reduced order bases are projected to their corresponding locations in the full solution as follows:

$$\{U_{STH}\}_{k=1}^T \approx \{\sum\nolimits_{i=1}^{R^k} \alpha_i^k \phi_i^k\}_{k=1}^T \tag{2.55}$$

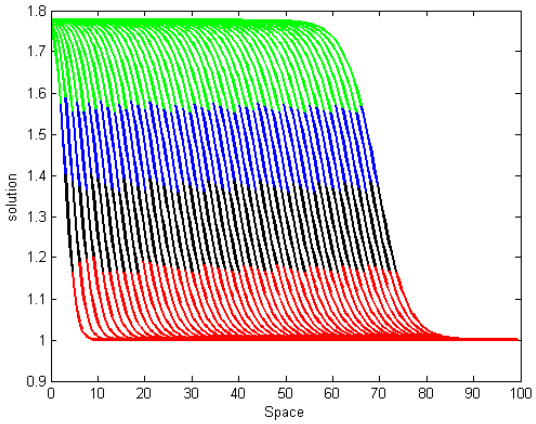

Figure 2.10: STH 4 clusters

Performance comparison between reduced order models using all methods presented in this chapter compared with global POD for the 1D Burgers' equation is shown in Figure 2.11 with the full number of states $N = 500$ is reduced to $R = 15$ where the space domain is $x \in [0, 100]$ and the time domain is $t \in [0, 50]$.

The error norms at $t = 30$ for the two methods when reducing the order from 500 states to 15 states are shown in Table 2.1.

Table 2.1: Error norms at $t = 30$ for the 1D equation for different POD versions

Method	Error norm at $t = 30$
Global POD	0.3080
TSC POD	0.0352
SVC POD	0.0012
STH POD	0.0009

The reduced order systems for the 2D domain Burgers' equation problem using the three methods presented in this paper along with global POD is shown in Figure 2.12 with full number of states $N = 2000$ is reduced to $R = 10$ states.

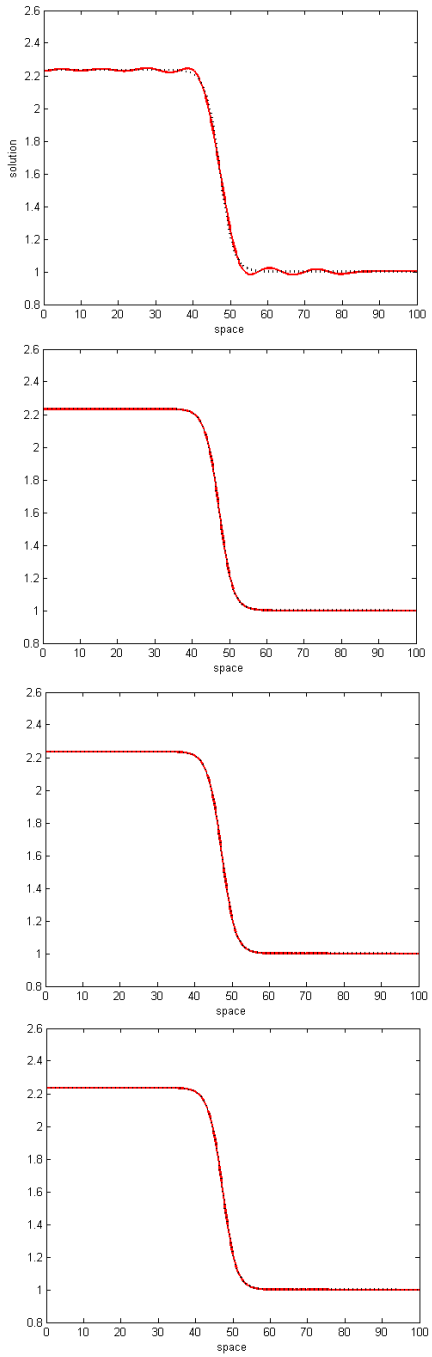

Figure 2.11: 1D Burgers equation model reduction. Dotted blacks are the full order models and reds are the reduced ones using (starting from the top): Global, TSC, SVC and STH POD, all at t=30

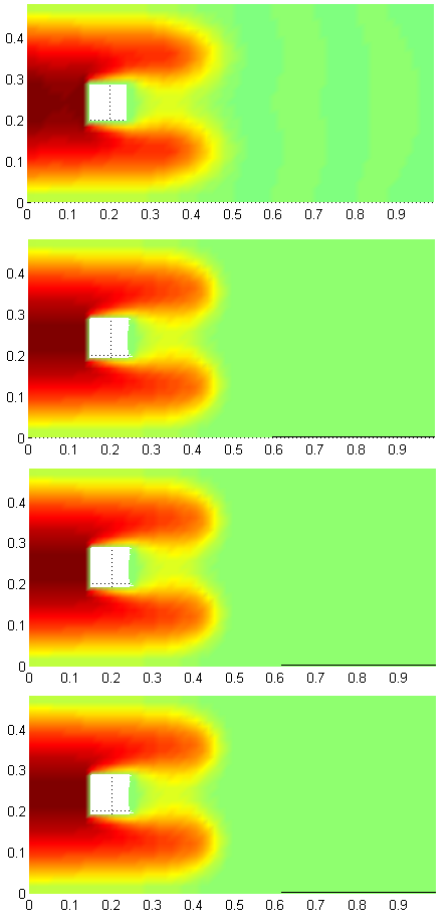

Figure 2.12: 2D Burgers equation model reduction using (starting from the top): Global, TSC, SVC and STH POD

Chapter 3

Nonlinear Control of the Reduced Order 1D Burgers' Equation

Nonlinear systems of quadratic type nonlinearity with the presence of a linear term are the reduced order finite dimensional version of the fluid flow systems described by the Navier Stokes equations. The one dimensional version of the Navier Stokes PDE reduces to the one dimensional Burgers' equation. In this chapter, we present an analytical solution for the one dimensional quadratic system with homogeneous type Dirichlet Conditions. The resulting finite dimensional nonlinear system for both PDEs has the same structure, hence the result in this note applies also to the Navier Stokes system. The remainder of this chapter includes deriving the POD model reduction, Galerkin projection, and finally the nonlinear optimal control design for the 1D Burgers equation PDE. Explicit expressions for the adjoint and state equations are derived in order to avoid numerical instabilities. The nonlinear control design is shown to be significantly better than the linearized one when the nonlinearities in the system are dominant.

The one dimensional Burgers' equation is given by:

$$\frac{\partial w}{\partial t} = \frac{1}{Re}\frac{\partial^2 w}{\partial x^2} - w\frac{\partial w}{\partial x} \tag{3.1}$$

where $1/Re$ is the viscosity term that plays a similar role that is done by the Reynolds number in the Navier Stokes equations. If the solution $w(t, x)$ is approximated by a linear

combination of the POD basis functions as:

$$w(x,t) = \sum_{i=1}^{N} \alpha_i(t)\phi_i(x) \tag{3.2}$$

where $\phi_i(x)$ is the POD basis i and $\alpha_i(t)$ is the corresponding ith temporal coefficient, and the expression in (3.2) is used in (3.1) and Galerkin projection is performed, we get a quadratic nonlinear system of the dynamics of the temporal coefficients $\alpha_i(x)$. In this chapter we give an analytical expression for the solution of this system in the case of homogeneous Dirichlet boundary conditions.

3.1 Galerkin Projection

The solution $w(t,x)$ of the distributed parameter system is approximated by a linear combination of the POD basis functions as:

$$w(x,t) = \sum_{i=1}^{N} \alpha_i(t)\phi_i(x) \tag{3.3}$$

The expression in (3.3) is used in the 1D Burgers' PDE:

$$\frac{\partial w}{\partial t} = \frac{1}{Re}\frac{\partial^2 w}{\partial x^2} - w\frac{\partial w}{\partial x} \tag{3.4}$$

and Galerkin projection is performed by multiplying (3.4) by the basis functions $\phi_j(x)$ and integrating over the spatial domain. Due to the orthogonality of POD basis, the left hand side of (3.4) becomes:

$$\begin{aligned}\int_\Omega \frac{\partial w(x,t)}{\partial t}\phi_j(x)dx = \int_\Omega \frac{\partial \sum_{i=1}^{N} \alpha_i(t)\phi_i(x)}{\partial t}\phi_j(x)dx \\ = \dot{\alpha}_j(t)\end{aligned} \tag{3.5}$$

Integrating the linear diffusion term by parts yields:

$$\begin{aligned}\int_\Omega \frac{1}{Re}\frac{\partial^2 w}{\partial x^2}\phi_j(x)dx &= \frac{1}{Re}\left(\frac{\partial w}{\partial x}\phi_j\Big|_{\partial\Omega} - \int_\Omega \frac{\partial w}{\partial x}\frac{d\phi_j}{dx}dx\right) \\ &= \frac{1}{Re}\left(\frac{\partial w(b)}{\partial x}\phi_j(b) - \frac{\partial w(a)}{\partial x}\phi_j(a) - \int_a^b \frac{\partial w}{\partial x}\frac{d\phi_j}{dx}dx\right) \qquad (3.6)\end{aligned}$$

The spatial derivatives at the boundaries can be approximated as:

$$\frac{\partial w(a,t)}{\partial x} = \frac{w(a+h,t) - w(a,t)}{h} \qquad (3.7)$$

$$\frac{\partial w(b,t)}{\partial x} = \frac{w(b,t) - w(b-h,t)}{h} \qquad (3.8)$$

where h is a sufficiently small mesh step size, $w(a,t)$ and $w(b,t)$ are the control inputs defined as:

$$\begin{pmatrix} w(a,t) \\ w(b,t) \end{pmatrix} = \begin{pmatrix} u_a(t) \\ u_b(t) \end{pmatrix} := u(t) \qquad (3.9)$$

and

$$w(a+h,t) = \sum_{i=1}^{N} \alpha_i(t)\phi_i(a+h) \qquad (3.10)$$

$$w(b-h,t) = \sum_{i=1}^{N} \alpha_i(t)\phi_i(b-h) \qquad (3.11)$$

The linear term then has the form $A\alpha + Bu$ where

$$A_{ji} = -\frac{1}{Re}\left(\frac{\phi_i(b-h)\phi_j(b)}{h} + \frac{\phi_i(a+h)\phi_j(a)}{h} + \int_a^b \frac{d\phi_i}{dx}\frac{d\phi_j}{dx}dx\right) \qquad (3.12)$$

and B is the Nx2 matrix such that:

$$B_{j1} = \frac{\phi_j(a)}{hRe}, \quad B_{j2} = \frac{\phi_j(b)}{hRe} \qquad (3.13)$$

The nonlinear term in (3.4) can be written as $\frac{1}{2}\frac{\partial w^2}{\partial x}$, so the Galerkin projection becomes:

$$\begin{aligned} -\int_\Omega \frac{1}{2}\frac{\partial w^2}{\partial x}\phi_j(x)dx &= -\left(\frac{w^2}{2}\phi_j\Big|_{\partial\Omega} - \int_\Omega \frac{w^2}{2}\frac{d\phi_j}{dx}dx\right) \\ &= -\frac{1}{2}\left(w^2(b)\phi_j(b) - w^2(a)\phi_j(a) - \int_a^b w^2\frac{d\phi_j}{dx}dx\right) \end{aligned} \tag{3.14}$$

The nonlinear term then has the form $N(\alpha) + B'u^2$ where u^2 is the vector of the term by term squares of the inputs vector u described in (3.9):

$$u^2 = \begin{pmatrix} u_1^2 \\ u_2^2 \end{pmatrix} \tag{3.15}$$

and,

$$N(\alpha) = \frac{1}{2}\int_a^b (\sum_{i=1}^N a_i(t)\phi_i(x))^2\frac{d\phi_j(x)}{dx}dx \tag{3.16}$$

where B' is the Nx2 matrix such that:

$$B'_{j1} = \frac{\phi_j(a)}{2}, \quad B'_{j2} = -\frac{\phi_j(b)}{2} \tag{3.17}$$

Finally, the initial condition:

$$w(x, t_0) = w_0(x) \tag{3.18}$$

is projected onto the POD basis to find the initial values for α. The complete reduced order system becomes:

$$\begin{aligned} \dot{\alpha} &= A\alpha + N(\alpha) + Bu + B'u^2 \\ \alpha(0) &= \alpha_0. \end{aligned} \tag{3.19}$$

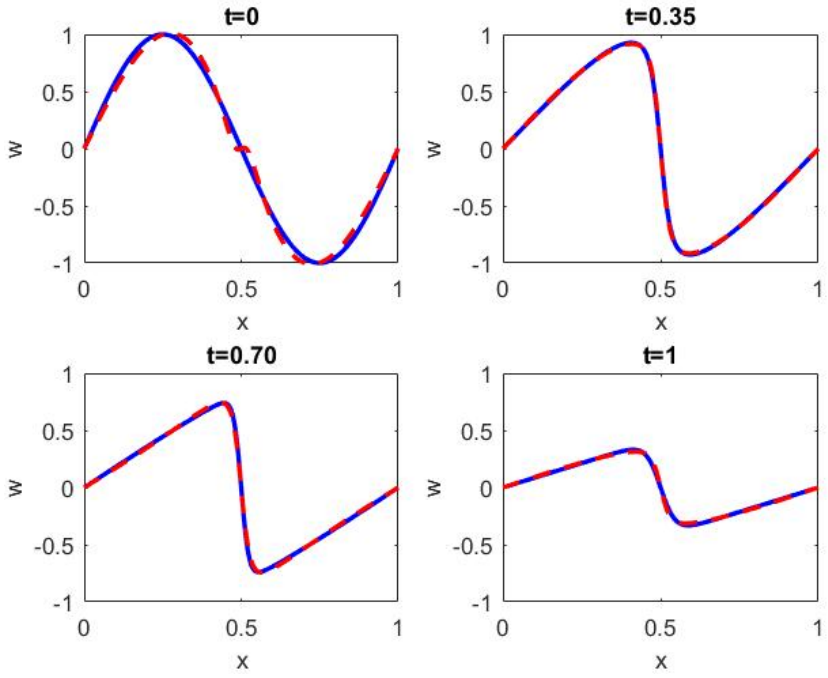

Figure 3.1: Full (solid) Vs Reduced (dashed) model with Re=100

Figures 3.1 and 3.2 compare the solution of the full and reduced order models. Solid is the full order, dashed is the reduced. POD modes were constructed from 50 snapshots and the number of spacial degrees of freedom is 200, i.e. the full order system size is 200. The reduced order size is two only. The low number of states needed to get this performance is driven by the fact that zero Dirichlet boundary conditions are used to generate the snapshots. We will see later that as input values change, more states will be needed to achieve the same performance.

Although the reconstructed solution looks to agree with the full order one, there is still a problem for highly nonlinear situations (high Re) where discontinuities might appear as shown in Figure 3.3 where both POD modes have a sharp change at $x = 0.5$ where shocks occur as shown earlier. As shown in (3.19), the spatial derivative of the POD modes is needed to design the system parameters in (3.19). Figure 3.4 shows how large these derivatives are around the shock location.

Now, for the same initial condition but using different controls, we use $u_a = t$ and $u_b = -t$ where t runs from 0 to 1, five states are needed to show the performance in Figure 3.5. Notice the multiple shocks that increase overtime.

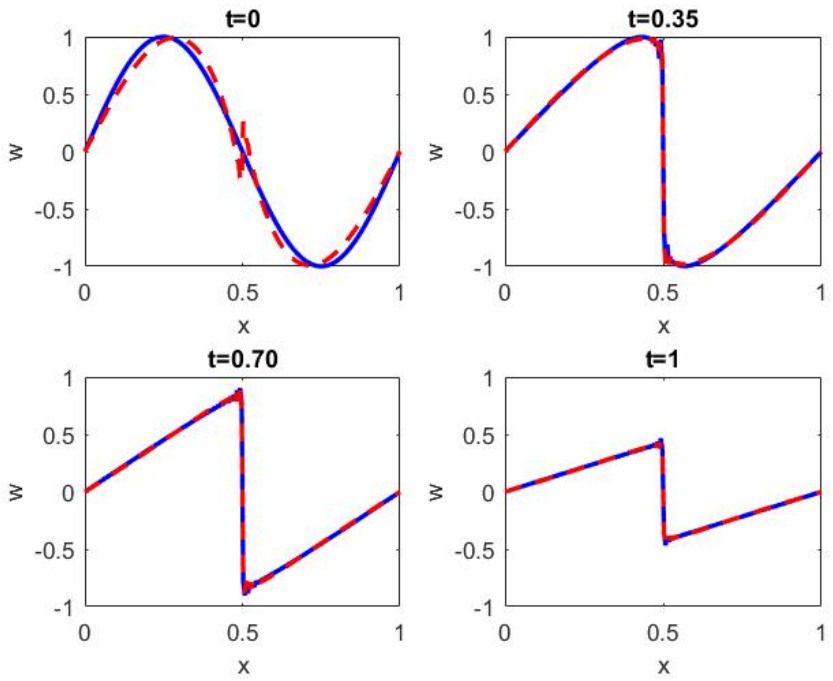

Figure 3.2: Full (solid) Vs Reduced (dashed) model with Re=5000

3.2 Solution to the Homogeneous Dirichlet Boundary Conditions System

For a zero input boundary conditions, the quadratic nonlinear system (3.19) can be written as:

$$\dot{\alpha} = A\alpha + diag(\alpha)M\alpha \tag{3.20}$$
$$\alpha(0) = \alpha_0.$$

where $A, M \in R^{r\times r}$ are time invariant matrices since they are functions of spacial POD modes as described in the previous section , $\alpha \in R^r$ is the temporal coefficients vector and $diag(\alpha) \in R^{r\times r}$ is a diagonal matrix in which α is its main diagonal.

We claim that the solution of (3.19) is given by:

$$\alpha(t) = Ae^{At}(I - diag(c)Me^{At})^{-1}c \tag{3.21}$$

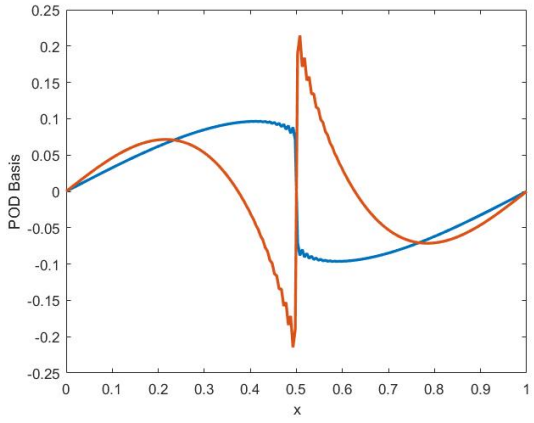

Figure 3.3: The two POD Basis functions for the highly nonlinear system

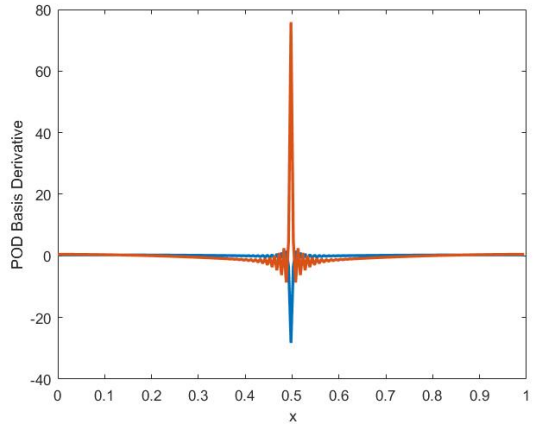

Figure 3.4: The spatial derivative of the two POD basis functions shown in Figure 3.3

where $c \in R^r$ is a constant vector that is a function of the initial condition α_0 and given by:

$$c = (I + diag(MA^{-1}\alpha_0))^{-1}A^{-1}\alpha_0 \tag{3.22}$$

and $diag(c), diag(MA^{-1}\alpha_0) \in R^{r\times r}$ are diagonal matrices in which c and $MA^{-1}\alpha_0$ are their main diagonals respectively. To proof our claim, we differentiate the expression (3.21) with respect to time, we get:

$$\dot{\alpha} = AAe^{At}(I - diag(c)Me^{At})^{-1}c+ \tag{3.23}$$

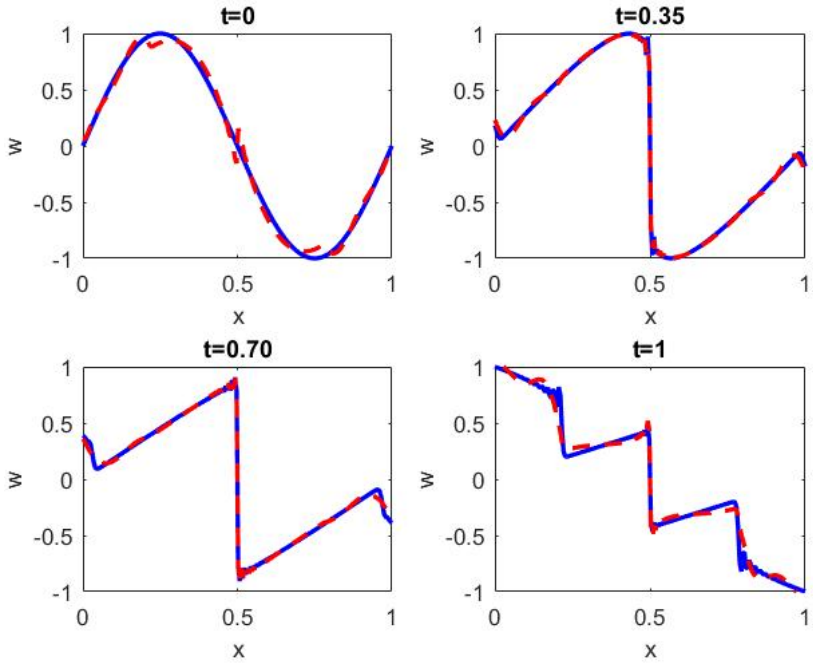

Figure 3.5: Full (solid) Vs Reduced (dashed) for nontrivial boundary controls, Re=5000 with 5 states model

$$Ae^{At}(I - diag(c)Me^{At})^{-1}diag(c)MAe^{At}(I - diag(c)Me^{At})^{-1}c$$

and using $\alpha = Ae^{At}(I - diag(c)Me^{At})^{-1}c$, equation (3.23) becomes:

$$\dot{\alpha} = A\alpha + Ae^{At}(I - diag(c)Me^{At})^{-1}diag(c)M\alpha \tag{3.24}$$

To show that $Ae^{At}(I - diag(c)Me^{At})^{-1}diag(c) = diag(\alpha)$, let

$$Ae^{At}(I - diag(c)Me^{At})^{-1}diag(c) := P \tag{3.25}$$

where $P \in R^{r\times r}$,then we have:

$$Ae^{At}(I - diag(c)Me^{At})^{-1} = Pdiag(c)^{-1} \tag{3.26}$$

Then we multiply c to the right of both sides we get:

$$\begin{aligned} \alpha &= Pdiag(c)^{-1}c \\ &= P1_r \end{aligned} \tag{3.27}$$

where $1_r \in R^r$ is the unity vector of length r, i.e all elements in 1_r are ones.
It is clear that the only P that satisfies (3.27) is $P = diag(\alpha)$. Then (3.23) becomes:

$$\dot{\alpha} = A\alpha + diag(\alpha)M\alpha$$

Finally we need to show that the initial condition is satisfied, we show that the choice of the constant c given by (3.22) satisfies the initial condition in (3.20) as follows:

$$\begin{aligned} c &= (I + diag(MA^{-1}\alpha_0)^{-1}A^{-1}\alpha_0 \\ (I + diag(MA^{-1}\alpha_0))c &= A^{-1}\alpha_0 \\ c + diag(MA^{-1}\alpha_0)c &= A^{-1}\alpha_0 \\ c + diag(c)MA^{-1}\alpha_0 &= A^{-1}\alpha_0 \\ c &= (I - diag(c)M)A^{-1}\alpha_0 \\ A(I - diag(c)M)^{-1}c &= \alpha_0 \end{aligned} \tag{3.28}$$

which equals the initial condition $\alpha(0)$ in (3.20).

3.3 Nonlinear Control

In most applications, the control objective for such systems is to track a particular trajectory, so we consider the minimization of the cost function:

$$J(u) = \frac{1}{2}\int_0^{t_f} [(\alpha - \alpha_r)^T Q(\alpha - \alpha_r) + u^T Ru]dt \tag{3.29}$$

subject to the constraints:

$$\dot{\alpha} = A\alpha + N(\alpha) + Bu + B'u^2$$
$$\alpha(0) = \alpha_0.$$

where α_r is the reference states vector that the system is supposed to track, Q is a diagonal, symmetric and positive semidefinite matrix of state weights, R is a diagonal, symmetric and positive-definite matrix of control weights. The optimization problem (3.29) is considered over all controls $u \in L_2(0, \infty)$.

The Hamiltonian is defined as:

$$H = \frac{1}{2}(\alpha - \alpha_r)^T Q(\alpha - \alpha_r) + \frac{1}{2}u^T Ru + \lambda^T(A\alpha + N(\alpha) + Bu + B'u^2) \tag{3.30}$$

where λ is the adjoint variables vector. Derivative of H w.r.t the control u is zero at the critical control values, so the optimality equation becomes:

$$\frac{\partial H}{\partial u} = Ru + B^T\lambda + 2(B'^T\lambda \circ u) = 0 \tag{3.31}$$

where $\circ$ denotes the Hadamard product (term by term multiplication). Since R is diagonal then it is easy to factorize it as:

$$Ru = diag(R) \circ u \tag{3.32}$$

where $diag(R)$ is the diagonal vector of R. The optimal control can be found:

$$u_{opt} = \frac{-B^T\lambda}{diag(R) + 2B'^T\lambda} \tag{3.33}$$

Note that the division in (3.33) is computed term by term between the numerator and denominator vectors. It is the inverse operation of the Hadamard product.

The adjoint equation is:

$$\dot{\lambda} = -\frac{\partial H}{\partial \alpha} = -Q(\alpha - \alpha_r) - A^T\lambda + \frac{d\lambda^T N(\alpha)}{d\alpha} \qquad (3.34)$$
$$\lambda(t_f) = 0.$$

$\frac{d\lambda^T N(\alpha)}{d\alpha}$ is found by differentiating the expression in (3.16). It is convenient to express the integral over the domain Ω as a sum (which is how it is actually coded in Matlab), so:

$$\frac{d\lambda^T N(\alpha)}{d\alpha} = 2\Phi^T(\frac{d\Phi}{dx} \circ \Phi\alpha) \qquad (3.35)$$

where Φ is the matrix that contain all POD basis vectors. Finally the coupled states and adjoint systems (3.19) and (3.34) are solved simultaneously.

The state system has initial conditions while the adjoint has final conditions. One method to solve such coupled systems is the forward backward sweep method explained in [40] and [5]. The steps of the forward backward sweep algorithm is as follows:

1. Start with an initial guess for the control u_{opt} over the domain.
2. Using the state system initial conditions and the values for u_{opt} , solve for α forward in time.
3. Using the adjoint final conditions and the values for u_{opt} and α, solve λ backward in time.
4. Update u_{opt} by entering the new α and λ into the expression of the optimal control.
5. Check convergence. Stop if the difference is negligible between this iteration and the previous one, otherwise return to step 2.

Convergence and stability of this algorithm is discussed in [23].

Figure 3.6 shows a comparison between a full order controlled system and a 3 states reduced system with $Re = 100$.

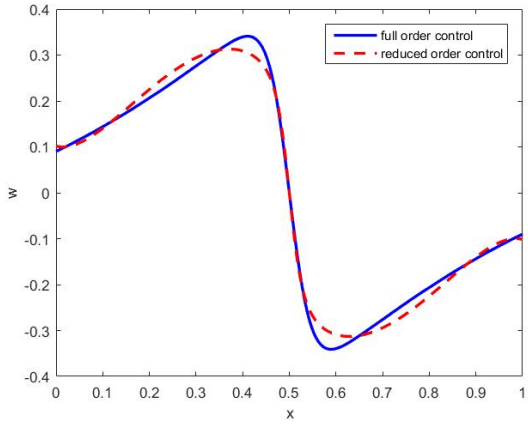

Figure 3.6: Full Vs 3 states reduced order nonlinear control

While linearized controllers might work just fine with low Re, they definitely fail when Re is large when the nonlinearity dominates the system behavior. To compare our nonlinear controller to the linear one, a high Re is used with the same number of reduced order system (5 states) and the same tracking function which is an arbitrary solution obtained with symmetric sinusoidal boundary conditions and a sin wave initial condition as usual. Figure 3.7 and 3.8 show how the linear control fails to track the reference function as well as the nonlinear one. Reference trajectories are the solid blues and controlled system trajectories are the dashed reds.

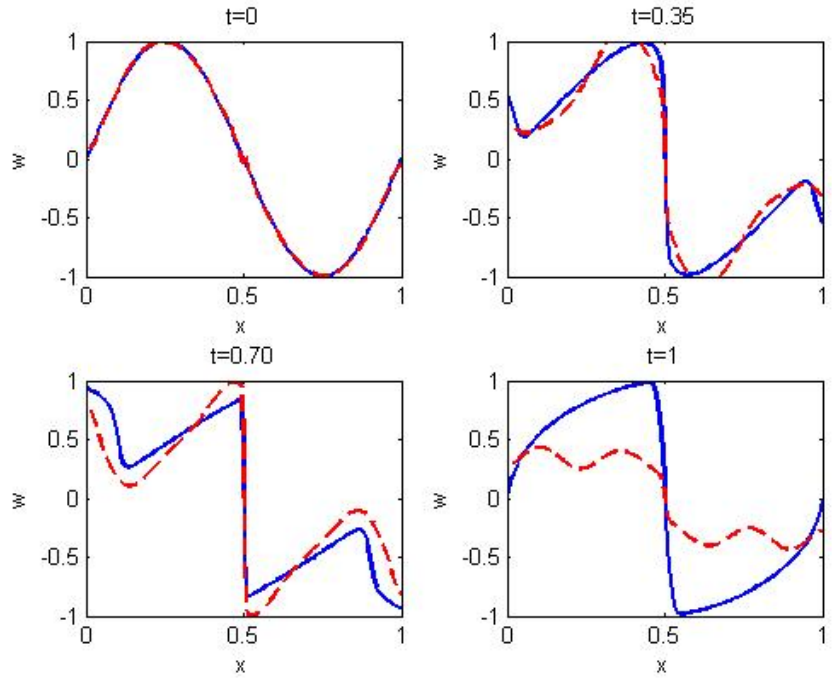

Figure 3.7: Linear control, full (solid) Vs reduced (dashed)

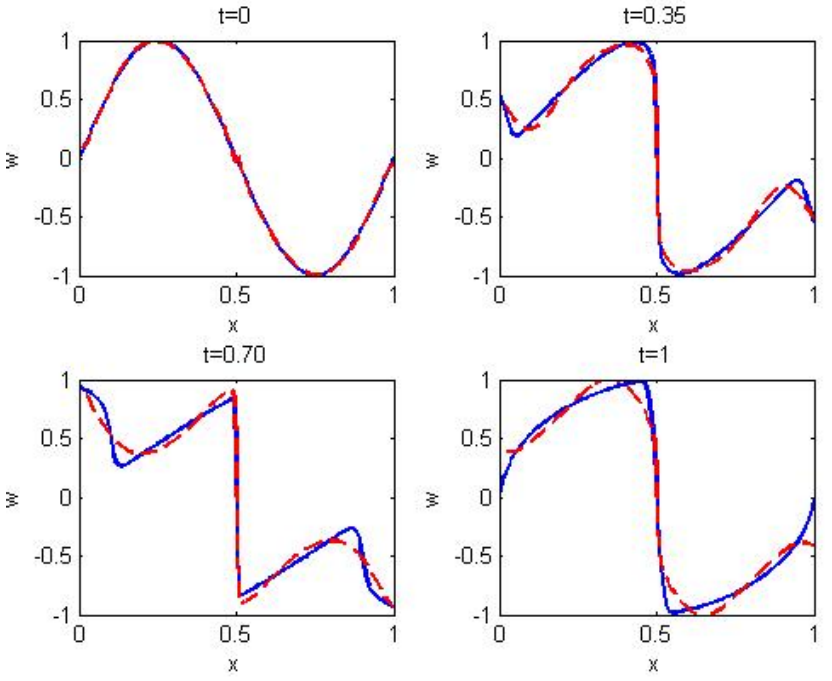

Figure 3.8: Nonlinear control, full (solid) Vs reduced (dashed)

Chapter 4

Flow Separation Control for the NACA 0015 Airfoil Based on an OLLP Reduced Order Model

In this chapter, complete and detailed approach for the Orthogonal Locality Preserving Projections (OLPP) modes computation for the incompressible Navier Stokes PDE that governs the dynamics of the NACA 0015 airfoil fluid flow problem is presented. Close snapshots in the full order model are forced to stay close in the reduced order model by defining an optimization problem that preserves local distances. The POD reduced model is computed for the same problem. Optimal control to track a defined trajectory is designed. The closed loop flow separation control problem is solved in which fluid suction on part of the airfoil boundary is used to control flow separation on the boundary layer.

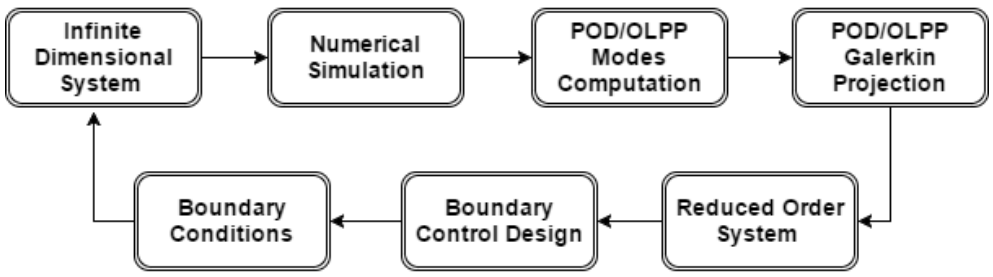

Figure 4.1: Model Reduction and Boundary Control Process Diagram

Locality Preserving Projections are linear projective maps that arise by solving a variational problem that optimally preserves the neighborhood structure of the data set. The authors in [48] applied a locality preserving algorithm in the image processing field to reduce dimensionality. The algorithm builds a graph incorporating neighborhood information of the data set. This linear transformation then optimally preserves local neighborhood information in a certain sense. In other words OLPP guarantees that close neighbors in the full order model will stay close in the reduce order model. Although POD beats OLPP in a global sense, the latter preserves the local behavior that POD misses.

Flow control is the process of bringing on desired changes in the behavior of the flow. A laminar flow of fluid moving in a deterministic way, is associated with considerable less drag, or friction, at the boundary layer, than a turbulent flow, which is characterized by velocity components that appear to be stochastic in nature. Laminar flows are unstable, and will unless controlled, become turbulent flows. Laminar flows are easier to control before it is too late when the transition to turbulence happens. Control objectives include separation prevention, transition delay, drag reduction, lift enhancement, and noise suppression [20].

Flow control can be passive or active. Passive control requires no auxiliary power and no control loop and can be implemented by choosing values for several surface parameters that can influence the boundary layer flow such as shape, roughness, porosity, and curvature [19]. Active control requires a control loop which can be open or closed. Control techniques either modifies the shape of the instantaneous mean velocity profile or selectively influences the small dissipative eddies [20].

Prandlt in [52] introduced the boundary layer theory and explained the physics of the separation phenomena. Laminar flow control and polymer drag reduction techniques were notable achievements during the world war II era, partially summarized in [37] and [75]. Control methods such as using large eddy breakup devices and riblets to reduce skin friction drag in turbulent boundary layers were developed in the 70's and 80's [27] [9] [4]. Reactive control strategies have been developed beyond the 90's by the help of the development of micro electromechanical systems (MEMS) and neural networks [77] [44] [18].

Suction and injection of primary fluid can have significant effects on the flow field. In suction, favorable pressure gradient or lower wall viscosity results in vorticity flux away

from the wall, making the surface a source of spanwise and streamwise vorticity. The corresponding velocity profiles have negative curvature at the wall and are more resistant to separation but associated with higher skin friction drag. Injection is the opposite; adverse pressure gradient or higher wall viscosity makes the velocity profile faster to separate but associated with lower skin friction [2], [12], [76].

Full model reduction and boundary control process for the flow separation control problem is shown in Fig 4.1. This chapter is basically going through this process block by block as follows; In section 6.2, the fluid flow system is described and a numerical solution for the problem is found. In section 6.3, the POD basis functions are computed. In section 6.4, the OLPP algorithm is presented and flow separation control is shown in section 6.5.

4.1 Problem Description

We consider the 2D incompressible fluid flow over the NACA 0015 airfoil shown in Figure 4.4.

The PDE that models the fluid velocity and pressure behavior is the two dimensional Navier Stokes Equation, given by the following dimensionless equations:

$$\begin{aligned} \frac{\partial w}{\partial t} &= \frac{1}{Re}\left(\frac{\partial^2 w}{\partial x^2}+\frac{\partial^2 w}{\partial y^2}\right) - w\frac{\partial w}{\partial x} - v\frac{\partial w}{\partial y} - \frac{\partial p}{\partial x} \\ \frac{\partial v}{\partial t} &= \frac{1}{Re}\left(\frac{\partial^2 v}{\partial x^2}+\frac{\partial^2 v}{\partial y^2}\right) - w\frac{\partial v}{\partial x} - v\frac{\partial w}{\partial y} - \frac{\partial p}{\partial y} \end{aligned} \tag{4.1}$$

$$\frac{\partial w}{\partial x} + \frac{\partial v}{\partial y} = 0 \tag{4.2}$$

where x and y are the spatial coordinates in the 2D domain Ω and $t \in [t_0, t_f]$ is the time variable, w, v are the velocity components in x,y directions, p is the pressure and Re is the Reynolds number. Equations (4.1) are the momentum equations while (4.2) is the continuity

equation. Initial conditions are given by:

$$\begin{aligned} w(\Omega, t_0) &= w_0 \\ v(\Omega, t_0) &= v_0 \\ p(\Omega, t_0) &= p_0 \end{aligned} \tag{4.3}$$

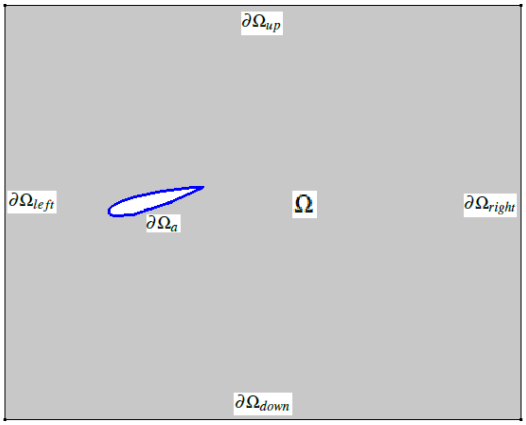

Figure 4.2: Domain and Boundaries

Let $\partial\Omega$ denotes the boundary of the domain Ω such that $\partial\Omega = \partial\Omega_a \cup \partial\Omega_{left} \cup \partial\Omega_{right} \cup \partial\Omega_{up} \cup \partial\Omega_{down}$ as shown in Fig (4.2) where $\partial\Omega_a$ is the airfoil boundary where the control input is applied, $\partial\Omega_{left}$ is the rectangle left boundary where the inflow condition for velocity is specified, $\partial\Omega_{right}$ is the rectangle right boundary where the outflow condition for velocity is specified, $\partial\Omega_{up}$ and $\partial\Omega_{down}$ are the rectangle upper and lower boundaries where periodic flow condition is defined. Boundary conditions are summarized as:

$$
\begin{aligned}
w(\partial\Omega_a, t) &= & u_w(\partial\Omega_a, t) & \quad w \text{ Dirichlet control input,} \\
v(\partial\Omega_a, t) &= & u_v(\partial\Omega_a, t) & \quad v \text{ Dirichlet control input,} \\
w(\partial\Omega_{up}, t) &= & w(\partial\Omega_{down}, t) & \quad w \text{ periodic flow conditions,} \\
v(\partial\Omega_{up}, t) &= & v(\partial\Omega_{down}, t) & \quad v \text{ periodic flow conditions,} \\
p(\partial\Omega_{up}, t) &= & p(\partial\Omega_{down}, t) & \quad p \text{ periodic flow conditions} \\
w(\partial\Omega_{left}, t) &= & w_{left} & \quad w \text{ inflow condition,} \\
v(\partial\Omega_{left}, t) &= & v_{left} & \quad v \text{ Inflow condition,} \\
p(\partial\Omega_{right}, t) &= & 0 & \quad p \text{ Outflow condition.}
\end{aligned}
$$

Numerical simulation is performed for $R_e = 10,000$ and 2226 finite element mesh nodes for 10 seconds with time step 0.1 seconds Using Comsol Multiphysics software. As shown in Fig 4.3, mesh is finer around the boundary of the airfoil where faster dynamics is expected. Figure 4.4 shows the full order model simulation for the velocity magnitude ($\sqrt{w^2 + v^2}$) at $t = 10$ with open loop zero inputs at the airfoil boundary.

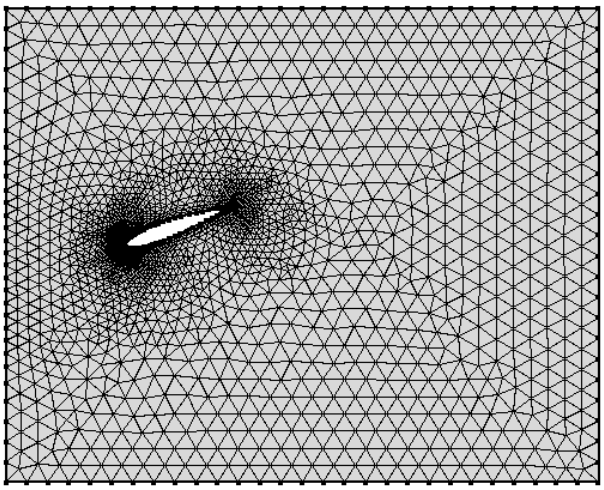

Figure 4.3: Problem geometry and mesh

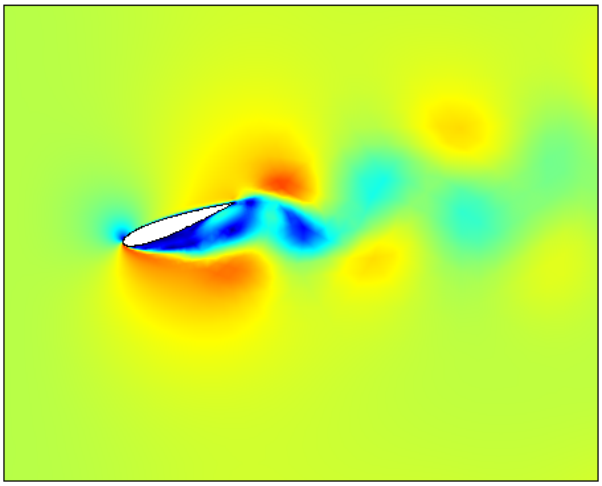

Figure 4.4: Full order solution at $t = 10$, velocity magnitude

4.2 POD Basis Computation

Let $\begin{pmatrix} w(x,y,t) \\ v(x,y,t) \end{pmatrix}$ be the fluid velocity solution to (4.1) and (4.2) such that:

$$\begin{pmatrix} w(x,y,t) \\ v(x,y,t) \end{pmatrix} = \begin{pmatrix} \bar{w}(x,y,t) \\ \bar{v}(x,y,t) \end{pmatrix} + \begin{pmatrix} \hat{w}(x,y,t) \\ \hat{v}(x,y,t) \end{pmatrix} \tag{4.4}$$

where $\bar{w}(x,y,t)$, $\bar{v}(x,y,t)$ are the mean velocity components and $\hat{w}(x,y,t)$, $\hat{v}(x,y,t)$ are the turbulent fluctuating velocity components. The turbulent velocity field is approximated by a linear combination of the POD basis functions as:

$$\begin{pmatrix} \hat{w}(x,y,t) \\ \hat{v}(x,y,t) \end{pmatrix} = \sum_{i=1}^{N} \alpha_i(t) \begin{pmatrix} \phi_i^w(x,y) \\ \phi_i^v(x,y) \end{pmatrix} \tag{4.5}$$

As shown in [26], the process is to maximize the averaged projection of the velocity field onto the basis functions $\|\phi^w\|$ and $\|\phi^v\|$ that are normalized. In other words, the optimization problem as explained in [26] is to find ϕ^w, $\phi^v \in L_2(\Omega)$ such that:

$$\langle \begin{pmatrix} \hat{w} & \phi^w \\ \hat{v} & \phi^v \end{pmatrix}^2 \rangle, \quad \|\phi^w\| = \|\phi^v\| = 1 \tag{4.6}$$

is maximized where $\langle\cdot\rangle$ denotes an averaging operation, $\|.\|$ is the L_2 norm, and $(,)$ is the inner product in $L_2(\Omega)$ for vector valued functions given by:

$$(\mathbf{f},\mathbf{g}) = \int_{\Omega} \mathbf{f}^T\mathbf{g}\, dA \tag{4.7}$$

The solution of this maximization problem is given by the eigenfunctions ϕ^w and ϕ^v that correspond to the largest eigenvalues of the following eigenvalue problems:

$$\int_{\Omega} \langle w(x,y)w(\acute{x},\acute{y})\rangle \phi^w((\acute{x},\acute{y}))d\Omega = \lambda^w\phi^w(x,y) \tag{4.8}$$

$$\int_{\Omega} \langle v(x,y)v(\acute{x},\acute{y})\rangle \phi^v((\acute{x},\acute{y}))d\Omega = \lambda^v\phi^v(x,y) \tag{4.9}$$

The ensemble of solution snapshots is available and the equivalent discrete optimization problem is simply the eigenvectors of the sample covariance matrix. 6 POD modes and their energy preserving percentages for w and v are shown in figures 4.5 and 4.6. By projecting the first 6 optimal modes on the full order set we get the reduced order representation of w and v shown in Figures 4.9 and 4.10. Figures 4.7 and 4.8 show the full order w and v velocity components at $t = 10$. These 6 modes capture 94.2% of w and 93.6% of v energies.

4.3 Orthogonal Locality Preserving Projection

In general, POD is not optimal in the manifold metric minimization sense. We propose to use locality preserving concept as an alternative to the classical POD model reduction technique.

Let $\mathcal{M} = \mathcal{M}^d$ be a d- dimensional smooth and compact submanifold of the Euclidean space $\mathbb{R}^n$. Let $\{x_i\} \subset \mathcal{M}$ be a finite set of snapshots that lie on $\mathcal{M}$. The manifold metric between two distinct snapshots x_i and x_j is defined by:

$$d_{\mathcal{M}}(x_i,x_j) = \inf_{\gamma}\{\text{length}(\gamma)\} \tag{4.10}$$

where γ varies over a set of piecewise smooth arcs connecting x_i to x_j. It is clear that $d_{\mathcal{M}}(x_i, x_j)$ is different than the Euclidean distance $\|x_i - x_j\|$ in the higher dimensional space n. Conventional POD minimization problem is stated as follows:

$$\phi = \arg \min_{\|\phi\|=1} \sum_i \|x_i - (x_i, \phi)\phi\|_2^2 \tag{4.11}$$

If x_i and x_j are too close on the manifold then it is a valid approximation that $d_{\mathcal{M}}(x_i, x_j) \simeq \|x_i - x_j\|_2$. This means that close members in the original full order set must stay close in the reduced order set to preserve an approximate global manifold metric among other members in the set.

OLPP projects the data in a way that preserves a certain affinity graph $\mathcal{G} = (\mathcal{V}, \mathcal{E})$ where graph nodes $\mathcal{V}$ are the snapshots. The edges can be defined by taking some k number of nearest neighbor nodes to every state x_i. Another option to define the edges is to include all neighbors within a radius ϵ from x_i.

OLPP defines the projected points in the form $y_i = V^T x_i$ by putting a penalty for mapping the nearest neighbor nodes in the original graph to distant points in the projected data, so the objective is to minimize:

$$J(Y) = \frac{1}{2} \sum_{i,j=1}^{n} w_{ij} \|y_i - y_j\|_2^2 \tag{4.12}$$

subject to the orthogonality constraint $V^T V = I$ and the weights w_{ij} are defined by solving the following minimization problem:

$$J(W) = \sum_i \|x_i - \sum_j w_{ij} x_j\|_2^2 \tag{4.13}$$

with the constraints that $w_{ij} = 0$ if x_j is not a neighbor of x_i and $\sum_j w_{ij} = 1$, in other words, x_i is approximated by a convex combination of its neighbors. The solution, as shown in [48] is the eigenvalue problem:

$$X(D - W)X^T v_i = \lambda_i v_i \tag{4.14}$$

where W is the weights matrix and D is diagonal with $d_{ii} = \sum_{j=1}^{n} w_{ij}$.

Simulation results show close agreement between POD and OLPP as shown in Figures 4.9 and 4.10. To visualize the comparison better, one location on the domain is chosen and both velocity components with time are shown in Figures 4.11 and 4.12.

4.4 Galerkin Projection and Nonlinear Optimal Control

Using the approximated velocity expression in (4.5) to replace the velocity vector in the Navier stokes system (4.1) and applying a Galerkin projection on the POD/OLPP basis functions, the following finite dimensional system is obtained:

$$\begin{aligned} \dot{\alpha} &= A\alpha + N(\alpha) + Bu + B'u^2 \\ \alpha(0) &= \alpha_0. \end{aligned} \tag{4.15}$$

where

$$\begin{aligned} A_{ji} &= (\nabla\phi_j, \nabla\phi_i)_{L^2} \\ N_{jki} &= (\phi_j, (\phi_k.\nabla)\phi_i)_{L^2}, \end{aligned}$$

where (.) is the inner product defined in (4.7), B,B' are the boundary term matrices resulting from applying Green's identity in the Galerkin projection and u is vector of the discretized control input at the blue section in Fig 4.13 and u^2 is a vector of the squares of u.

The control objective to track a particular trajectory, so we consider the minimization of the cost function:

$$J(u) = \frac{1}{2}\int_0^{t_f} [(\alpha - \alpha_r)^T Q(\alpha - \alpha_r) + u^T Ru]dt \tag{4.16}$$

subject to the constraints:

$$\dot{\alpha} = A\alpha + N(\alpha) + Bu + B'u^2$$
$$\alpha(0) = \alpha_0.$$

where α_r is the reference states vector that the system is supposed to track, Q is a diagonal, symmetric and positive semidefinite matrix of state weights, R is a diagonal, symmetric and positive-definite matrix of control weights. The optimization problem (4.16) is considered over all controls $u \in L_2(0, \infty)$.

The Hamiltonian is defined as:

$$H = \frac{1}{2}(\alpha - \alpha_r)^T Q(\alpha - \alpha_r) + \frac{1}{2}u^T Ru + \lambda^T(A\alpha + N(\alpha) + Bu + B'u^2) \quad (4.17)$$

where λ is the adjoint variables vector. Derivative of H w.r.t the control u is zero at the critical control values, so the optimality equation becomes:

$$\frac{\partial H}{\partial u} = Ru + B^T\lambda + 2(B'^T\lambda \circ u) = 0 \quad (4.18)$$

where $\circ$ denotes the Hadamard product (term by term multiplication). Since R is diagonal then it is easy to factorize it as:

$$Ru = diag(R) \circ u \quad (4.19)$$

where $diag(R)$ is the diagonal vector of R. The optimal control can be found:

$$u_{opt} = \frac{-B^T\lambda}{diag(R) + 2B'^T\lambda} \quad (4.20)$$

Note that the division in (4.20) is computed term by term between the numerator and denominator vectors. It is the inverse operation of the Hadamard product.

The adjoint equation is:

$$\dot{\lambda} = -\frac{\partial H}{\partial \alpha} = -Q(\alpha - \alpha_r) - A^T\lambda + \frac{d\lambda^T N(\alpha)}{d\alpha} \qquad (4.21)$$
$$\lambda(t_f) = 0.$$

It is convenient to express the integral over the domain Ω as a sum (which is how it is actually coded in Matlab), so:

$$\frac{d\lambda^T N(\alpha)}{d\alpha} = 2\Phi^T(\frac{d\Phi}{dx} \circ \Phi\alpha) \qquad (4.22)$$

where Φ is the matrix that contain all POD/OLPP basis vectors. Finally the coupled states and adjoint systems (4.15) and (4.21) are solved simultaneously.

4.5 Flow Separation Control

Suction and injection of primary fluid can have significant effects on the flow separation phenomena. Flow separation occurs when the boundary layer travels far enough against an adverse pressure gradient that the speed of the boundary layer relative to the object falls almost to zero. The fluid flow becomes detached from the surface of the object, and instead takes the forms of eddies and vortices [2], [12], [76]. Fig 4.14 shows how the flow separation happens starting roughly at t=1 second and evolves to cause the vorticies shown at t=3 seconds. To control separation, fluid suction is actuated from the blue part of the boundary as shown in Fig 4.13. In suction, favorable pressure gradient or lower wall viscosity results in vorticity flux away from the wall, making the surface a source of spanwise and streamwise vorticity and the corresponding velocity profiles have negative curvature at the wall and are more resistant to separation but associated with higher skin friction drag. The effect is shown in Fig 4.15 where a PID controlled suction function is applied at the actuation location. Fluid injection on the other hand causes faster separation and stronger vorticity as shown in Fig 4.17. Fig 4.16 shows how the vorticity magnitude response with suction, injection and no control applied at the airfoil boundary.

To summarize this chapter, POD modes for the NACA 0015 airfoil fluid flow problem are computed, and since POD is not in general optimal in the manifold metric minimization sense, we forced close snapshots in the full order to stay close in the reduced order model by defining an optimization problem that preserves local distances of members. We showed how the flow separates on the boundary layer and how fluid suction controls the separation.

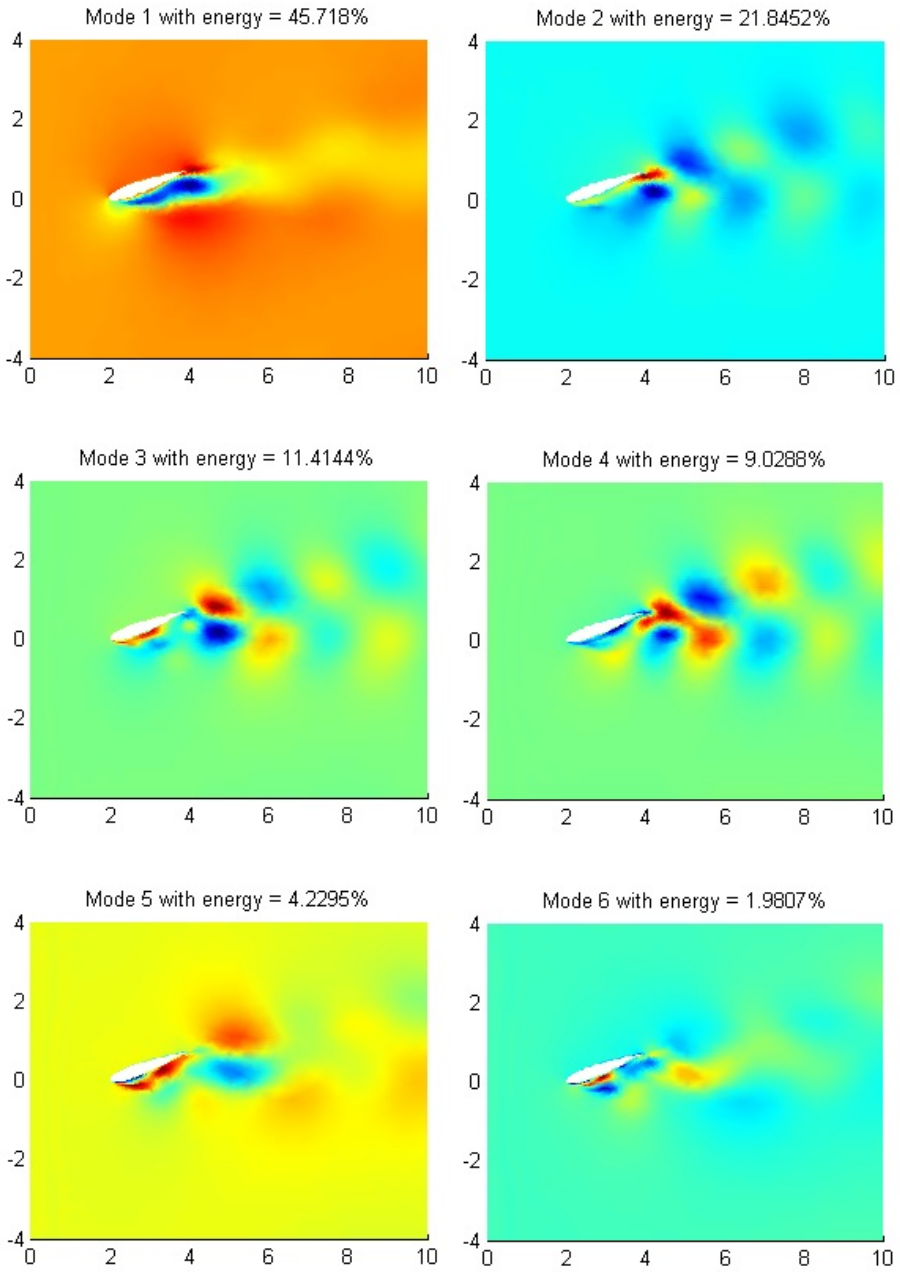

Figure 4.5: w POD modes

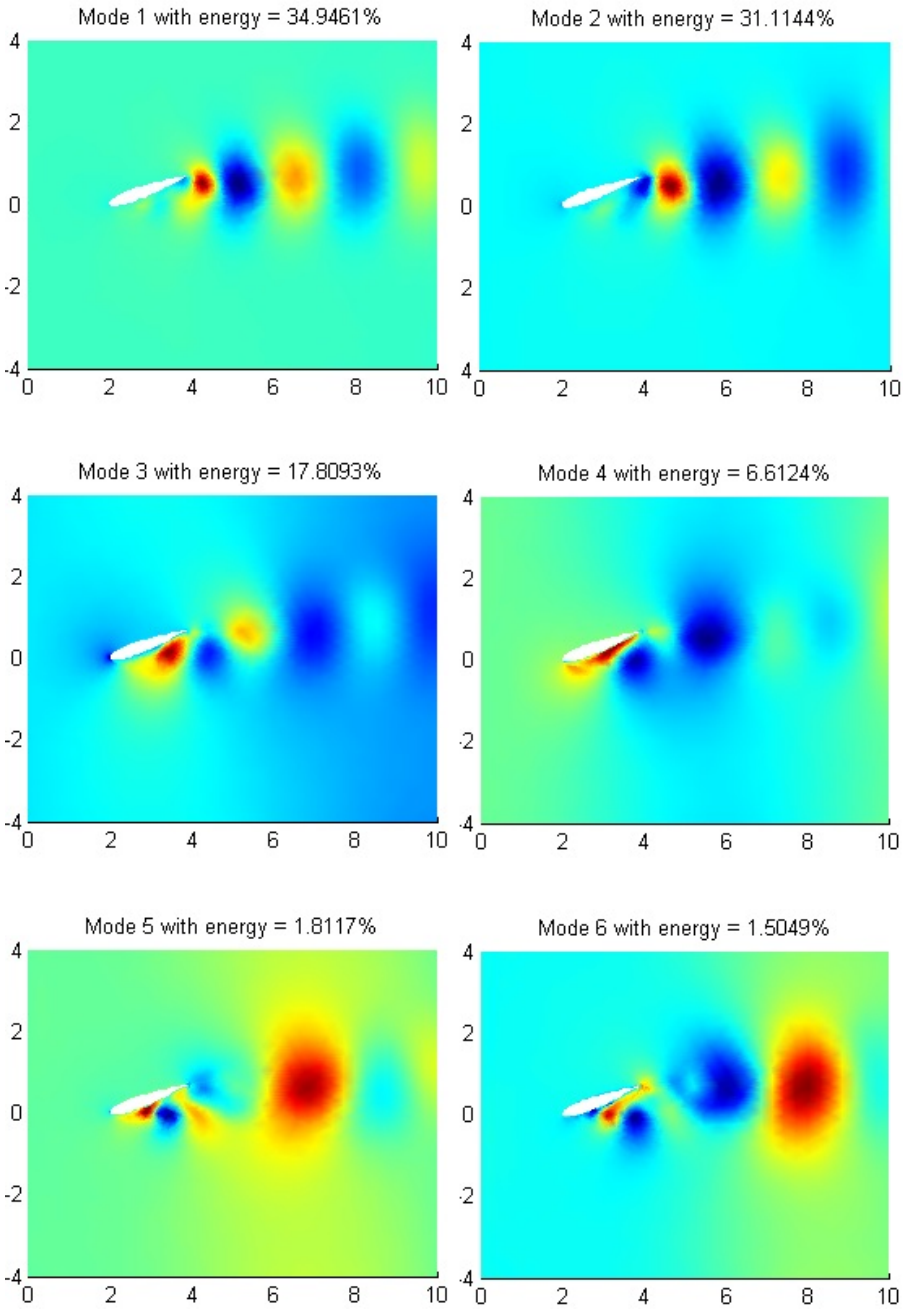

Figure 4.6: v POD modes

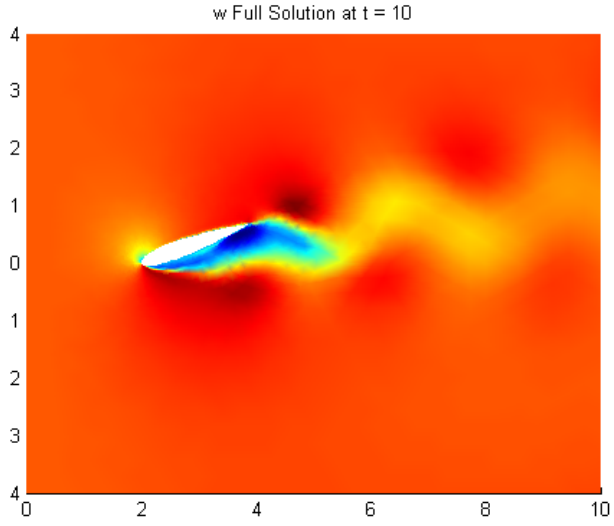

Figure 4.7: w full order

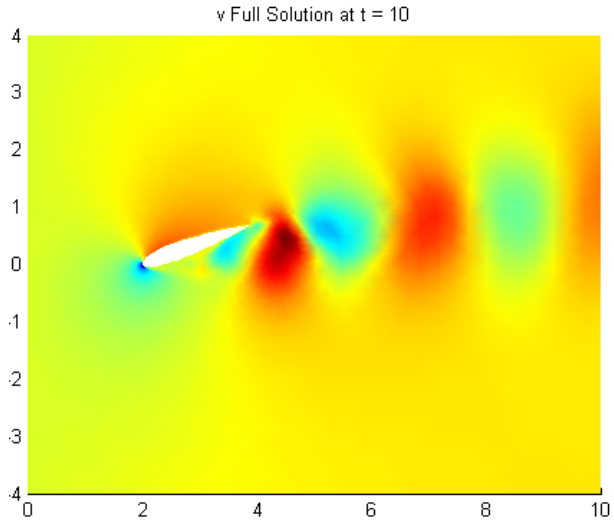

Figure 4.8: v full order

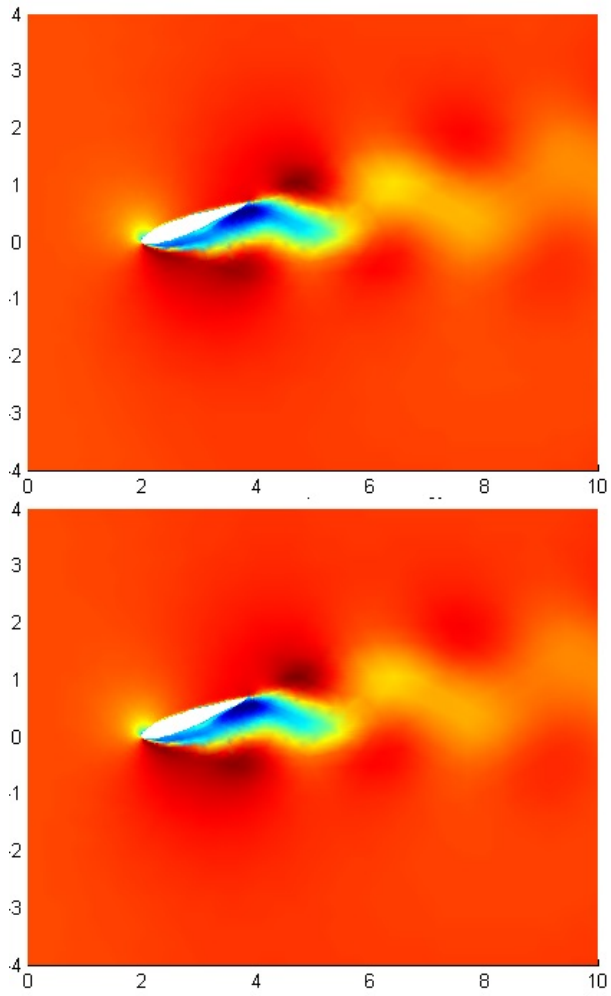

Figure 4.9: Reduced w component: POD (top) and OLPP (bottom)

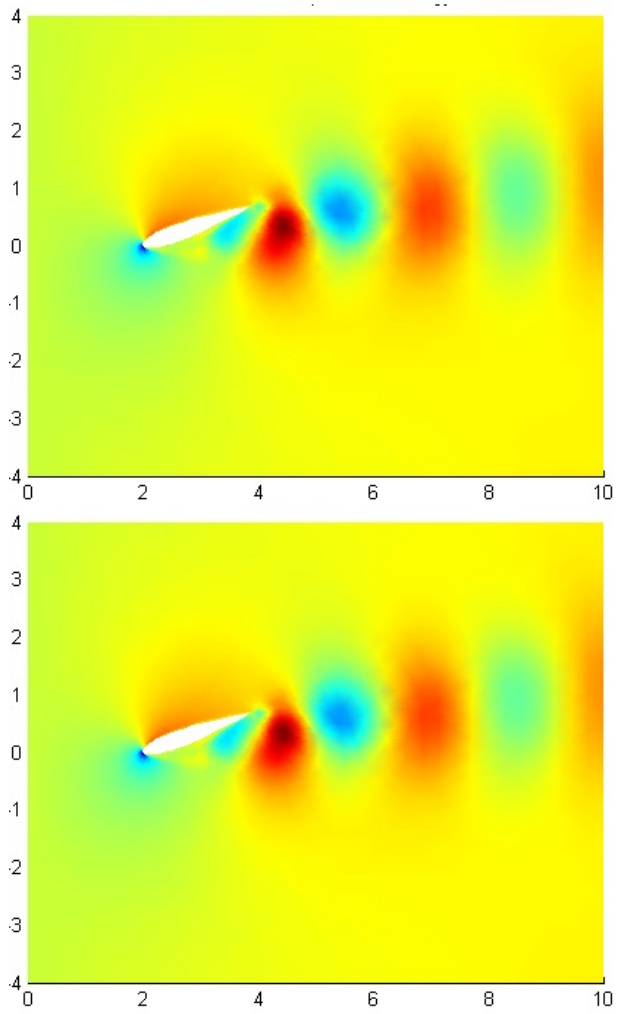

Figure 4.10: Reduced v component: POD (top) and OLPP (bottom)

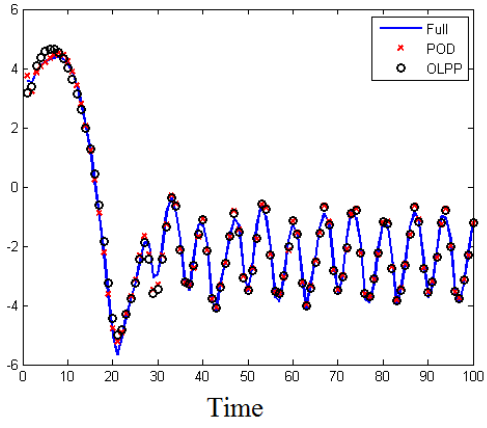

Figure 4.11: w velocity component at one location

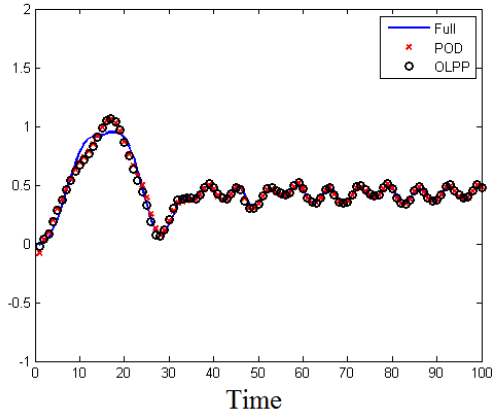

Figure 4.12: v velocity component at one location

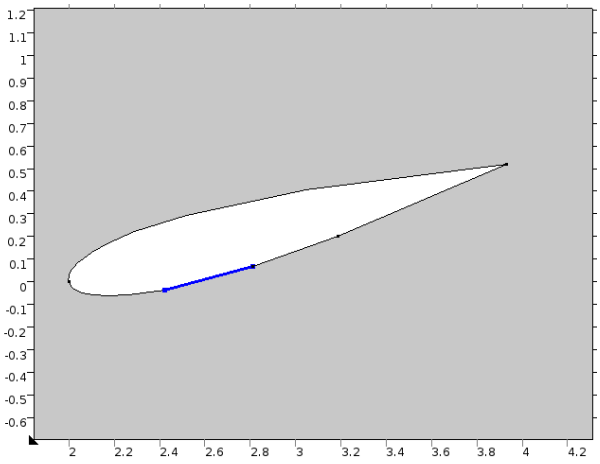

Figure 4.13: Control actuation location for the flow separation control problem

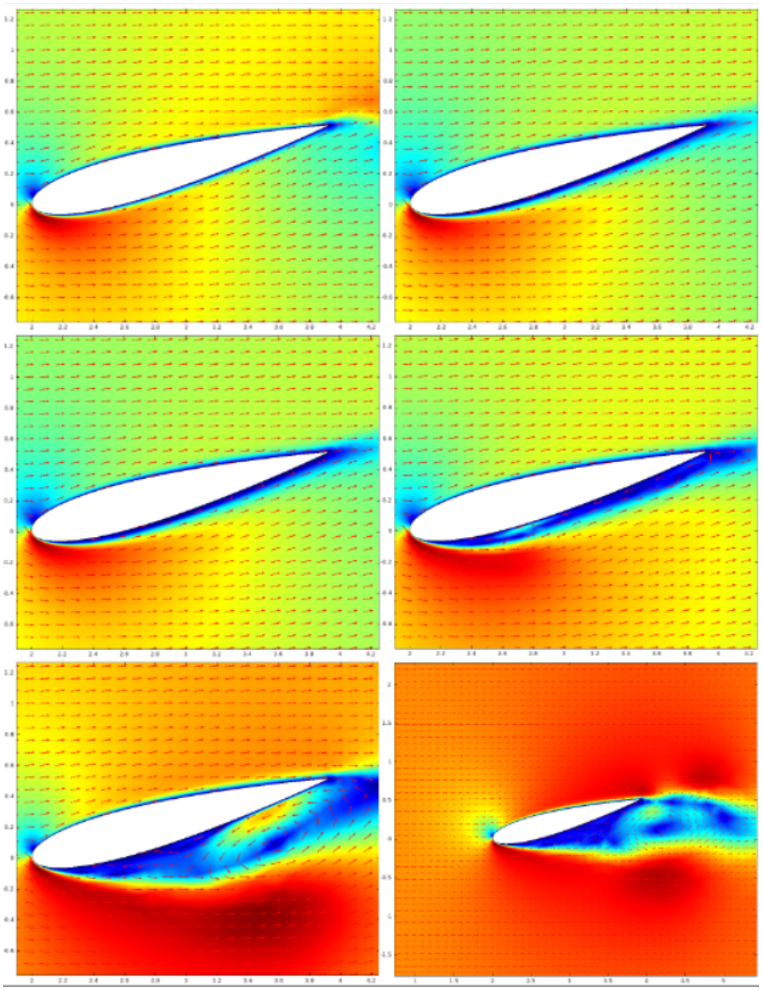

Figure 4.14: Flow separation with no control applied, snapshots at times t=0.1 (top left), 0.4, 0.6, 1, 2 and 3 seconds (bottom right)

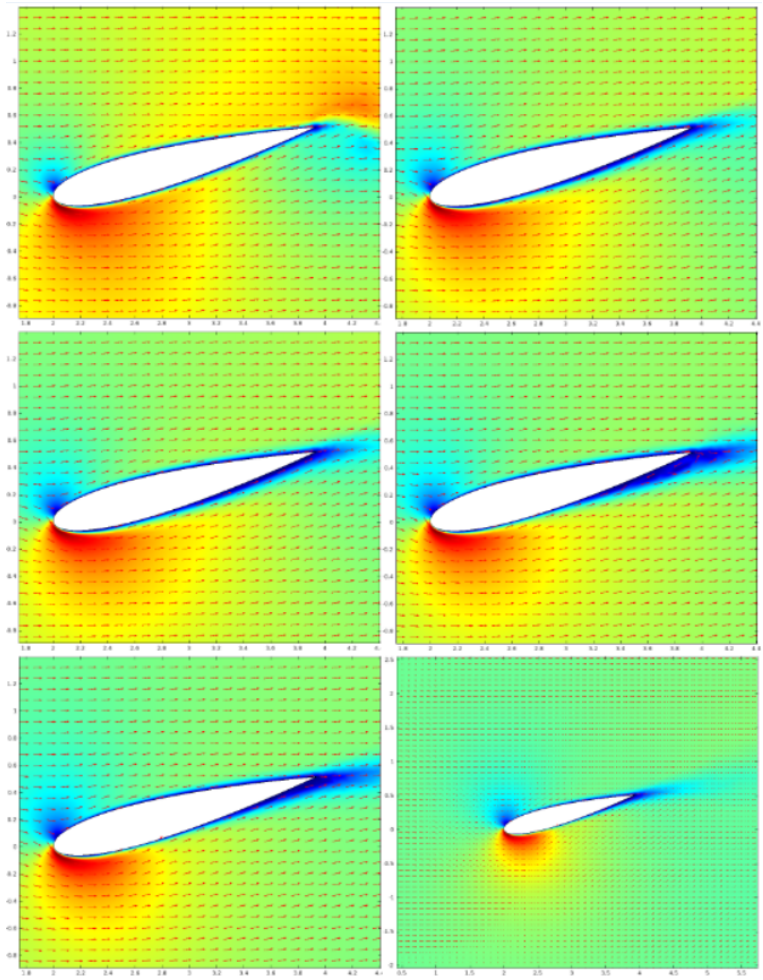

Figure 4.15: Flow separation controlled, snapshots at times t=0.1 (top left), 0.4, 0.6, 1, 2 and 3 seconds (bottom right)

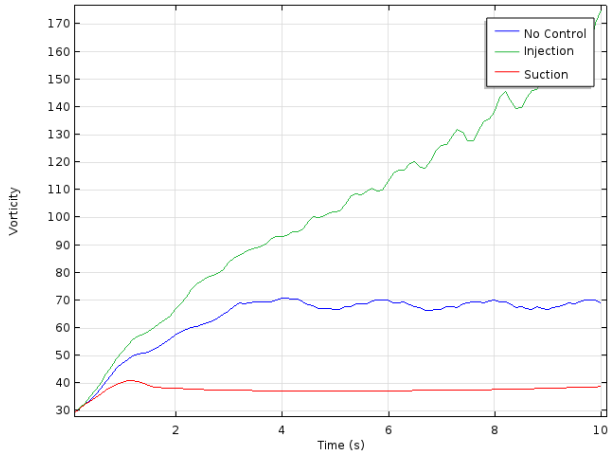

Figure 4.16: Vorticity with suction, injection and no control applied at the boundary

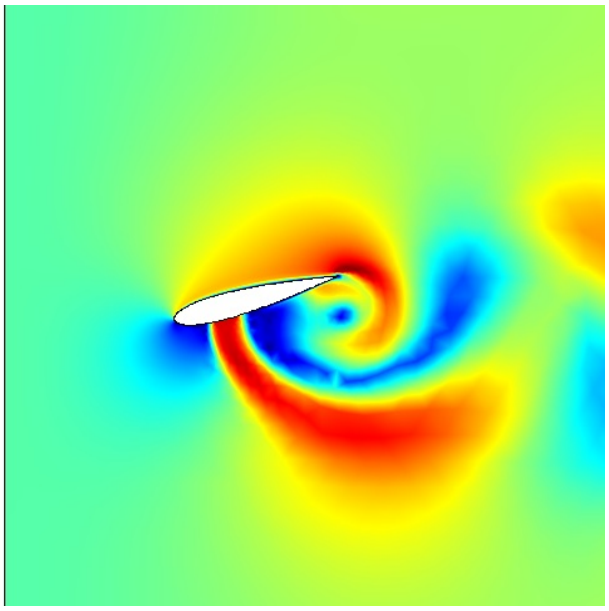

Figure 4.17: Effect of fluid injection on vorticity

Chapter 5

Model Reduction and Control of Temperature in Energy Efficient Buildings

Buildings are complex multi-scale, multi-physics, and highly uncertain dynamic systems with many sources of disturbances. Whole building simulation presents a formidable computational challenge making the development of design, optimization, and control tools of whole buildings difficult. At a fundamental level, there are several possible approaches to the design and control of high performance buildings. These include: (1) Simulation Based Design, (2) Holistic Fully Integrated Design, and (3) Hybrid Design Methods. Optimal design and control of these systems are very challenging problems and are often done by first developing a reduced order model on which the design is based [6]. This is known as a simulation based design.

In this chapter, distributed parameter theory is shown to provide useful information about building design and control. The problem illustrated by a single room shown in Figure 5.1 is considered. By solving the system numerically, the dynamical equations of the system with different parameters shed light on the best sensor location, temperature distribution of the room, and the corresponding energy consumption. Finite element theory is used to solve the PDE that describes the cooling and heating process.

The finite element technique is a numerical method for finding approximate solutions of partial differential equations (PDE). The Finite Element Method is a good choice for solving partial differential equations over complicated domains (like cars and oil pipelines), when the domain changes (as during a solid state reaction with a moving boundary), when the desired precision varies over the entire domain, or when the solution lacks smoothness [72].

The approach is based on simplifying the PDE into an approximating system of ordinary differential equations, which are then numerically integrated using standard techniques such as Euler's method, Runge-Kutta, etc. In solving PDEs, the main challenge is to create an equation that approximates the equation to be studied, but is numerically stable, such that errors in the input and intermediate calculations do not accumulate and make the resulting output to be meaningless. The finite element model comprises thousands (18182) states and therefore is not directly amenable to control design. This is due to the fact that the systematic design of optimal controllers based on the full order model results in the former having the same dimension, i.e., thousands of states. This is computational expensive and not feasible in real time. The order of the model needs to be first reduced and then a controller is designed based on the reduced model, and applied to the full order system to control the heat/cooling systems.

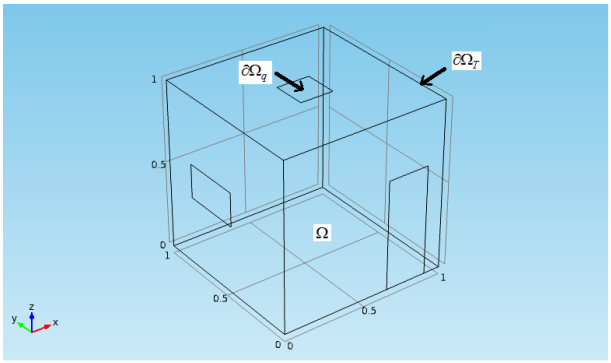

Figure 5.1: Room geometry

5.1 Finite Element Solution of the 3D Heat Equation Problem

The cooling and heat flow is modeled by a 3-dimensional (3D) heat equation [13]

$$\rho C_p \frac{\partial T(t,x,y,z)}{\partial t} + \nabla.(-k\nabla T(t,x,y,z)) = Q \tag{5.1}$$

where t denotes time, x, y, z are spatial coordinates assumed to belong to a domain Ω which represents the room geometry, ρ is the density in lb/ft^3, C_p is the specific heat capacity at constant pressure in $J/lb.F$, T is the absolute temperature in F, k is thermal conductivity in $w/ft.F$ and Q is the heat source in w/ft^3. The initial temperature is 50^oF. Boundary condition at the center of the top surface is a fixed temperature at 150^oF. The domain of the 3D heat equation Ω is the room geometry and,

- The initial conditions at $t = t_o$ is $T(x,y,z,t_o) = T_o(x,y,z)\, in\, \Omega$
- Dirichlet type boundary condition $T(x,y,z,t) = \hat{T}(x,y,z,t)\, in\, \partial\Omega_T$
- Neumann type boundary condition $q(x,y,z,t) = \hat{q}(x,y,z,t)\, in\, \partial\Omega_q$

where $q := -k\nabla T$ is the heat flux, $\partial\Omega_T$ and $\partial\Omega_q$ are Dirichlet and Neumann boundaries respectively as shown in Figure 5.1 where $\partial\Omega = \partial\Omega_T \cup \partial\Omega_q$. The 3D heat equation is multiplied by a basis function δT and integrated over the domain Ω as follows:

$$\int_\Omega \rho C_p \dot{T}\delta T + \int_\Omega \nabla \cdot (-k\nabla T)\, \delta T = 0 \tag{5.2}$$

The basis function δT has the following property

$$\delta T = 0\, in\, \partial\Omega_T \tag{5.3}$$

Using the divergence theorem:

$$\begin{aligned}\int_{\Omega} \nabla.(-k\nabla T)\delta T &= \int_{\Omega} \nabla(-k\nabla T\delta T) - \int_{\Omega} (-k\nabla T)\nabla\delta T \\ &= \int_{\partial\Omega} -k\nabla T\delta T n_i - \int_{\Omega} (-k\nabla T)\delta T \end{aligned} \tag{5.4}$$

Using the Neumann boundary condition and the basis function property 5.3 we have:

$$\begin{aligned}\int_{\partial\Omega} -k\nabla T n_i\delta T &= \int_{\partial\Omega_q} -k\nabla T n_i\delta T + \int_{\partial\Omega_T} -k\nabla T n_i\delta T \\ &= \hat{q}(x,t)\end{aligned} \tag{5.5}$$

Then the weak formulation of the problem follows

$$\int_{\Omega} \rho C_p\dot{T}\delta T - \int_{\Omega} q\nabla\delta T - \int_{\partial\Omega_q} \hat{q}\delta T = 0 \tag{5.6}$$

The spatial approximation of solution in the domain Ω is performed by a linear combination of shape functions , where $\phi_s = \phi_s(x)$, where

$$T(x,t) = \theta_s(t)\phi_s(x), s = 1, \cdots, N \tag{5.7}$$

where N is the total number of solution nodes and $\theta_s(t)$ is the time dependent coefficients. The basis function is also approximated as:

$$\delta T(x) = \theta_r(t)\phi_r(x) \tag{5.8}$$

Since the basis function is time independent, θ_r coefficients will only be numbers. Substitute in the weak form 5.6 and after some derivations; we get the system of ordinary differential equations (ODEs) as follows

$$M_{rs}\dot{\theta}_s = K_{rs}\theta_s + \int_{\partial\Omega} \hat{q}\phi_r \tag{5.9}$$

where $M_{rs} = \int_{\Omega} \rho\, C_p \phi_s \phi_p dxdydz$ is the thermal capacity matrix and $K_{rs} = \int_{\Omega} (-k\nabla\phi_s + \rho C_p u_i \phi_s)\nabla\phi_r dxdydz$ is the heat transfer matrix. The system in 5.9 can then be written in state space form as

$$\dot{x} = Ax + Bu \tag{5.10}$$

where $A := M_{rs}^{-1} K_{rs}$, $B := M_{rs}^{-1}$ and $x := \theta_s$ The plot of one snapshot of the 3D heat diffusion in the room using finite element analysis with the corresponding mesh is shown in Fig 5.2. One heating/cooling element is assumed to be installed in the room ceiling. Finite element solution at different times is shown in figures 5.3, 5.4, 5.5 and 5.6.

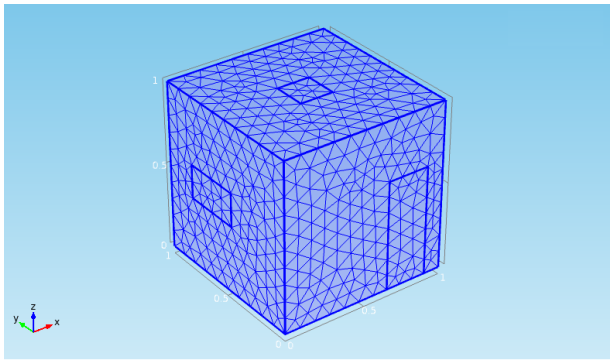

Figure 5.2: The 3D heat equation with corresponding finite element mesh. Number of mesh nodes = number of states = 18182 nodes.

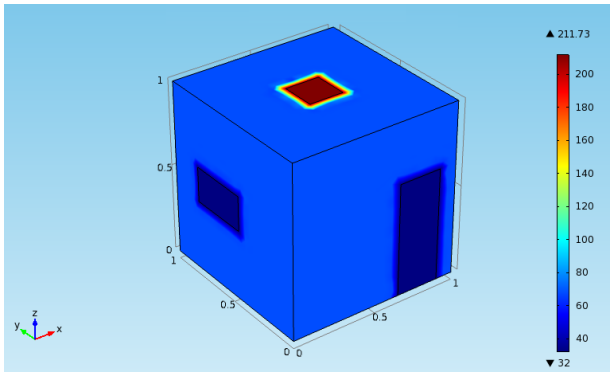

Figure 5.3: Temperature distribution in F after 1 minute

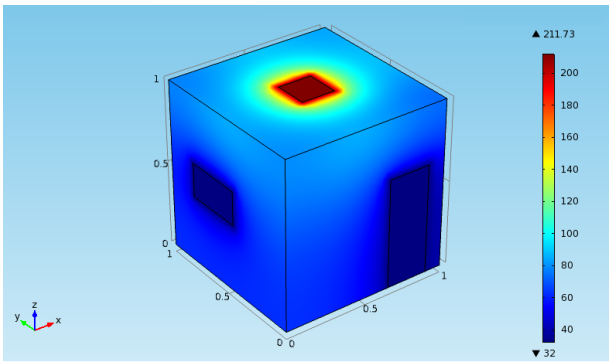

Figure 5.4: Temperature distribution in F after 20 minutes

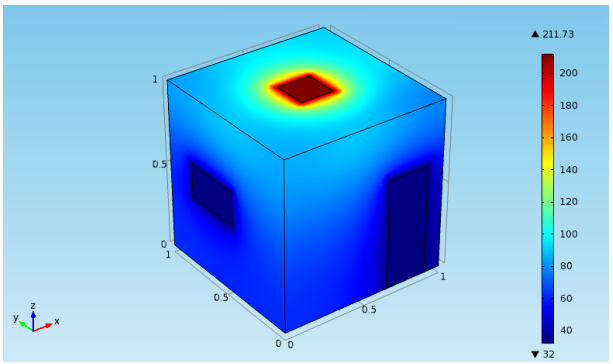

Figure 5.5: Temperature distribution in F after 40 minutes

5.2 Temperature Control

A linear quadratic regulator (LQR) controller [36] is designed to keep the room temperature at the desired value. The control design is based on the reduced order model and applied to the full order system of the form

$$\dot{x} = Ax + Bu$$

where x is the states vector that contains 18182 temperature values at the nodes shown in the mesh figure. The sensor location is chosen at $(04, 0, 0.5)$, so the measurement equation has the following form:

$$y = Cx$$

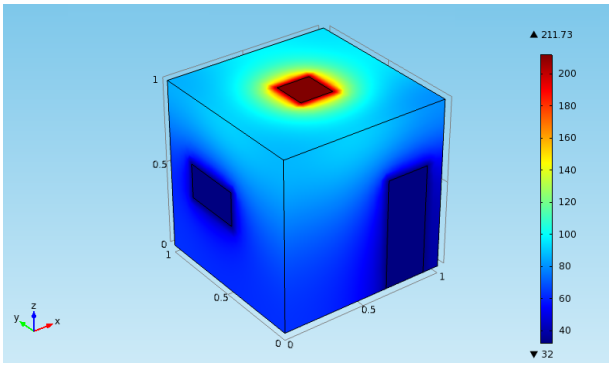

Figure 5.6: Temperature distribution in F after 60 minutes

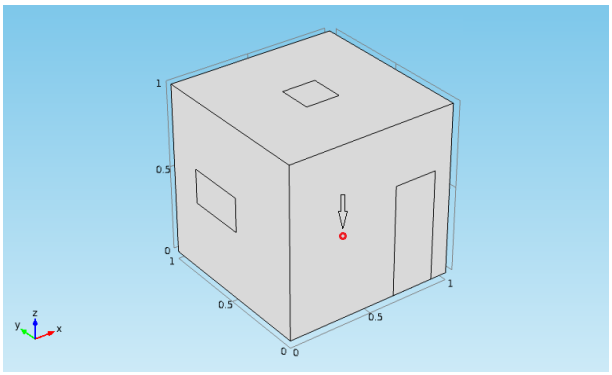

Figure 5.7: Sensor Location

where $C = [00 \cdots 1 \cdots 00]$ is a vector of zeros everywhere except for the sensor location node where the value is 1. Note that we assumed the temperature is measured by only one sensor.

One of the main issues arising in automatic control of room temperature is the best location of sensors in order to effectively estimate the temperature, especially in the context of using distributed parameter models. From a general point of view, the problem of optimal sensor location can be viewed as the problem of maximizing the output generated by a given state [21], [8]. In room temperature control it is no possible to sense inside the flow domain and full state estimation is not practical. For such problems, the sensors must be located on the boundary, in our case, somewhere on the room walls. In this work we rely on a search over the domain boundary $\partial\Omega$ for candidate locations to determine the best sensor position. In our simulation the best sensor location is represented in Figure 5.7.

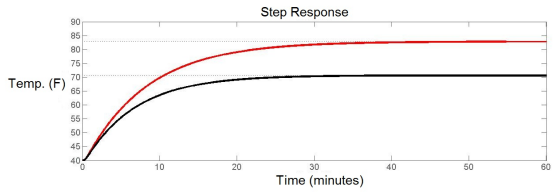

Figure 5.8: Step response for 2 desired set points 70 and 83

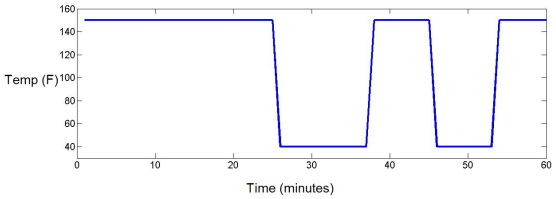

Figure 5.9: Control input

LQR controller is used as follows: the state-feedback law $u--Kx$ minimizes the quadratic cost function:

$$J(u) = \int (x^T Q x + u^T R u) dt \tag{5.11}$$

Subject to the system dynamics $\dot{x} = Ax + Bu$.

Figure 5.8 shows the step response for two different desired values of $70^o F$ and $83^o F$.

Note that the closed-loop response is stable and tracks the set points. The corresponding control input is plotted in the Figure 5.9. A constraint for the input signal to be bounded between $40^o F$ and $150^o F$ is added to account for heating/cooling systems saturation.

5.3 Reduced Order Model Using POD

With N snapshots in hand the $N \times N$ correlation matrix L is defined by:

$$L_{i,j} = \langle S_i, S_j \rangle \tag{5.12}$$

is constructed, where $\langle , \rangle$ denotes the usual Euclidean inner product of snapshots S. With M denoting the number of POD modes to be constructed, the first M eigenvalues of

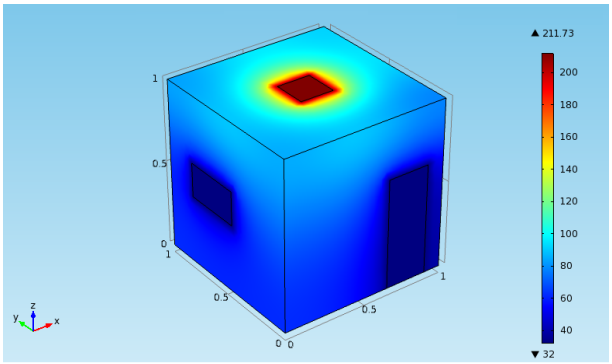

Figure 5.10: Full order model at $t = 40$ minutes

largest magnitude, $\{\lambda\}_{i=1}^{M}$, of L are found. They are sorted in descending order, and their corresponding eigenvectors $\{v\}_{i=1}^{M}$ are calculated. Each eigenvector is normalized so that

$$\|v_i\|^2 = \frac{1}{\lambda_i} \tag{5.13}$$

The orthonormal POD basis set $\{\phi_i\}_{i=1}^{M}$ is constructed according to:

$$\phi_i = \sum_{j=1}^{N} v_{i,j} S_j \tag{5.14}$$

where $v_{i,j}$ is the j^{th} component of v_i . With a POD basis in hand, the solution T of the distributed parameter model is approximated as a linear combination of POD modes, i.e.,

$$T \approx \sum_{i=1}^{M} \alpha_i \phi_i \tag{5.15}$$

This shows that POD finds a low dimensional embedding of the snapshots that preserve most of the energy as measured in a much higher dimensional solution space. It is found that taking only the largest 50 eigenvalues keeps 98% of the energy of the full order system. Figures 5.10 and 5.11 show the full order model compared to the reduced order model of 50 modes respectively, both after 40 minutes. Figures 5.12 and 5.13 show the full order model compared to the reduced order model of 50 modes respectively, both after 60 minutes. It is shown from the figures that the reduced order is so close to the full order which means that working with the reduced order is acceptable and reliable.

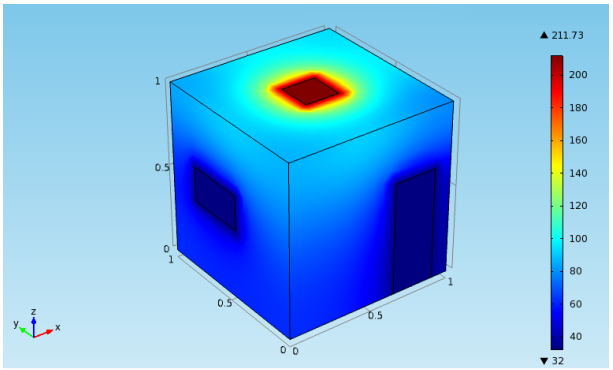

Figure 5.11: Reduced order model at $t = 40$ minutes

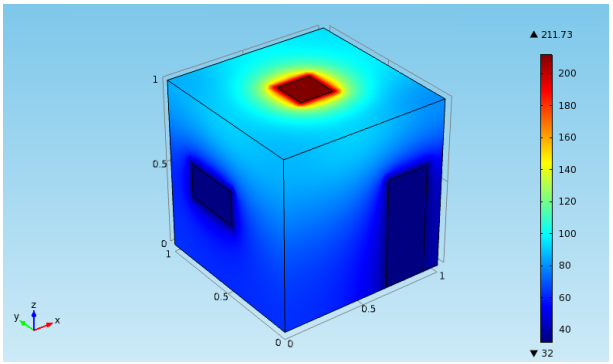

Figure 5.12: Full order model at $t = 60$ minutes

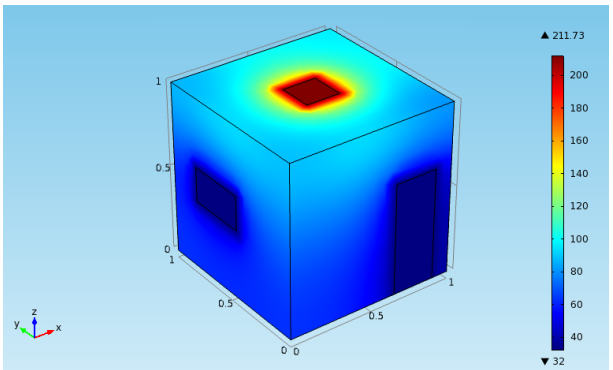

Figure 5.13: Reduced order model at $t = 60$ minutes

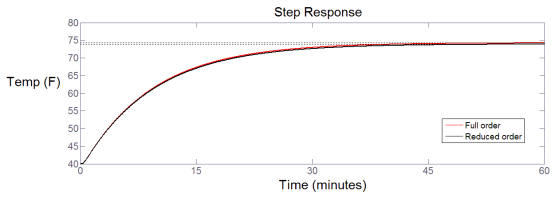

Figure 5.14: Step response for full and reduced order models

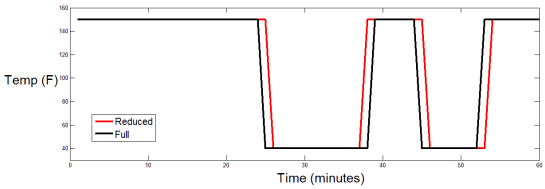

Figure 5.15: Controlled input signal for full order and reduced order controlled systems

Step response for both full and reduced controlled system is shown in Figure 5.14. The difference lies between 1 or 2 F which is very acceptable considering the large reduction ratio from 18182 states to 50. Figure 5.15 shows the input signal for full and reduced order systems. The reduced order controlled input signal leads or lags the full order controlled input signal by 1 or 2 minutes.

So In this chapter, we developed a modeling and control approach for room temperature in buildings. The approach is based on a distributed parameter model coupled with high performance computing, and modern control theory to regulate room temperature. This theory allows us to study optimal sensor location. The results obtained show excellent performance and are promising for practical implementation.

Chapter 6

Optimal Control for Wave oscillations in the Power Grid

Sudden disturbances in large electrical power networks cause electromechanical oscillations that have been modeled as spatially continuum systems that follow the dynamics of a second order nonlinear wave equation with constant voltage assumptions. In this chapter, the optimal control problem is solved for both the constant voltage continuum system and the generalized time-space voltage varying PDE. First the mechanical power is used as the control input and then the varying voltage magnitude is used as the control input.

The fundamental equation that describes the rotor dynamics in power systems is the swing equation [67]:

$$\frac{2H}{\omega}\ddot{\delta} + \omega D\dot{\delta} = P_m - P_e, \tag{6.1}$$

where H is the is the inertia constant, ω is the electrical angular velocity, D is the rotor damping constant, P_m and P_e are the mechanical and electrical power respectively, all expressed in per unit on the system base power. It represents the equation of motion of synchronous machines[46], [45], [32].

6.1 The Continuum System Constant Voltage Swing PDE

In this section, Thorp's constant voltage swing wave PDE [74] is reviewed. The distributed power system model shown in Fig. (6.1) [74] is considered. Each node is a generator that supplies a variable current and voltage producing a variable power.

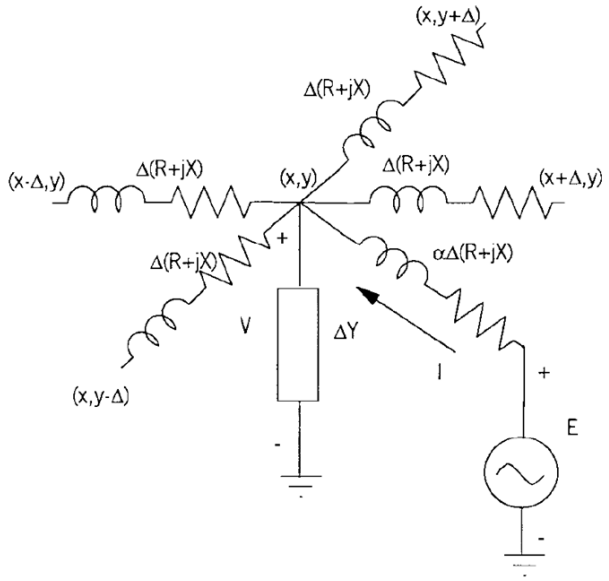

Figure 6.1: Power System Model [74]

The continuum system is described by the following second order hyperbolic wave PDE [74]:

$$\frac{\partial^2 \delta}{\partial t^2} + \nu \frac{\partial \delta}{\partial t} - v^2 \nabla^2 \delta + u^2 |\nabla \delta|^2 = P, \tag{6.2}$$

and the PDE parameters are given by:

$$v^2 = \frac{\omega V^2 sin\theta}{2h|z|}$$
$$u^2 = \frac{\omega V^2 cos\theta}{2h|z|}$$
$$P = \frac{\omega(p_m - GV^2)}{2h}$$
$$\nu = \frac{\omega^2 d}{2h}$$

where $E(x,y) = Ve^{j\delta(x,y)}$ and V is the constant voltage magnitude, δ is the angle, $z = |z|(cos\theta + jsin\theta)$ is the transmission line impedance and G is the real part of the admittance, ∇ and ∇^2 are the first and second spatial derivatives, respectively, h is the inertia constant, ω is the electrical angular velocity, d is the rotor damping constant, p_m is the mechanical power.

6.1.1 Optimal Control of the Constant Voltage Swing PDE Using Power as The Control Input

Here the mechanical power P is used as the control input that drives the angle $\delta(x,y)$ to track a reference value $\delta_r(x,y)$ for the constant voltage swing PDE. So our goal is to minimize the cost function:

$$J(P) = \frac{1}{2}\int_0^T \int_\Omega \left[|\delta(x,y,t) - \delta_r(x,y,t)|^2 + P(x,y,t)^2\right] dAdt \tag{6.3}$$

Subject to:

$$\frac{\partial^2 \delta}{\partial t^2} + \nu \frac{\partial \delta}{\partial t} - v^2 \nabla^2 \delta = P$$
$$\delta(x, y, t) = 0 \quad \text{for} \quad \delta(x, y, t) \in \partial\Omega \times [0, T]$$
$$\delta(x, y, 0) = \delta_i$$
$$\delta_t(x, y, 0) = \delta_{ti}$$
$$U_{ad} = \{P(x, y, t) \in L^2(\Omega \times (0, T)) \mid 0 \leq P(x, y, t) \leq M\}$$

where U_{ad} is the admissible control set and $0, M$ are the lower and upper control bounds respectively. Here we assume a lossless system in which $\theta = \pi/2$ then the term $u^2|\nabla\delta|^2$ is dropped out. To derive necessary conditions for optimality, the cost function is differentiated with respect to P, i.e. the map $P \mapsto J(P)$ is differentiated. However, δ contributes to $J(P)$ so the map $P \mapsto \delta(P)$ must also be differentiated.

Let

$$\psi = \lim_{\epsilon \longrightarrow 0} \frac{\delta(P + \epsilon l) - \delta(P)}{\epsilon} \tag{6.4}$$

be the sensitivity of the state with respect to the control where l is a variation function and $\epsilon > 0$.

Then the PDE that corresponds to the control $P + \epsilon l$ is:

$$\delta^\epsilon_{tt} + \nu \delta^\epsilon_t - v^2 \nabla^2 \delta^\epsilon = P + \epsilon l \tag{6.5}$$

Subtracting the constraint in (6.3) from (6.5) and dividing both sides by ϵ yields:

$$\left(\frac{\delta^\epsilon - \delta}{\epsilon}\right)_{tt} + \nu \left(\frac{\delta^\epsilon - \delta}{\epsilon}\right)_t - v^2 \nabla^2 \left(\frac{\delta^\epsilon - \delta}{\epsilon}\right) = l$$
$$L\psi =: \psi_{tt} + \nu \psi_t - v^2 \nabla^2 \psi = l$$

where $\psi \in L_2[0, T] \times H_0^1(\Omega) := \Psi$.

$L : \Psi \to \mathbb{R}$

$L^* : \mathbb{R}^* \to \Psi^* = \mathbb{R} \to \Psi$.

The operator L and the adjoint operator L^* are related by:

$$< \lambda, L\psi >=< L^*\lambda, \psi >$$

where $< ., . >$ is the L^2 inner product. For ψ_{tt}, for zero boundary conditions, Green's formula gives:

$$\int_0^T \int_\Omega \lambda \psi_{tt} dA dt = \int_0^T \int_\Omega \psi \lambda_{tt} dA dt$$

For ψ_{xx}:

$$\int_0^T \int_\Omega \lambda \nabla^2 \psi dA dt = \int_0^T \int_\Omega \psi \nabla^2 \lambda dA dt$$

For ψ_t:

$$\int_0^T \int_\Omega \lambda \psi_t dA dt = -\int_0^T \int_\Omega \psi \lambda_t dA dt$$

So the adjoint operator will be:

$$L^*\lambda = \lambda_{tt} - \nu\lambda_t - v^2\nabla^2\lambda \tag{6.6}$$

Then the adjoint PDE is:

$$L^*\lambda = \frac{\partial \text{integrand}(J)}{\partial \delta}$$

$$\lambda_{tt} - \nu\lambda_t - v^2\nabla^2\lambda = \delta^* - \delta_r \tag{6.7}$$

The sensitivity and adjoint functions are used in the differentiation of the map $P \mapsto J(P)$.

$$\lim_{\epsilon \to 0^+} \frac{J(P^* + \epsilon l) - J(P^*)}{\epsilon} \geq 0 \tag{6.8}$$

The numerator terms are:

$$J(P^*) = \frac{1}{2}\int_0^T \int_\Omega \left[|\delta^* - \delta_r|^2 + (P^*)^2\right] dAdt$$

$$J(P^* + \epsilon l) = \frac{1}{2}\int_0^T \int_\Omega \left[|\delta^{\epsilon *} - \delta_r|^2 + (P^* + \epsilon l)^2\right] dAdt$$

Then the limit (6.8) becomes:

$$\begin{aligned}
&= \lim_{\epsilon \to 0^+} \frac{1}{2}\int_0^T \int_\Omega [\frac{(\delta^{\epsilon *})^2 - (\delta^*)^2}{\epsilon} - \frac{2\delta_r(\delta^{\epsilon *} - \delta^*)}{\epsilon} + 2P^* l + \epsilon l^2] dAdt \\
&= \lim_{\epsilon \to 0^+} \frac{1}{2}\int_0^T \int_\Omega [\frac{(\delta^{\epsilon *} - \delta^*)}{\epsilon}(\delta^{\epsilon *} + \delta^*) - \frac{2\delta_r(\delta^{\epsilon *} - \delta^*)}{\epsilon} + 2P^* l + \epsilon l^2] dAdt \\
&= \frac{1}{2}\int_0^T \int_\Omega [\psi(2\delta^*) - 2\delta_r \psi + 2P^* l]\, dAdt \\
&= \int_0^T \int_\Omega [\psi(\delta^* - \delta_r) + P^* l]\, dAdt
\end{aligned}$$

Then from (6.7) we get:

$$\begin{aligned}
\int_0^T \int_\Omega [\psi(L^*\lambda) + P^* l]\, dAdt = 0 \\
\int_0^T \int_\Omega [\lambda L\psi + P^* l]\, dAdt = 0 \\
\int_0^T \int_\Omega [\lambda l + P^* l]\, dAdt = 0 \\
\int_0^T \int_\Omega [l(\lambda + P^*)]\, dAdt = 0
\end{aligned}$$

So the optimal control in the interior of U_{ad} becomes:

$$P^* = -\lambda$$

Taking into account the control bounds, the optimal control becomes:

$$P^* = min(max(-\lambda, 0), M) \tag{6.9}$$

where λ is computed by solving the coupled PDE system:

$$\delta^*_{tt} + \nu\delta^*_t - v^2\nabla^2\delta^* = min(max(-\lambda, 0), M)$$
$$\lambda_{tt} - \nu\lambda_t - v^2\nabla^2\lambda = \delta^* - \delta_r$$

where initial and boundary conditions are defined for the state PDE:

$$\delta(x, y, t) = 0 \quad \text{for} \quad \delta(x, y, t) \in \partial\Omega \times [0, T]$$
$$\delta(x, y, 0) = \delta_i$$
$$\delta_t(x, y, 0) = \delta_{ti}$$

while final and boundary conditions are defined for the adjoint PDE:

$$\lambda(x, y, t) = 0 \quad \text{for} \quad \lambda(x, y, t) \in \partial\Omega \times [0, T]$$
$$\lambda(x, y, T) = 0$$
$$\lambda_t(x, y, T) = 0$$

The difficulty in solving these coupled PDEs arises from the fact that the state PDE has initial conditions while the adjoint PDE has final conditions. One method to solve such coupled systems is the forward backward sweep method explained in [40] and [5]. The steps of the forward backward sweep algorithm is as follows:

1. Start with an initial guess for the control P^* over the domain.
2. Using the state PDE initial conditions and the values for P^*, solve δ^* forward in time.
3. Using the adjoint PDE final conditions and the values for P^* and δ^*, solve λ backward in time.

4. Update P^* by entering the new δ^* and λ into the expression of the optimal control.

5. Check convergence. Stop if the difference is negligible between this iteration and the previous one, otherwise return to step 2.

Convergence and stability of this algorithm is discussed in [23]. Figure (6.3) shows the numerical solution of a controlled system for the initial disturbance shown in Figure (6.2).

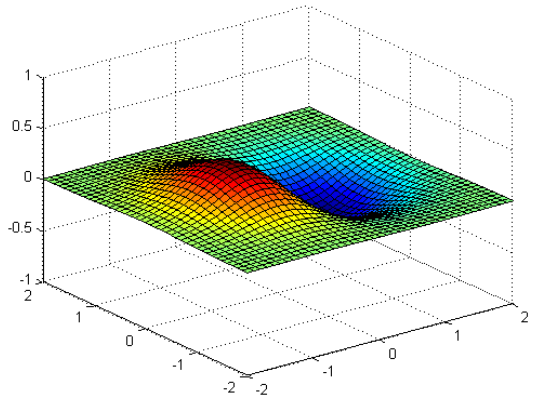

Figure 6.2: Initial disturbance

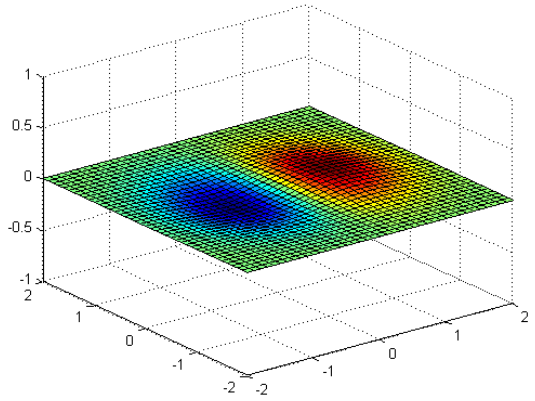

Figure 6.3: Controlled System

6.1.2 Optimal Control of the Constant Voltage Swing PDE Using Voltage as The Control Input

Although constant voltage is the assumption for the swing PDE in this case, voltage can still be used as a control input if the deviation above or below a constant value is kept minimum. We need to assume that the voltage varies only within a narrow neighborhood around a constant V_r because letting it vary freely violates the original assumption in deriving the swing PDE (6.2), then the cost function to be minimized is :

$$J(V) = \frac{1}{2}\int_0^T \int_\Omega \left[|\delta(x,y,t) - \delta_r(x,y,t)|^2 + |V(x,y,t)|^2\right] dAdt \tag{6.10}$$

Subject to:

$$\begin{aligned}
\frac{\partial^2\delta}{\partial t^2} + \nu\frac{\partial\delta}{\partial t} - \frac{\omega V^2 sin\theta}{2h|z|}\nabla^2\delta &= \frac{\omega(p_m - GV^2)}{2h} \\
\delta(x,y,t) &= 0 \quad \text{for} \quad \delta(x,y,t) \in \partial\Omega \times [0,T] \\
\delta(x,y,0) &= \delta_i \\
\delta_t(x,y,0) &= \delta_{ti} \\
U_{ad} = \{V(x,y,t) \in L^2(\Omega \times (0,T)) \mid V_r - \epsilon_v \leq V(x,y,t) &\leq V_r + \epsilon_v\}
\end{aligned}$$

where U_{ad} is the admissible control set and ϵ_v is a small positive number and $\nu, \omega, h, z, \theta, p_m, G$ are all constants. The sensitivity of the state with respect to the control input V is:

$$\begin{aligned}
\psi &:= \lim_{\epsilon \longrightarrow 0} \frac{\delta(V + \epsilon l) - \delta(V)}{\epsilon} \\
&= \lim_{\epsilon \longrightarrow 0} \frac{\delta^\epsilon - \delta}{\epsilon}
\end{aligned}$$

For the control input $V + \epsilon l$ we have:

$$\frac{\partial^2\delta^\epsilon}{\partial t^2} + \nu\frac{\partial\delta^\epsilon}{\partial t} - \frac{\omega(V+\epsilon l)^2 sin\theta}{2h|z|}\nabla^2\delta^\epsilon = \frac{\omega(p_m - G(V+\epsilon l)^2)}{2h} \tag{6.11}$$

while for the control input V we have:

$$\frac{\partial^2\delta}{\partial t^2}+\nu\frac{\partial\delta}{\partial t}-\frac{\omega V^2 sin\theta}{2h|z|}\nabla^2\delta=\frac{\omega(p_m-GV^2)}{2h} \tag{6.12}$$

Subtracting (6.12) from (6.11) and dividing both sides by ϵ yields:

$$\left(\frac{\delta^\epsilon-\delta}{\epsilon}\right)_{tt}+\nu\left(\frac{\delta^\epsilon-\delta}{\epsilon}\right)_{t}-\frac{\omega V^2 sin\theta}{2h|z|}\nabla^2\left(\frac{\delta^\epsilon-\delta}{\epsilon}\right)$$
$$-\frac{\omega l(2V+\epsilon l)sin\theta}{2h|z|}\nabla^2\delta^\epsilon=-\frac{\omega Gl(2V+\epsilon l)}{2h}$$

$$\psi_{tt}+\nu\psi_t-\frac{\omega V^2 sin\theta}{2h|z|}\nabla^2\psi-\frac{\omega l(2V)sin\theta}{2h|z|}\nabla^2\delta=-\frac{2\omega GlV}{2h}$$

Defining the operator $L\psi:=\psi_{tt}+\nu\psi_t-\frac{\omega V^2 sin\theta}{2h|z|}\nabla^2\psi$ we have:

$$L\psi=\frac{\omega l(2V)sin\theta}{2h|z|}\nabla^2\delta-\frac{2\omega GlV}{2h} \tag{6.13}$$

Then the adjoint operator will be:

$$\begin{aligned}L^*\lambda&=\lambda_{tt}-\nu\lambda_t-\frac{\omega V^2 sin\theta}{2h|z|}\nabla^2\lambda \\ &=\delta^*-\delta_r\end{aligned} \tag{6.14}$$

Now the sensitivity and adjoint functions will be used in the differentiation of the map $V\mapsto\delta(V)$.

$$\lim_{\epsilon\to 0^+}\frac{J(V^*+\epsilon l)-J(V^*)}{\epsilon}\geq 0 \tag{6.15}$$

where

$$J(V^*) = \frac{1}{2}\int_0^T \int_\Omega [|\delta^* - \delta_r|^2 + |V^* - V_r|^2] dA dt$$
$$J(V^* + \epsilon l) = \frac{1}{2}\int_0^T \int_\Omega [|\delta^{\epsilon *} - \delta_r|^2 + |V^* - V_r + \epsilon l|^2] dA dt$$

Then the limit (6.15) becomes:

$$\begin{aligned}
&\lim_{\epsilon \to 0^+} \frac{1}{2}\int_0^T \int_\Omega [\frac{(\delta^{\epsilon *})^2 - (\delta^*)^2}{\epsilon} - \frac{2\delta_r(\delta^{\epsilon *} - \delta^*)}{\epsilon} + 2V^* l + \epsilon l^2] dA dt \\
&= \lim_{\epsilon \to 0^+} \frac{1}{2}\int_0^T \int_\Omega [\frac{(\delta^{\epsilon *} - \delta^*)}{\epsilon}(\delta^{\epsilon *} + \delta^*) - \frac{2\delta_r(\delta^{\epsilon *} - \delta^*)}{\epsilon} + 2(V^* - V_r) l + \epsilon l^2] dA dt \\
&= \frac{1}{2}\int_0^T \int_\Omega [\psi(2\delta^*) - 2\delta_r \psi + 2(V^* - V_r) l] \, dA dt \\
&= \int_0^T \int_\Omega [\psi(\delta^* - \delta_r) + (V^* - V_r) l] \, dA dt \\
&= \int_0^T \int_\Omega [\psi L^* \lambda + (V^* - V_r) l] \, dA dt \\
&= \int_0^T \int_\Omega [\lambda L \psi + (V^* - V_r) l] \, dA dt \\
&= \int_0^T \int_\Omega \left[\lambda \left(\frac{\omega l 2 V^* sin\theta}{2h|z|}\nabla^2 \delta - \frac{2\omega G l V^*}{2h}\right) + (V^* - V_r) l\right] dA dt \\
&= \int_0^T \int_\Omega l \left[\lambda V^* \left(\frac{\omega sin\theta}{h|z|}\nabla^2 \delta - \frac{\omega G}{h}\right) + (V^* - V_r)\right] dA dt
\end{aligned}$$

And then the optimal control input V^* in terms of the adjoint variable λ would be:

$$V^* = \frac{V_r}{\lambda \left(\frac{\omega sin\theta}{h|z|}\nabla^2 \delta - \frac{\omega G}{h}\right) - 1} \tag{6.16}$$

And remember that the variation for V^* should be limited around V_r for practical results. Substituting the expression for V^* in (6.16) into the adjoint PDE (6.14), then substituting

also in the state PDE (6.12) yields the coupled state and adjoint PDEs:

$$\begin{aligned}\lambda_{tt} - \nu\lambda_t - \frac{\omega V^{*2} sin\theta}{2h|z|}\nabla^2\lambda &= \delta^* - \delta_r \\ \delta^*_{tt} + \nu\delta^*_t - \frac{\omega V^{*2} sin\theta}{2h|z|}\nabla^2\delta^* &= \frac{\omega(p_m - GV^{*2})}{2h}\end{aligned} \tag{6.17}$$

where initial and boundary conditions are defined for the state PDE:

$$\begin{aligned}\delta(x,y,t) &= 0 \quad \text{for} \quad \delta(x,y,t) \in \partial\Omega \times [0,T] \\ \delta(x,y,0) &= \delta_i \\ \delta_t(x,y,0) &= \delta_{ti}\end{aligned}$$

while final and boundary conditions are defined for the adjoint PDE:

$$\begin{aligned}\lambda(x,y,t) &= 0 \quad \text{for} \quad \lambda(x,y,t) \in \partial\Omega \times [0,T] \\ \lambda(x,y,T) &= 0 \\ \lambda_t(x,y,T) &= 0\end{aligned}$$

6.2 Space Dependent Voltage Magnitude Swing PDE

In this section, the PDE that describes the electromechanical wave propagation for the space varying voltage magnitude, i.e. $E(x,y) = V(x,y)e^{j\delta(x,y)}$ is derived.
The space varying generator current is then given by:

$$I(x,y) = -\frac{\Delta^2}{z}\nabla^2 E(x,y) + \Delta Y E(x,y), \tag{6.18}$$

where Y is the shunt admittance, Δ is the separation between adjacent nodes and ∇ is the space derivative. So the spatial gradient of $E(x,y)$ is:

$$\nabla E = \nabla V e^{j\delta} + V j \nabla\delta e^{j\delta} \tag{6.19}$$

where the Laplacian of E would be:

$$\begin{aligned}\nabla^2 E &= \nabla^2 V e^{j\delta} + \nabla V j \nabla\delta e^{j\delta} \\ &\quad + j[(\nabla V \nabla\delta + V\nabla^2\delta)e^{j\delta} + V j(\nabla\delta)^2 e^{j\delta}] \\ &= [\nabla^2 V - V(\nabla\delta)^2 + j(2\nabla V\nabla\delta + V\nabla^2\delta)]e^{j\delta} \end{aligned} \tag{6.20}$$

Using the current expression in (6.18), the electrical power P_e is given by:

$$\begin{aligned} P_e &= Re\{EI^*\} \\ &= Re\{Ve^{j\delta}(-\frac{\Delta^2}{z}[\nabla^2 V - V(\nabla\delta)^2 - j(2\nabla V\nabla\delta \\ &\quad + V\nabla^2\delta)]e^{-j\delta} + \Delta Y^* V e^{-j\delta})\} \end{aligned}$$

The complex exponential terms cancel and the electrical power expression simplifies to:

$$\begin{aligned} P_e &= Re\{V(-\frac{\Delta^2}{z}[\nabla^2 V - V(\nabla\delta)^2 - j(2\nabla V\nabla\delta + V\nabla^2\delta)] \\ &\quad + \Delta Y^* V)\} \end{aligned}$$

Using the complex form of the impedance $z = |z|(cos\theta + jsin\theta)$ we have:

$$\begin{aligned} P_e &= Re\{V(-\frac{\Delta^2}{|z|}[\nabla^2 V - V(\nabla\delta)^2 - j(2\nabla V\nabla\delta + V\nabla^2\delta)](cos\theta \\ &\quad - jsin\theta) + \Delta Y V)\} \\ &= V(-\frac{\Delta^2}{|z|}[(\nabla^2 V - V(\nabla\delta)^2)cos\theta - (2\nabla V\nabla\delta + V\nabla^2\delta)sin\theta] \\ &\quad + \Delta V^2 G, \end{aligned} \tag{6.21}$$

where $G = Re\{Y\}$.

The discrete swing equation parameters H, D, Z, and P_m in (6.1) translate for the continuum system into the distributed parameters $\Delta h(x,y), \Delta d(x,y), \Delta z(x,y)$, and $\Delta p_m(x,y)$ respectively. Substituting the electrical power expression (6.21) into the discrete swing

equation (6.1) and taking the continuum limits yields:

$$\frac{2h}{\omega}\frac{\partial^2\delta}{\partial t^2}+\omega d\frac{\partial\delta}{\partial t}=p_m+V(\frac{1}{|z|}[(\nabla^2V-V(\nabla\delta)^2)cos\theta \\ -(2\nabla V\nabla\delta+V\nabla^2\delta)sin\theta]-GV^2 \tag{6.22}$$

where the dependence on Δ cancels. The PDE (6.22) is also a hyperbolic second order wave equation but includes nonlinearities that didn't show up in the constant voltage swing PDE (6.2). For a particular but also practical choice of $\theta=\frac{\pi}{2}$, (6.22) simplifies to:

$$\ddot{\delta}+\nu\dot{\delta}=-\alpha(2V\nabla V\nabla\delta+V\nabla^2\delta)+\beta(p_m-GV^2) \tag{6.23}$$

where $\nu=\dfrac{\omega^2 d}{2h}, \alpha=\dfrac{\omega}{2h|z|}$ and $\beta=\dfrac{\omega}{2h}$

Figure (6.4) shows a numerical simulation for the electromechanical wave propagation for the angle δ in a continuous 2D system. Initial disturbance is a Gaussian function of space where its peak is at the center. The voltage magnitude V is allowed to have a random (uncontrolled) space variation from 0.9 to 1.1 pu. Control design for systems governed by

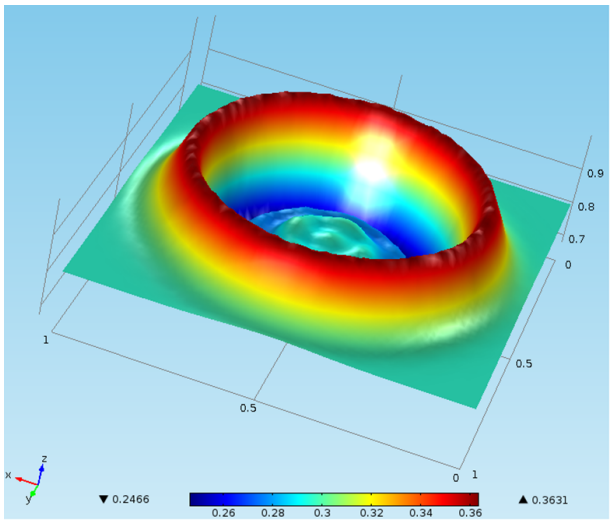

Figure 6.4: Electromechanical wave propagation in the continuous 2D system

these types of nonlinear PDEs is not an easy task due to the existence of the nonlinear

terms in the right hand side of (6.23). Optimal Control design for ODE systems is not difficult. Space discretization can be implemented on the PDE (6.23) to obtain a state space system of ODEs for which control techniques are well studied in the literature. But before discretization, since it is a second order type PDE, states x_1 and x_2 are defined as follows:

$$x_1 = \delta, \qquad \dot{x_1} = \dot{\delta}$$
$$x_2 = \dot{\delta}, \qquad \dot{x_2} = \ddot{\delta}$$

Then (6.23) can be written in the form:

$$\begin{aligned} \dot{x_1} &= x_2 \\ \dot{x_2} &= -\nu x_2 - \alpha(2VA_1VA_1 + VA_2)x_1 + \beta(p_m - G(V).(V)) \end{aligned} \tag{6.24}$$

where $\nabla = A_1$ and $\nabla^2 = A_2$ are the discretization matrices and

$$(V).(V) = \begin{pmatrix} V_1 & 0 & \cdots \\ 0 & \ddots & 0 \\ 0 & \cdots & V_N \end{pmatrix} \begin{pmatrix} V_1 \\ \vdots \\ V_N \end{pmatrix}$$

Chapter 7

Optimal Control of Droop Controlled Inverters in Islanded Microgrids

A microgrid is an interconnected low voltage group of devices consisting of distributed energy resources (DERs) and loads. It is typically seen by the main grid as a single controllable entity and it connects or disconnects to the main grid on previously defined events and therefore works in grid connected or islanded mode respectively [24]. DERs can be either AC resources such as wind turbines or DC resources such as solar panels and, for both cases, AC/AC or DC/AC voltage source inverters are needed to ensure network synchronization. A microgrid may consist of a wind turbine, solar energy resource, storage device and loads connected in a logical bus (or ring) as shown in Figure 7.1. Microgrids facilitate distributed generation and high penetration of renewable energy sources and hence increase power quality and reliability of electric supply [3]. Fault events within the connection with the main grid could lead to an islanded mode of operation [28].

Frequency control is needed in both grid connected and island modes. Control strategies for island modes are discussed in [49] where it was shown that the forced islanding of the microgrid can be performed safely under several different power importing and exporting conditions. They also showed that management of storage devices are essential to implement successful control strategies. In this chapter we take advantage of the existence of storage devices to provide a desired feasible control flexibility to respond to renewable energy sources that do not have a well predicted power generation behavior. In a grid connected mode, the

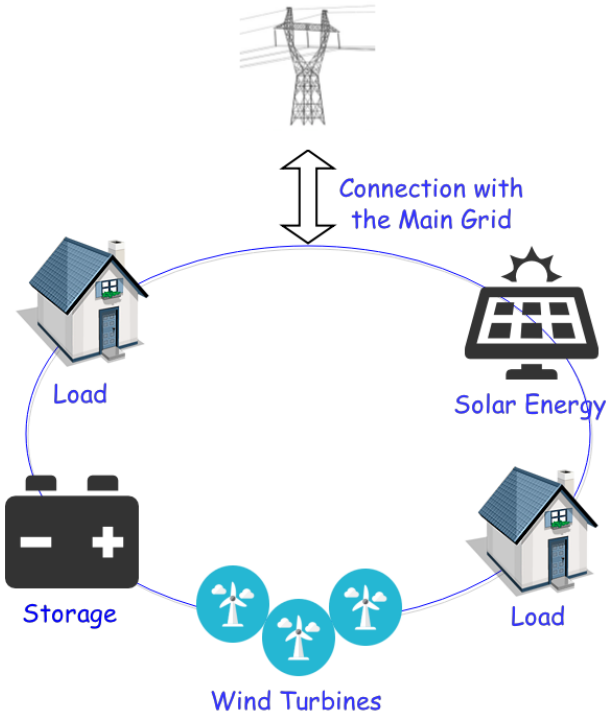

Figure 7.1: Microgrid basic elements

microgrid - depending on the amount of power generated and consumed - acts as either a load when the power consumption within the microgrid exceeds the supply, or as a generator when the supply exceeds the consumption. The latter case is called power penetration where the grid injects power to the main grid [43]. Although this penetration reduces the overall amount of power needed to be supplied by the main grid, the fluctuating and intermittent nature of this renewable generation causes variations of power flow that can significantly affect the operation of the electrical grid and causes frequency instabilities [31]. Wind generation for instance is a growing renewable energy resource but a known challenge is to effectively integrate a significant amount of wind power into the power network [22].

Figures (7.2) and (7.3) show a 24 hours simulation of power consumption and supply for two households that use solar energy resources.The black curve is the amount of power supplied by the main grid, the blue curve is the household consumption while the red curve is the generated power from the solar energy resources. The simulation starts at 12:00 am at night where there is no solar energy generation so the power consumption equals exactly the power supplied by the grid. In the morning, the solar energy generator starts generating

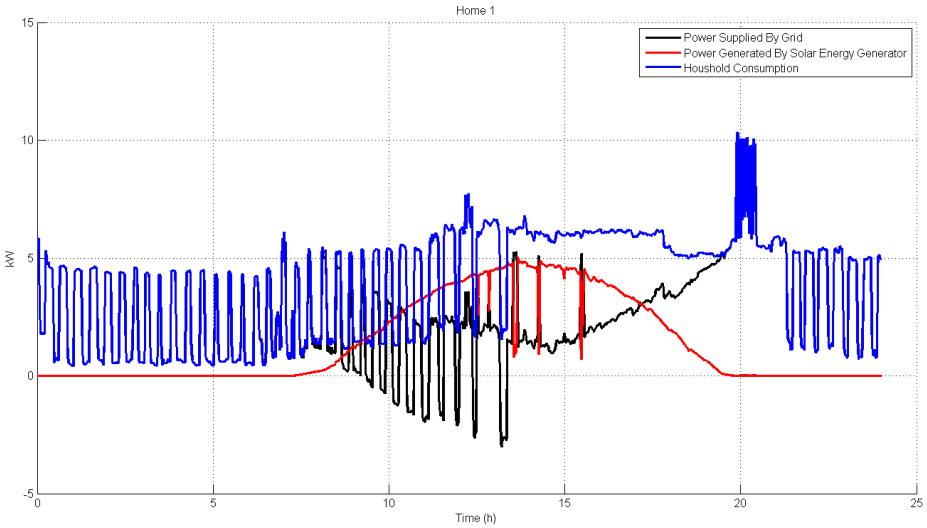

Figure 7.2: Penetration due to Solar Energy Generation in Home 1

power and therefore the main grid supply decreases. The maximum solar energy generation occurs in the afternoon time where the grid supply becomes negative, which means that this household is now injecting power into the main grid and therefore is seen as a generator.

So the problem of interest is how to use the droop values at the inverters in order to achieve frequency stability around the nominal value. In this chapter we design the optimal controller for the islanded mode while the grid connected mode will be analyzed in future work. Many control strategies have been discussed in the literature, but they assume either linear models or linearized ones. In [38] and [10], a control scheme based on droop concepts to operate inverters feeding a standalone ac system is presented. Some droop control methods are proposed in [41], [30], and [54]. Here we develop an optimal control algorithm for the nonlinear model formulation.

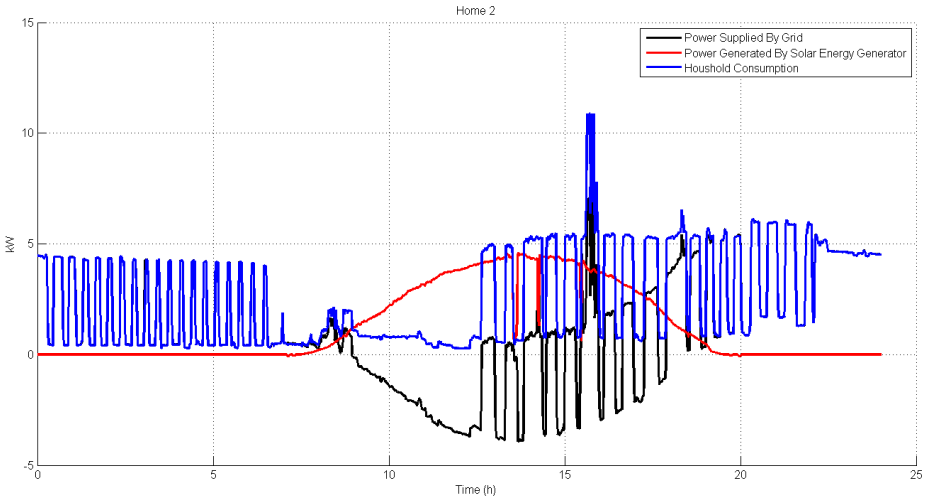

Figure 7.3: Penetration due to Solar Energy Generation in Home 2

7.1 Microgrid Model

In a microgrid like the one shown in figure (7.5) that includes N inverters, the electrical active power injected into the network at the ith inverter is given by [32]

$$P_{e,i} = \sum_{j=1}^{N} E_i E_j [B_{ij} \sin(\delta_i - \delta_j) + G_{ij}(\delta_i - \delta_j)], \tag{7.1}$$

where E_i, E_j are the nodal voltage magnitudes at inverters i and j respectively, δ_i, δ_j are the nodal voltage phases at inverters i and j respectively, B_{ij}, G_{ij} are the real and imaginary parts of $y_{ij} = B_{ij} + jG_{ij}$ respectively, where y_{ij} is the ijth entry in the nodal admittance matrix Y.

For a pure inductive admittance matrix Y, (7.1) becomes:

$$P_{e,i} = \sum_{j=1}^{N} E_i E_j B_{ij} \sin(\delta_i - \delta_j) \tag{7.2}$$

In frequency droop control, the power demand changes the frequency ω_i at inverter i by

$$\omega_i = \omega^* - (d_i P_{e,i} - P_i^*), \tag{7.3}$$

where ω^* is the nominal frequency, P_i^* is the nominal active power injection at inverter i and d_i is the ith droop coefficient. The frequency droop controller (7.3) can be written as

$$\dot{\delta}_i = P_i^* - d_i P_{e,i}, \tag{7.4}$$

where $\dot{\delta}_i = \omega_i - \omega^*$ is the frequency deviation from the nominal frequency ω^* at inverter i [70].

Substituting (7.2) in (7.4) gives the dynamics:

$$\dot{\delta}_i = P_i^* - d_i \sum_{j=1}^{N} E_i E_j B_{ij} \sin(\delta_i - \delta_j), \tag{7.5}$$
$$\delta_i(0) = \delta_i^0,$$

It has been shown by [70] that for a microgrid model whose elements are connected in parallel as shown in figure (7.5) and described by (7.5) is equivalent to a network of n Kuramoto phase coupled oscillators model given by [35]:

$$\dot{\delta}_i = \Omega_i - d_i \sum_{j=1}^{N} a_{ij} \sin(\delta_i - \delta_j), \tag{7.6}$$

where $\delta_i \in S^1$ (the unit circle) is the phase of oscillator i, Ω_i is the natural frequency, a_{ij} is the coupling strength between oscillators i and j, and d_i is a the ith oscillator coefficient. A Kuramoto oscillator network is shown in figure (7.4).

In the next section we show the existence of the optimal control problem.

7.2 The optimal control Problem formulation and existence of solution

In this section, we use the approach discussed in [39] to show the existence of solution. Let $r(t) = \left| \frac{1}{N} \sum_{i=1}^{N} e^{j\delta_i(t)} \right|$ quantify the synchrony in the network such that $r(t) = 1$ refers to a perfectly synchronized network while $r(t) = 0$ means there is no synchronization [73].
So the optimization problem is:

$$\begin{aligned} \sup_{D \in U} J(D) = & \int_0^T r^2(\delta, D) dt \\ = & \int_0^T \frac{1}{N^2} \left[\sum_{j=1}^{N} \sin(\delta_j)^2 + \sum_{j=1}^{N} \cos(\delta_j)^2 \right] dt, \end{aligned} \tag{7.7}$$

subject to the constraints:
$\dot{\delta}_i = P_i^* - d_i \sum_{j=1}^{N} E_i E_j B_{ij} \sin(\delta_i - \delta_j)$,
$\delta_i(0) = \delta_i^0$,

where $\delta = [\delta_1, \cdots, \delta_N]^T$ is the phase vector at nodes $1, \cdots, N$ and is also called the states vector, $D = [d_1, \cdots, d_N]^T$ is the vector of droop coefficients at nodes $1, \cdots, N$ and is also called the controls vector. A practical constraint for D is that it should be bounded, i.e. $\|D\| \leq C$ for some constant C where $\| \cdot \|$ is the Euclidean norm, so U in (7.7) is the set of feasible controls defined as:

$$U := \{D \in R^N : \|D\| \leq C\} \tag{7.8}$$

Theorem 7.1. *A solution exists for the optimization problem (7.7).*

Proof. Let D^* denotes the optimal control vector when they exist and δ^* denotes the corresponding optimal states vector. Choose a sequence $\{D^n\}$ in U such that

$$J(D^n) = \max_{D \in U} J(D) \tag{7.9}$$

U is a closed and bounded subset of R^N, then there exists a subsequence D^n that converges to an element $D^* \in U$. For a fixed and finite final time T, and bounded states derivatives, the states δ_i^n corresponding to the controls D^n are then uniformly bounded and equicontinuous, which implies (by Arzela–Ascoli Theorem) that there exists a subsequence $\{\delta^n\}$ and a continuous function $\delta^*(t)$ such that $\delta^n(t)$ uniformly converges to $\delta^*(t)$, then the following is true:

$$\int_0^T \frac{dv(t)}{dt}\delta_i^*(t)dt = -\int_0^T v(t)\frac{d\delta_i^*(t)}{dt}dt \tag{7.10}$$

$$= -\int_0^T v(t)\left(P_i^* - d_i^*\sum_{j=1}^N E_i E_j B_{ij}\sin(\delta_i^* - \delta_j^*)\right)dt,$$

for all $v \in C^\infty(0,T)$. Then δ_i^* is absolutely continuous and satisfies [17]:

$$\frac{d\delta_i^*}{dt} = P_i^* - d_i^*\sum_{j=1}^N E_i E_j B_{ij}\sin(\delta_i^* - \delta_j^*) \tag{7.11}$$

almost everywhere, that is δ^* corresponds to D^*. Finally:

$$\begin{aligned} J(D^*) = & \int_0^T r^*(t)^2 dt \\ = & \lim_{n\to\infty}\int_0^T r^n(t)^2 dt \\ = & \lim_{n\to\infty} J(D^n) \\ = & \sup_{D\in U} J(D) \end{aligned}$$

So the optimal control exists and the theorem is proved. □

In the next section, the solution of the optimal control problem is computed.

7.3 Solution of the Optimal Control Problem

Let $g(\delta, D) := \dot{\delta}$ be a column vector function and $f(\delta, D) = r^2$ be a scaler function where r is defined in (7.7), then we define the adjoint row vector function $y = [y_1, \cdots, y_N]$ that

satisfies [40]:

$$\dot{y} = -yg_\delta(\delta, D) - f_\delta(\delta, D) \tag{7.12}$$

$$y(T) = 0 \tag{7.13}$$

where f_δ denotes a row vector of length N of the partial derivatives of f with respect to the vector δ and g_δ denotes an $N \times N$ Jacobean matrix:

$$g_\delta(\delta, D) = \begin{pmatrix} \frac{d\dot{\delta}_1}{d\delta_1} & \cdots & \frac{d\dot{\delta}_1}{d\delta_N} \\ \vdots & \ddots & \vdots \\ \frac{d\dot{\delta}_N}{d\delta_1} & \cdots & \frac{d\dot{\delta}_N}{d\delta_N} \end{pmatrix} \tag{7.14}$$

Using (7.5), the expression for $g_\delta(\delta, D)$ can be written as:

$$\begin{pmatrix} \sum_{j=1}^{N} d_1 E_1 E_j B_{1j} \cos(\delta_1 - \delta_j) & -d_1 E_1 E_2 B_{12} \cos(\delta_1 - \delta_2) & \ldots \\ -d_2 E_2 E_1 B_{21} \cos(\delta_2 - \delta_1) & \sum_{j=1}^{N} d_2 E_2 E_j B_{2j} \cos(\delta_2 - \delta_j) & \ldots \\ \vdots & \ddots & \vdots \\ -d_N E_N E_1 B_{N1} \cos(\delta_N - \delta_1) & \ldots & \sum_{j=1}^{N} d_N E_N E_j B_{Nj} \cos(\delta_N - \delta_j) \end{pmatrix}$$

By differentiating f w.r.t. δ, the ith component of f_δ is:

$$\begin{aligned} f_{\delta i}(\delta, D) = & \frac{2}{N^2} \sum_{j=1}^{N} \sin(\delta_j)\cos(\delta_i) - \sin(\delta_i)\cos(\delta_j) \\ = & \frac{2}{N^2} \sum_{j=1}^{N} \sin(\delta_j - \delta_i) \end{aligned} \tag{7.15}$$

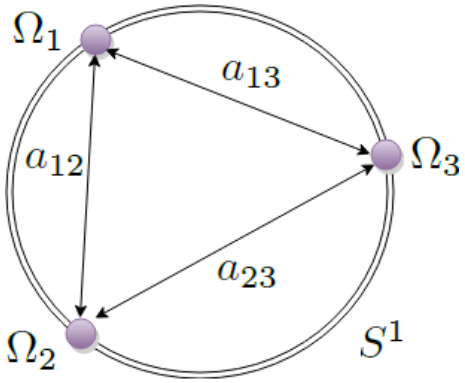

Figure 7.4: A Kuramoto oscillator network

Then the ith component of (7.12) can then be written as:

$$\dot{y}_i = \sum_{j=1, j\neq i}^{N} (y_j - y_i) d_i E_i E_j B_{ij} \cos(\delta_i - \delta_j) - \frac{2}{N^2} \sum_{j=1}^{N} \sin(\delta_j - \delta_i) \tag{7.16}$$

Now we will find the optimal control D in terms of the adjoint variable y. Using the maximum principle theory, we define the Hamiltonian [51]:

$$H(t, \delta, D, y) = yg(t, \delta, D) + f(t, \delta, D) \tag{7.17}$$

Differentiating H w.r.t. the control D yields:

$$\frac{dH(t, \delta, D, y)}{dD} = y \frac{dg(t, \delta, D)}{dD} \tag{7.18}$$

Finally the optimal control D^* is obtained when $\dfrac{dH}{dD} = 0$, or :

$$y \frac{dg(t, \delta, D^*)}{dD} = 0 \tag{7.19}$$

In the next section we present simulation results of operating such systems in practice.

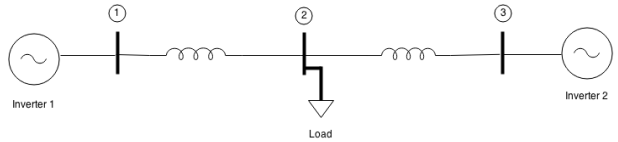

Figure 7.5: A microgrid of 2 paralleled inverters and a load

7.4 Simulation Case

The microgrid shown in figure (7.1) can be mathematically viewed as the parallel circuit shown in figure (7.5). It includes two inverters and a load. Microgrid parameters are shown in table (7.1). The load in this case scenario suddenly changes from 2.5 KW to 5 KW at $t = 2$ and then back to 2.5 KW at $t = 4$.

Table 7.1: Microgrid Parameters

Parameter	Value
Load Active Power (for $t \in [0, 2]$)	-2.5 KW
Load Active Power (for $t \in [2, 4]$)	-5 KW
Load Active Power (for $t \in [4, 6]$)	-2.5 KW
Nominal Frequency	60 Hz
Line inductance between bus 1 and 2	0.7 mH
Line inductance between bus 2 and 3	0.5 mH
Power ratings for inverter 1	4 KW
Power ratings for inverter 2	5 KW
Nominal Voltage for inverter 1	120 V
Nominal Voltage for inverter 2	122 V

Before solving for the optimal problem discussed in the last section, let us demonstrate the case in which the droop coefficients are constants such that $d_1 = 1/2000$ and $d_2 = 1/3000$. Using the microgrid data in table (7.1), we get the results for frequency, active power generation and angles shown in figures (7.6), (7.7) and (7.8) respectively.

As we see, while constant drops can bring the system frequency close to $60Hz$, it is still not clear how to choose the best and most efficient values. So what are the optimal values for the droops is what we show in this section. Using the same microgrid model and the same parameters, we solve the optimization problem in section 4 to find the optimum set of droop coefficients. Figure (7.9) shows the frequency measured at inverter 1 while figure

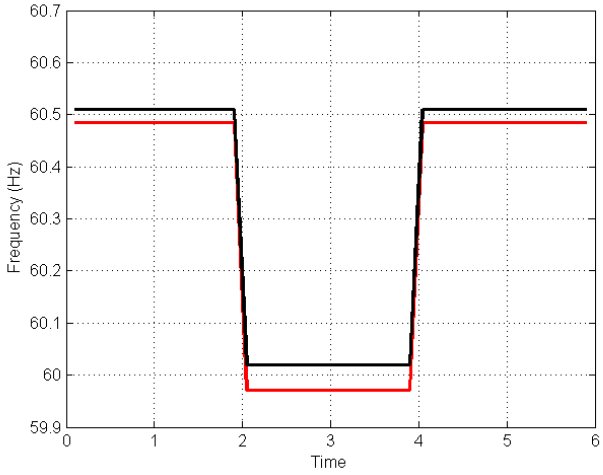

Figure 7.6: Frequencies measured at inverter1

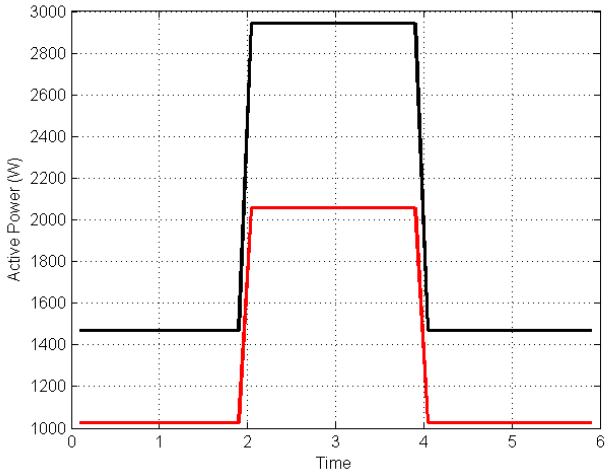

Figure 7.7: Active Power generated from inverters 1 and 2

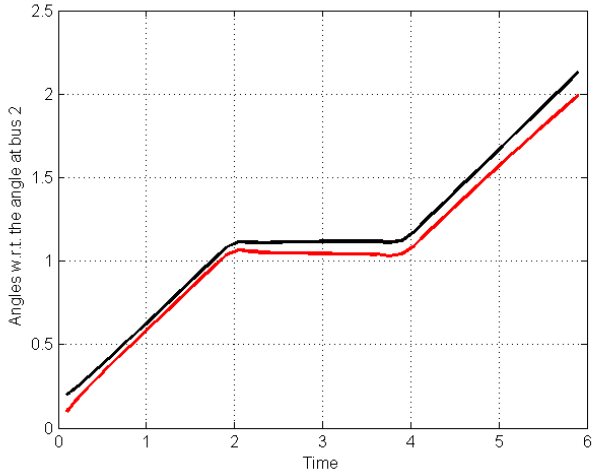

Figure 7.8: Angles for inverters 1 and 2

(7.10) shows the active power supplied by the two inverters over time and there we can see the performance of our optimal control algorithm.

We have described a distributed optimal controller for an islanded microgrid with a Kuramoto oscillators nonlinear model. We have borrowed results from the optimal control theory area, namely, the maximum principle optimization theory. We formulated the objective as an optimal control problem and we showed that a solution exists and found it. Finally, we presented a simulation case to illustrate the optimal controller performance.

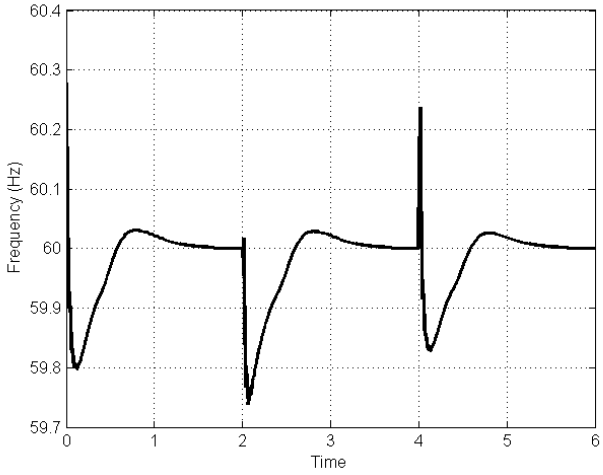

Figure 7.9: Frequencies measured at inverter1

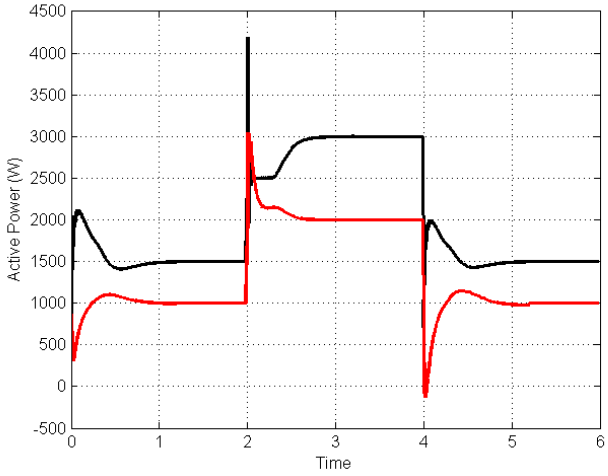

Figure 7.10: Active Power generated from inverters 1 and 2

Chapter 8

Conclusions

New methods that make POD more accurate are investigated. In chapter 2, POD is applied locally to clusters instead of applying it to the global system. Each cluster contains relatively close in distance behavior within itself, and considerably far with respect to other clusters. Three different clustering schemes in time, space and space-time are introduced. For time clustering, time snapshots of the solution are grouped into clusters where the solution exhibits significantly different features and a local basis is pre-computed and assigned to each cluster. Space clustering is done in a similarly for the space vectors of the solution instead of snapshots, and finally space-time clustering is applied through a hybrid clustering scheme that combines space and time behavior together. Our methods are applied to reduce a nonlinear convective PDE system governed by the Burgers' equation for fluid flows over 1D and 2D domains. The proper orthogonal decomposition without the usual integral or inner product constraints is extended to general Hilbert spaces, such as Sobolev spaces, using functional analytic methods.

Nonlinear systems of quadratic type nonlinearity with the presence of a linear term are the reduced order finite dimensional version of the fluid flow systems described by the Navier Stokes equations. The one dimensional version of the Navier Stokes PDE reduces to the one dimensional Burgers' equation. In chapter 3, an analytical solution is presented for the one dimensional quadratic system with homogeneous type Dirichlet Conditions. The resulting finite dimensional nonlinear system for both PDEs has the same structure, hence the result in this note applies also to the Navier Stokes system. The same chapter includes deriving the

POD model reduction, Galerkin projection, and finally the nonlinear optimal control design for the 1D Burgers equation PDE. Explicit expressions for the adjoint and state equations are derived in order to avoid numerical instabilities. The nonlinear control design is shown to be significantly better than the linearized one when the nonlinearities in the system are dominant.

In chapter 4, complete and detailed approach for the Orthogonal Locality Preserving Projections (OLPP) modes computation for the incompressible Navier Stokes PDE that governs the dynamics of the NACA 0015 airfoil fluid flow problem is presented. Close snapshots in the full order model are forced to stay close in the reduced order model by defining an optimization problem that preserves local distances. The POD reduced model is computed for the same problem. The PID closed loop flow separation control problem is shown in which fluid suction on part of the airfoil boundary is used to control flow separation on the boundary layer.

The heat equation is used as an application of a linear PDE system. The building sector in the United States consumes a large part of the energy used and is responsible for nearly 40% of greenhouse gas emissions. It is therefore economically and environmentally important to reduce the building energy consumption to realize massive energy savings. In chapter 5, a method to control room temperature in buildings is proposed. The approach is based on a distributed parameter model represented by a three dimensional (3D) heat equation in a room with heater/cooler located at ceiling. The latter is resolved using finite element methods, and results in a model for room temperature with thousands of states. The latter is not amenable to control design. A reduced order model of only few states is then derived using POD. A Linear Quadratic Regulator (LQR) is computed based on the reduced model, and applied to the full order model to control room temperature.

Sudden disturbances in large electrical power networks cause electromechanical oscillations that have been modeled as spatially continuum systems that follow the dynamics of a second order nonlinear wave equation with constant voltage assumptions. In chapter 6, the optimal control problem is solved for both the constant voltage continuum system and the generalized time-space voltage varying PDE. First the mechanical power is used as the control input and then the varying voltage magnitude is used as the control input.

For an islanded microgrid modeled by a Kuramoto oscillators nonlinear model, the distributed optimal controller is designed in chapter 7 using the maximum principle optimization theory. Synchrony is quantified in terms of phases and droop coefficients at the inverters in the microgrid and then it is maximized. The solution existence of the distributed optimal control problem is proved and the solution is found. Performance is evaluated in a simulation case.

Bibliography

[1] Amsallem, D., Zahr, M. J., and Farhat, C. (2012). Nonlinear model order reduction based on local reduced-order bases. *International Journal for Numerical Methods in Engineering*, 92(10):891–916. 2

[2] Anderson, J. (2005). *Introduction to Flight*. McGraw-Hill series in aeronautical and aerospace engineering. McGraw-Hill Higher Education. 44, 52

[3] Barker, P. and Herman, D. (2002). Technical and economic feasibility of microgrid- based power systems. In *Proceedings of the Seventh EPRI Distributed Resources Conference and Exhibition, Dallas, TX*, pages 20–22. 89

[4] Barnwell, R. and Hussaini, M. (1992). *Natural laminar flow and laminar flow control*. ICASE/NASA LaRC series. Springer-Verlag. 43

[5] Betts, J. (2001). *Practical Methods for Optimal Control Using Nonlinear Programming*. Advances in design and control. Society for Industrial and Applied Mathematics. 39, 80

[6] Borggaard, J., Burns, J. A., Surana, A., and Zietsman, L. (2009). Control, estimation and optimization of energy efficient buildings. In *2009 American Control Conference*, pages 837–841. 63

[7] Burgers, J. (1948). A mathematical model illustrating the theory of turbulence. volume 1 of *Advances in Applied Mechanics*, pages 171 – 199. Elsevier. 17

[8] Burns, J. A. and King, B. B. (1994). Optimal sensor location for robust control of distributed parameter systems. In *IEEE CONFERENCE ON DECISION AND CONTROL*, volume 4, pages 3967–3967. INSTITUTE OF ELECTRICAL ENGINEERS INC (IEE). 69

[9] Bushnell, D. (1990). *Viscous Drag Reduction in Boundary Layers*. Progress in astronautics and aeronautics. American Institute of Aeronautics and Astronautics. 43

[10] Chandorkar, M., Divan, D., and Adapa, R. (1993). Control of parallel connected inverters in standalone ac supply systems. *Industry Applications, IEEE Transactions on*, 29(1):136–143. 91

[11] Cho, W., Sahyoun, S., Djouadi, S. M., Koschan, A., and Abidi, M. A. (2015). Reduced-order spectral data modeling based on local proper orthogonal decomposition. *Journal of the Optical Society of America A*, 32(5):733–740. 4

[12] Clancy, J. (2006). *Aerodynamics*. Sterling Bks. Sterling Book House. 44, 52

[13] Crank, J. and Nicolson, P. (1947). A practical method for numerical evaluation of solutions of partial differential equations of the heat-conduction type. *Mathematical Proceedings of the Cambridge Philosophical Society*, 43:50–67. 65

[14] Djouadi, S. M. (2008). On the optimality of the proper orthogonal decomposition and balanced truncation. In *Decision and Control, 2008. CDC 2008. 47th IEEE Conference on*, pages 4221–4226. IEEE. 12

[15] Djouadi, S. M., Camphouse, R. C., and Myatt, J. H. (2008). Reduced order models for boundary feedback flow control. In *2008 American Control Conference*, pages 4005–4010. 2

[16] Djouadi, S. M. and Sahyoun, S. (2012). On a generalization of the proper orthogonal decomposition and optimal construction of reduced order models. In *2012 American Control Conference (ACC)*, pages 1436–1441. IEEE. 4

[17] Evans, L., editor (2002). *Partial Differential Equations*. The American Mathematical Society,. 95

[18] Gad-el Hak, M. (1994). Interactive control of turbulent boundary layers-a futuristic overview. *AIAA journal*, 32(9):1753–1765. 43

[19] Gad-el Hak, M. (2001). *The MEMS Handbook*. Mechanical and Aerospace Engineering Series. CRC Press. 43

[20] Gad-el Hak, M. (2006). *Flow Control: Passive, Active, and Reactive Flow Management*. Cambridge University Press. 43

[21] Georges, D. (1995). The use of observability and controllability gramians or functions for optimal sensor and actuator location in finite-dimensional systems. In *Decision and*

Control, 1995., Proceedings of the 34th IEEE Conference on, volume 4, pages 3319–3324 vol.4. 69

[22] Georgilakis, P. S. (2008). Technical challenges associated with the integration of wind power into power systems. *Renewable and Sustainable Energy Reviews*, 12(3):852 – 863. 90

[23] Hackbusch, W. (1978). A numerical method for solving parabolic equations with opposite orientations. *Computing*, 20(3):229–240. 39, 81

[24] Hatziargyriou, N., Asano, H., Iravani, R., and Marnay, C. (2007). Microgrids. *Power and Energy Magazine, IEEE*, 5(4):78–94. 89

[25] Henri, T. and Yvon, J.-P. (2005). *Convergence Estimates of POD-Galerkin Methods for Parabolic Problems*, pages 295–306. Springer US, Boston, MA. 8, 12

[26] Holmes, P., Lumley, J., and Berkooz, G. (1998). *Turbulence, Coherent Structures, Dynamical Systems and Symmetry*. Cambridge Monographs on Mechanics. Cambridge University Press. 2, 7, 8, 20, 47

[27] Hough, G. (1980). *Viscous Flow Drag Reduction*. Number v. 72 in Progress in astronautics and aeronautics. American Institute of Aeronautics and Astronautics. 43

[28] Katiraei, F., Iravani, M., and Lehn, P. (2005). Micro-grid autonomous operation during and subsequent to islanding process. *Power Delivery, IEEE Transactions on*, 20(1):248–257. 89

[29] Khalil, H. (2002). *Nonlinear Systems*. Pearson Education. Prentice Hall. 3

[30] Kim, J., Guerrero, J., Rodriguez, P., Teodorescu, R., and Nam, K. (2011). Mode adaptive droop control with virtual output impedances for an inverter-based flexible ac microgrid. *Power Electronics, IEEE Transactions on*, 26(3):689–701. 91

[31] Kroposki, B., Lasseter, R., Ise, T., Morozumi, S., Papatlianassiou, S., and Hatziargyriou, N. (2008). Making microgrids work. *Power and Energy Magazine, IEEE*, 6(3):40–53. 90

[32] Kundur, P. (1994). *Power System Stability and Control*. McGraw-Hill. 74, 92

[33] Kunisch, K. and Volkwein, S. (2001). Galerkin proper orthogonal decomposition methods for parabolic problems. *Numerische Mathematik*, 90(1):117–148. 8, 12

[34] Kunisch, K. and Volkwein, S. (2002). Galerkin proper orthogonal decomposition methods for a general equation in fluid dynamics. *SIAM Journal on Numerical Analysis*, 40(2):492–515. 8, 12

[35] Kuramoto, Y. (1975). Self-entrainment of a population of coupled non-linear oscillators. *, Int. Symposium on Mathematical Problems in Theoretical Physics*, 35:420–422. 93

[36] Kwakernaak, H. and Sivan, R. (1972). *Linear optimal control systems*. Wiley-Interscience publication. Wiley Interscience. 68

[37] Lachmann, G. (1961). *Boundary layer and flow control: its principles and application*. Boundary Layer and Flow Control: Its Principles and Application. Pergamon Press. 43

[38] Lasseter, R. and Piagi, P. (2000). Providing premium power through distributed resources. In *System Sciences, 2000. Proceedings of the 33rd Annual Hawaii International Conference on*, pages 9 pp.–. 91

[39] Leander, R., Lenhart, S., and Protopopescu, V. (2012). Using optimal control theory to identify network structures that foster synchrony. *Physica D: Nonlinear Phenomena*, 241(5):574 – 582. 94

[40] Lenhart, S. and Workman, J. (2007). *Optimal Control Applied to Biological Models*. Chapman & Hall/CRC Mathematical and Computational Biology. CRC Press. 39, 80, 96

[41] Li, Y. and Li, Y. W. (2011). Power management of inverter interfaced autonomous microgrid based on virtual frequency-voltage frame. *Smart Grid, IEEE Transactions on*, 2(1):30–40. 91

[42] Lumley, J. (1970). *Stochastic Tools in Turbulence*. New York Academic Press. 2

[43] Mathiesen, B. V., Lund, H., and Karlsson, K. (2011). 100% renewable energy systems, climate mitigation and economic growth. *Applied Energy*, 88(2):488 – 501. 90

[44] Moin, P. and Bewley, T. (1994). Feedback control of turbulence. *Applied Mechanics Reviews*, 47(6S):S3–S13. 43

[45] Momoh, J. and El-Hawary, M. (1999). *Electric Systems, Dynamics, and Stability with Artificial Intelligence Applications*. Power Engineering (Willis). Taylor & Francis. 74

[46] Mondal, D., Chakrabarti, A., and Sengupta, A. (2014). *Power System Small Signal Stability Analysis and Control*. Elsevier Science & Technology Books. 74

[47] Moore, B. (1981). Principal component analysis in linear systems: Controllability, observability, and model reduction. *IEEE Transactions on Automatic Control*, 26(1):17–32. 1

[48] Niyogi, X. (2004). Locality preserving projections. 43, 49

[49] Peas Lopes, J., Moreira, C., and Madureira, A. (2006). Defining control strategies for microgrids islanded operation. *Power Systems, IEEE Transactions on*, 21(2):916–924. 89

[50] Peyret, R. and Taylor, T. (1982). *Computational Methods for Fluid Flow*. Scientific Computation. Springer Berlin Heidelberg. 1

[51] Pontryagin, L. (1987). *Mathematical Theory of Optimal Processes*. Classics of Soviet Mathematics. Taylor & Francis. 97

[52] Prandtl, L. (1904). Uber flussigkeits bewegung bei sehr kleiner reibung. *Verhaldlg III Int. Math. Kong*, pages 484–491. 43

[53] Riesz, F. and Nagy, B. (2012). *Functional Analysis*. Dover Books on Mathematics. Dover Publications. 14

[54] Rokrok, E. and Golshan, M. (2010). Adaptive voltage droop scheme for voltage source converters in an islanded multibus microgrid. *Generation, Transmission Distribution, IET*, 4(5):562–578. 91

[55] Sahyoun, S. and Djouadi, S. (2013). Local proper orthogonal decomposition based on space vectors clustering. In *3rd International Conference on Systems and Control*, pages 665–670. IEEE. 4

[56] Sahyoun, S., Djouadi, S., and Shankar, M. (2015a). Optimal control of droop controlled inverters in islanded microgrids. *IFAC-PapersOnLine*, 48(30):363–368. 5

[57] Sahyoun, S. and Djouadi, S. M. (2011). Nonlinear model reduction for fluid flows. In *Proceedings of the 2011 American Control Conference*, pages 1765–1769. IEEE. 4

[58] Sahyoun, S. and Djouadi, S. M. (2014a). Control of nonlinear pdes based on space vectors clustering reduced order systems. *IFAC Proceedings Volumes*, 47(3):5181–5186. 4

[59] Sahyoun, S. and Djouadi, S. M. (2014b). Nonlinear model reduction using space vectors clustering pod with application to the burgers' equation. In *2014 American Control Conference*, pages 1661–1666. IEEE. 4

[60] Sahyoun, S. and Djouadi, S. M. (2014c). Time, space, and space-time hybrid custering pod with application to the burgers' equation. In *53rd IEEE Conference on Decision and Control*, pages 2088–2093. IEEE. 4

[61] Sahyoun, S. and Djouadi, S. M. (2016). Nonlinear optimal control of fluid flows governed by the burgers equation reduced order model. In *Proceedings of the 22nd International Symposium on Mathematical Theory of Networks and Systems*, pages 339–344. SIAM. 4

[62] Sahyoun, S. and Djouadi, S. M. (2017). Orthogonal locality preserving model reduction and flow separation control for incompressible navier stokes equations. In *Accepted 2017 American Control Conference*. IEEE. 4

[63] Sahyoun, S., Djouadi, S. M., Tomsovic, K., and Lenhart, S. (2015b). Optimal distributed control for continuum power systems. In *2015 Proceedings of the Conference on Control and its Applications*, pages 416–422. Society for Industrial and Applied Mathematics. 5

[64] Sahyoun, S., Dong, J., and Djouadi, S. M. (2012a). Reduced order modeling for fluid flows subject to quadratic type nonlinearities. In *Decision and Control (CDC), 2012 IEEE 51st Annual Conference on*, pages 961–966. IEEE. 4

[65] Sahyoun, S., Dong, J., and Djouadi, S. M. (2013). Reduced order modeling for fluid flows based on nonlinear balanced truncation. In *2013 American Control Conference*, pages 1284–1289. IEEE. 4

[66] Sahyoun, S., Nelson, C., Djouadi, S. M., and Kuruganti, T. (2012b). Control and room temperature optimization of energy efficient buildings. In *Control Applications (CCA), 2012 IEEE International Conference on*, pages 962–967. IEEE. 5

[67] Sauer, P. and Pai, M. (2006). *Power System Dynamics and Stability*. Stipes Publishing L.L.C. 74

[68] Schatten, R. (1960). *Norm Ideals of Completely Continuous Operators*. Ergebnisse der Mathematik und ihrer Grenzgebiete. Springer. 12, 13, 14, 15

[69] Scherpen, J. M. A. (1993). Balancing for unstable nonlinear systems. In *Decision and Control, 1993., Proceedings of the 32nd IEEE Conference on*, pages 14–19 vol.1. 1

[70] Simpson-Porco, J. W., Dorfler, F., and Bullo, F. (2013). Synchronization and power sharing for droop-controlled inverters in islanded microgrids. *Automatica*, 49:2603–2611. 93

[71] Sirovich, L. (1987). Turbulence and the dynamics of coherent structures parts i-iii. *Quarterly of Applied Mathematics*, (3):561–582. 2

[72] Strang, W. and Fix, G. (1973). *An Analysis of the Finite Element Method*. Prentice-Hall series in automatic computation. Prentice-Hall. 64

[73] Strogatz, S. (2000). From kuramoto to crawford: exploring the onset of synchronization in populations of coupled oscillators. *Physica D: Nonlinear Phenomena*, 143(1–4):1–20. 94

[74] Thorp, J. S., Seyler, C. E., and Phadke, A. G. (1998). Electromechanical wave propagation in large electric power systems. *IEEE Transactions on Circuits and Systems I: Fundamental Theory and Applications*, 45(6):614–622. xi, 75

[75] Wells, C. (1969). *Viscous Drag Reduction: Proceedings of the Symposium on Viscous Drag Reduction Held at the LTV Research Center, Dallas, Texas, September 24 and 25, 1968*. Plenum Press. 43

[76] White, F. (2003). *Fluid Mechanics*. McGraw-Hill international editions. McGraw-Hill. 44, 52

[77] Wilkinson, S. P. (1990). Interactive wall turbulence control. *Viscous drag reduction in boundary layers*, 1:479–509. 43

Vita

Samir Sahyoun received his B.S. in Electrical Engineering from Misr University for Science and Technology, 6th of October city, Egypt in 2003. From 2003 to 2005, he served as a full time Communications Engineer at Electrowave, Dubai, UAE. Funded by the Fulbright Scholarship Award, he received his Masters Degree in Electrical Engineering from University of Tennessee, Knoxville, TN, USA in 2009. Besides his research work, Samir worked as an instructor for Signal and Systems and Automatic Control courses at the University of Tennessee From 2012 to 2016. He will graduate with a Doctor of Philosophy in Electrical Engineering from the University of Tennessee, Knoxville, TN, USA in May 2017.